UNIVERSITY OF GRONINGEN

MASTER RESEARCH PROJECT

MASTER INDUSTRIAL ENGINEERING & MANAGEMENT
MASTER ENERGY & ENVIRONMENTAL SCIENCES

The potential of solar carports in an AC/DC hybrid microgrid

Author:
Sándor Kruse

First Supervisor IEM:
Prof. dr. ir. J.M.A. (Jacquelien) Scherpen
First Supervisor EES:
Dr. R.M.J. (René) Benders
Daily Supervisor IEM:
Dr. M. (Michele) Cucuzella

February 27, 2020

university of groningen / faculty of science and engineering

Abstract

Over the past years the concept of hybrid microgrids has become more and more interesting. The implementation of this type of configuration presents several advantages to generate local power and to supply local demand. This research is, therefore, focused on the design of a hybrid microgrid of which a solar carport is part of. An average Dutch office building is taken as a reference. A solar covered parking lot, a battery, and electric vehicles are considered to be present on the DC side of the microgrid, and a load and grid connection on the AC side. A two-level control strategy is proposed to control the hybrid microgrid with the objective to minimize the power exchange with the utility grid. Consequently, simulations have been conducted to test the individual control layers as well as the two-level control strategy. Finally, the hybrid microgrid is compared with four alternative configurations, ranging from only a local load and the load induced by the EVs to a solar carport connected to the local load. Based on the results, it can be stated that the hybrid microgrid can reduce the dependency on the grid significantly as well as improve the coordination of meeting local demand with local supply.

Contents

List of abbreviations

Abbreviation	Definition
AC	Alternating current
BESS	Battery energy storage system
CCM	Current control mode
D	Duty cycle
DC	Direct current
DG	Distributed generator
EMS	Energy management system
ESS	Energy storage system
EV	Electric vehicle
GHI	Global horizontal irradiance
IC	Incremental conductance
ILC	Interlinking converter
KCL	Kirchhoff's current law
KVL	Kirchhoff's voltage law
LDC	Load duration curve
m	Modulation index
M	Number of EVs
MPC	Model predictive control
MPP	Maximum power point
MPPT	Maximum power point tracking
N	Prediction horizon
P&O	Perturbation and observation
PHEV	Plug-in hybrid electric vehicle
PI	Proportional-Integral
PID	Proportional-integral-derivative
PLL	Phase-locked loop
pu	Per unit
PV	Photovoltaics
PWM	Pulse width modulation
RES	Renewable energy source
RMS	Root mean square
SOC	State of charge
SPWM	Sinusoidal pulse width modulation
SST	Solid state transformer
V2G	Vehicle-to-grid
VCM	Voltage control mode
VSC	Voltage source converter
w	Weights MPC cost function

Chapter 1

Introduction

Due to the current global energy transition, a trajectory is set to reduce carbon emissions by fossil fuels. Consequently, the energy production by renewable energy sources (RES), such as wind and solar photovoltaics (PV), is increasing. Decarbonizing the power sector as well as large-scale electrification of transport, industry and buildings are considered key in the energy transition and for reaching the climate goals set for 2050. As a result, the share of electricity in the total worldwide energy demand is expected to grow from 20% to 40% by 2050. Hereof, 60% is expected to be produced by wind and solar PV [1].

Due to the current and future changes in the electricity sector, the conventional power system is undergoing a transformation. The system shifts from predominately centralized electricity generation to more decentralized generation, since RES are generally more distributed. Unfortunately, the more distributed RES can cause significant capacity issues for the power grid [2]. On the contrary, also several advantages are accompanying this shift. When power can be fully supplied by local RES, long-distance high-voltage transmission is no longer required. Local electricity generation can be used to meet local electricity demand. The microgrid concept is embracing this principle by combining it with local control and coordination. When operated properly it can meet the needs of electricity consumers as well as the needs of the grid operators. Moreover, it is considered to be more economical, reliable and efficient [3, 4].

When the concept of the microgrid was introduced, research was mostly dedicated to the AC microgrid. After all, last century the power system was predominately AC driven. Currently, however, this dominance is decreasing. DC power is rapidly increasing its share in the power system since most RES and more modern loads have a DC interface. As a consequence of this shift within the power system, DC microgrids became also interesting. Both, AC and DC, microgrids present significant advantages and reduce the conversion losses for, respectively, AC and DC generators and loads. Nevertheless, power conversion is still required to facilitate both AC and DC generators and loads [4, 5]. By combining the advantages of the AC and DC microgrids, the more complex hybrid AC/DC microgrid was introduced. In this type of microgrid a separate AC microgrid is connected by one or more interlinking converters (ILCs) to a DC microgrid [6, 7].

Possible application of microgrids can be found in smart parking systems for electric vehicles (EVs). This type of application is especially of interest with an increasing number of EVs, due to the electrification of the transport sector [1]. For the integration of large numbers of EVs in the current power systems, coordination is required. If the charging of these EVs is performed uncoordinated, it can negatively impact the grid due to extra large and undesired peaks in electricity demand. Also, preferably EVs are charged with electricity generated by RES. Smart parking systems enable to locally coordinate the charging of

EVs, to maximize the use of renewable electricity as well as to limit the impact on the grid [8, 9]. A DC microgrid can in this case interconnect local solar PV generation and electricity demand of the EVs. The use of EVs within this type of system also enables other advantages. The EVs can be used as energy storage systems (ESS) and supply power back to the microgrid. This concept is known as vehicle-to-grid (V2G). Smart parking systems can provide opportunities and limit the possible disadvantages endured by the growth of the number of EVs [8, 9]. As a result of the above, the charging strategies can be diverse. Ref. [10] differentiates several articles on smart parking systems with different charging strategies, ranging from maximizing profits, minimizing costs or maximizing the use of RES for charging the EVs. Some strategies also enable to maximize RES generation, resulting in supplying surpluses to the grid. In practice, a common implementation of smart parking systems, is in the form of solar carports. These can even increase the value of parking lots due to its multi-functional use [11]. Similarly, in [12] EVs are even considered as part of a solution to enable a higher penetration of solar PV.

Only more recently, smart parking systems for EVs were discussed as part of AC/DC microgrids. Ref. [13] proposed to develop a plug-in hybrid EV (PHEV) charging coordination approach with the aim to minimize charging expenses for PHEV owners. In [14], the advantages of the storage capability of the EVs are exploited differently. A charge/discharge controller for the EVs is designed to regulate frequency and to balance power within the hybrid microgrid. The focus of [15] is on an isolated hybrid AC/DC microgrid. It presents a multi-layered coordination algorithm to coordinate the charging of the EVs to improve the performance of the islanded commercial hybrid AC/DC microgrid. It includes the charging of three-phase AC and DC types of EVs. Similarly, in [16] the effects of different charging strategies for these types of EVs on the AC/DC hybrid microgrid were investigated. Furthermore, [17] proposes a design of an EV charging station as part of a hybrid AC/DC microgrid. Only, the design makes use of a different type of hybrid AC/DC microgrid. Ref. [18] proposes a design for a need-based distributed coordination strategy to use the V2G principle to regulate the DC bus voltage of the hybrid AC/DC microgrid. The authors argue that this type of microgrid only would apply for commercial and industrial vicinities, due to the complexities of this type of microgrid. Moreover, with the local PV generation the electricity demand of the commercial buildings can be supplied and the EV storage capabilities enable efficient operation of the microgrid [18].

Motivated by the ongoing research on smart parking systems, the role of EVs in AC/DC microgrid and issues with the growth of solar PV and EVs, this research is investigating the practical solar carports as part of a hybrid AC/DC microgrid. While exploiting the advantages hereof, the aim is to minimize the power exchange with the utility grid. This can be considered as highly relevant since it would allow for more local solar power and EVs whilst reducing the negative consequences on the utility grid.

Chapter 2

Problem analysis

2.1 Problem description

In recent years smart parking systems as part of a hybrid microgrid have been discussed in literature. The operation objectives of these systems were diverse, ranging from cost minimization for charging EVs to maximizing local RES generation. Nevertheless, no research has been devoted yet to the contribution solar carports as part of hybrid microgrid can have on minimizing the power exchange with the utility grid. This is done by maximizing local RES generation and supplying internal demand. Consequently, the potential of solar carports as part of a hybrid microgrid, on generating and supplying local demand without burdening the utility grid is therefore also unknown.

2.2 Research aim and main research question

This research aims to design a hybrid AC/DC microgrid that represents a business premises with a solar covered parking lot and operates to minimize the power exchange with the utility grid. Subsequently, it is of interest to gain insight into the potential of this system in generating electricity and supplying internal demand. Based on the research aim the following main research question is defined:

How can a hybrid AC/DC microgrid that represents a commercial building with a solar covered parking lot be controlled to minimize the power exchange with the utility grid and what is the effect on the internal power demand and supply?

2.3 Sub-questions

To be able to answer the main research question, several sub-questions can be defined:

- *How is the hybrid microgrid including the solar carport configured?*
- *What is an average representation of a commercial facility with a solar carport for a hybrid microgrid?*
- *How can the hybrid microgrid be modeled?*
- *How should the hybrid microgrid and its components perform?*
- *How should the control strategy be designed to minimize the power exchange with the grid?*

- *What is the effect of the control strategy on the hybrid microgrid?*
- *What is the potential of a solar carport with respect to the internal power generation and consumption, and the power exchange with the utility grid?*

2.4 System description

The system that is of interest in this research is a hybrid AC/DC microgrid that represents a commercial building with a neighboring solar covered parking lot. Figure 2.1 displays an example of a possible hybrid microgrid, where the AC and DC microgrid are marked. In practice, this corresponds to most business premises with a local parking lot, such as offices, industrial facilities, airports, and hospitals. The actual configuration and the reference system that is considered in this research will be discussed next as well as the control strategy.

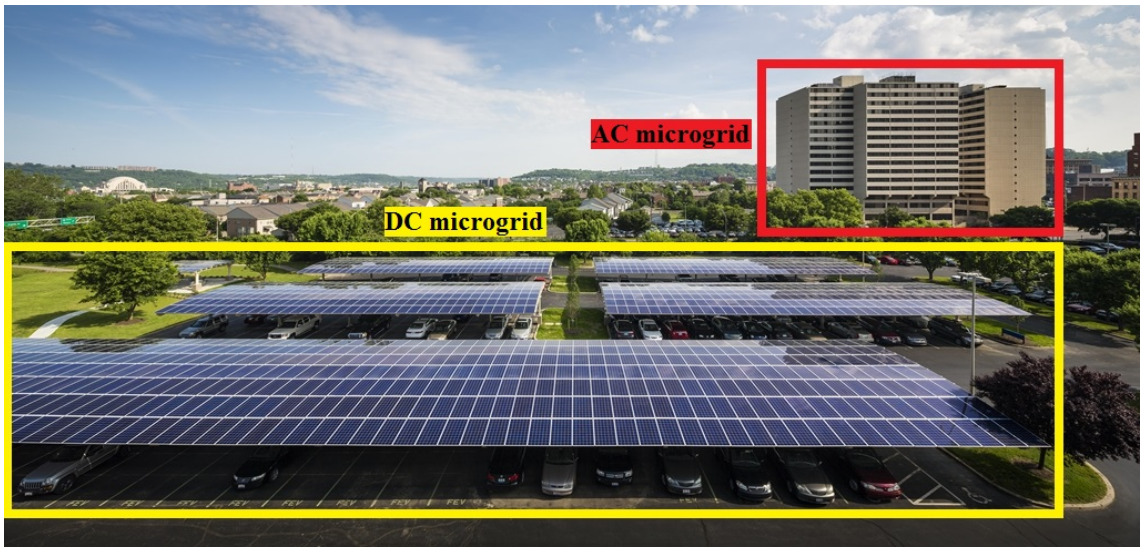

Figure 2.1: A practical hybrid AC/DC microgrid based on the employee parking lot of Burke in Cincinatti, United States [19]. The DC microgrid is highlighted in yellow and the AC microgrid is marked in red.

2.4.1 System configuration

The basic setup of hybrid microgrid defines the system to consist of an AC microgrid interconnected via the ILC to a DC microgrid. The AC microgrid contains for this system design an AC load and a grid connection. The AC load demands electricity within the hybrid microgrid via the AC bus. The utility grid operates as a slack bus for the AC bus and only exchanges power when the microgrid as a whole has a shortage or surplus. The DC side of the microgrid, incorporates a solar PV array, EVs and an ESS in the form of a battery (BESS). The EVs and solar panels are the considered components of a solar carport. The solar panels supply electricity to the DC bus by using a boost converter. The EVs are connected via a bidirectional converter to the DC bus. This converter enables the charging/discharging of the EVs. Finally, the BESS is present as a buffer and is also connected via a bidirectional converter to the DC bus.

2.4.2 Reference system

To represent the the hybrid microgrid, an average office building is taken as reference. Ref. [20] states the average office building in the Netherlands to be $955m^2$. According to [21], an office of this size would annually use $54.9kWh/m^2$. Furthermore, based on the parking policy of a random selected Dutch municipality, 1.9 parking lots per $100m^2$ of office area are required. Furthermore, the dimensions of each lot are considered to be 2.5 by 5.0 meter [22]. Similar to the figure, the solar carports only cover the parking lot area.

2.4.3 Control design

Based on the given system description the hybrid microgrid is controlled to minimize the power exchange with the utility grid. For this purpose the microgrid is configured with a two-level control strategy, as shown in Figure 2.2. The lower-level control includes the control of the individual components with their own control objectives. A boost converter is responsible for stepping up the voltage and for enforcing the solar panels to operate at maximum power, by using maximum power point tracking (MPPT). The bidirectional converters of the EVs and the BESS take care of the charging and discharging. Also, the converter of the BESS controls the DC bus voltage. Furthermore, the ILC controls the power exchange between both microgrids.

On the AC side of the microgrid, the AC loads consume power from the AC bus. The power is considered to be three-phase AC power and the AC frequency and voltage regulation is performed by the utility grid, which acts as infinite buffer. The ILC is responsible for synchronizing the voltage when power is transferred from the DC to the AC side.

The higher-level controller is responsible for the power management in the hybrid microgrid. It does, however, not affect the solar power generation nor the AC loads. The amount of power transferred between the AC and DC side of the microgrid is determined by the higher-level controller and depends on the state of charge (SOC) of the BESS and the EVs, the PV generation and the AC load. The charging of the EVs and the BESS is also determined by the higher-level controller, based on its objective to minimize the power exchange with the utility grid.

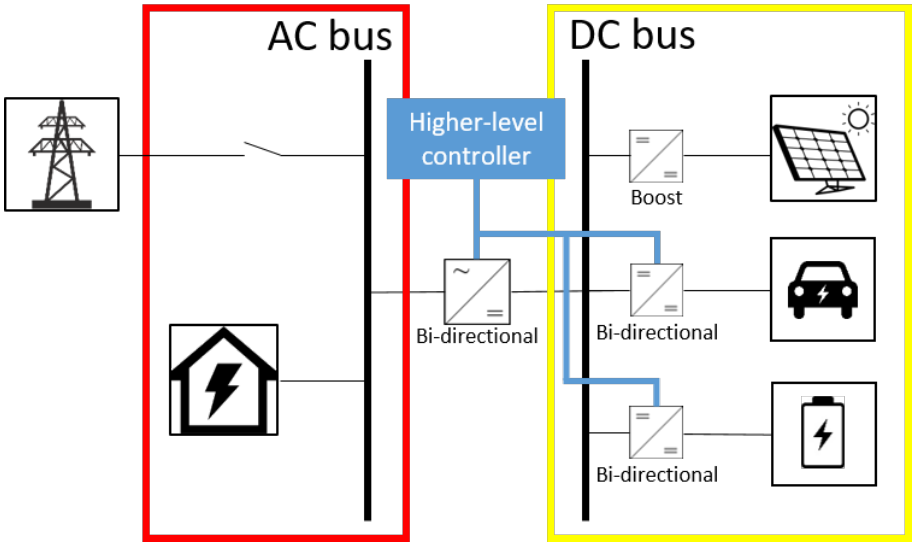

Figure 2.2: Schematic system description of hybrid AC/DC microgrid. The AC and DC microgrid are highlighted in red and yellow respectively. The higher-level controller is represented in blue.

2.5 Reading guide

The topic of this research has been introduced in section 1. In section 2, the problem of interest has been explained in more detail, the research questions have been proposed, and the system has been defined. Section 3 is used to provide more in-depth information supporting and explaining theory that is relevant in section 4 and section 5. The modeling of the different components of the system and the simulation model are discussed in section 4, followed by the control strategy of the hybrid microgrid in section 5. In section 6, several scenarios on the hybrid microgrid are proposed and the results are discussed. Sections 7 and 8 are, respectively, devoted to the discussion and the conclusion.

Chapter 3

Background

For the modeling of the hybrid microgrid and its components, and designing the control strategy, some background theory is provided. To start, this section elaborates on the ILC and the control of a hybrid microgrid. Hereafter, some basic power electronics theory is provided on different converters, pulse width modulation (PWM), switching frequencies versus sampling freqrency, and MPPT. Finally, the two in this research used control techniques, PI control and model predictive control (MPC), are introduced and explained.

3.1 ILC

3.1.1 Power topology

The ILC or ILCs within a hybrid microgrid are the interconnecting elements between the AC and DC microgrid. The role of the ILC depends on many factors. The microgrid power topology can affect the type of ILC that is required. Three main variants are distinguished: the conventional topology, the multi-microgrid and the solid state transformer (SST) topology [4]. Some unconventional power topologies are also discussed in literature, such as a three-level hierarchical power architecture [23, 24], however these are not further discussed here.

The first power topology is the conventional topology, wherein the ILC along with its filter connects the three phase AC side to the DC side. This topology is suitable in case of greenfield installations owned by one owner and is mainly used in low-voltage networks. This type of topology can vary in terms of the use of different ILCs and the location of the storage element [4].

The second topology of a hybrid microgrid is referred to as multi-microgrid or community microgrid (Figure 3.1). In this case two or more independent neighboring microgrids are integrated into a multi-microgrid to improve the performance in terms of backup, power quality, reliability, efficiency and economic optimization. Usually, the different AC or DC microgrids have different owners. Similar to the conventional topology, the multi-microgrid utilizes a single-stage converter, such as voltage source converters (VSC), or other two-stage converters as ILCs [4].

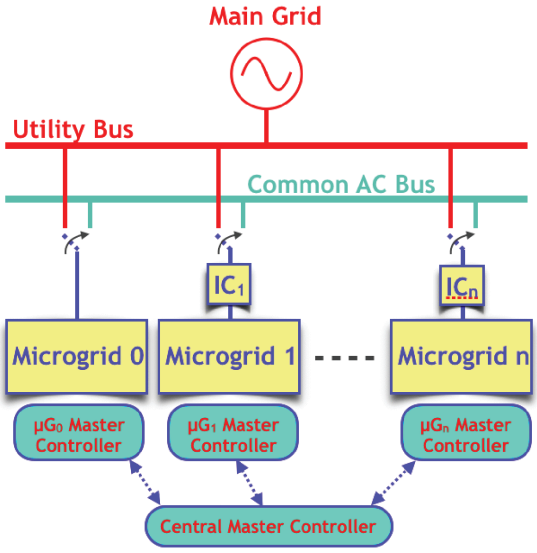

Figure 3.1: An example of a hybrid multi-microgrid [4]

The SST based topology is the third topology. The SST acts as an ILC for interfacing the AC and DC microgrid, and the main grid. In contrast to the conventional topology and the multi-microgrid, the SST integrates the converter stage, transformer and filter into one device. As a result, it can act as an energy router and perform all functions of a conventional transformer [4]. Typically, a SST consists of a high-voltage rectifier, a high-frequency DC-DC chopper and a low-voltage inverter [25] (Figure 3.2). The SST based topology can coordinate power exchange among existing neighboring AC and DC microgrids [26, 27] as well as provide ancillary services to the grid [28]. Single-phase SST based microgrids have shown to be very suitable to integrate smart housing communities [29].

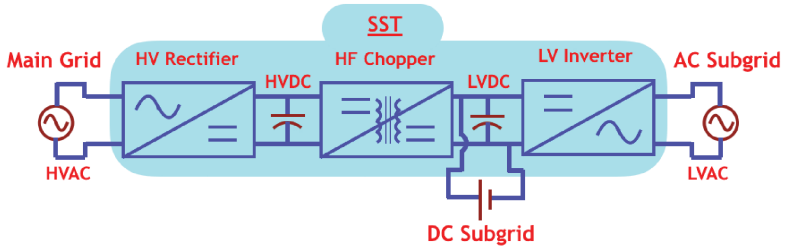

Figure 3.2: Solid state transformer [4]

3.1.2 ILC types

Depending on the direction of the power flow between both sides of the hybrid microgrid, the ILC or ILCs act as a rectifier or inverter. In grid-tied mode, the ILC can control the DC bus voltage, while in islanded mode it can provide a slack bus to the AC or DC bus. The ILC can have different converter topologies and configurations to supply this power transfer function. This converter topology primarily depends on the control objectives that the ILC must be able to fulfill. Although power management is the primary function of an ILC, additional control objectives can be included such as storage coordination, stability improvement, harmonics mitigation and more. Depending on the control objectives various ILC topologies are possible. Ref. [4] classifies three types of ILC topologies based on the

number of converter stages and their locations: single-stage ILCs, two-stage ILCs, and advanced ILCs.

A PWM bidirectional VSC is the most suitable single-stage ILC for a conventional hybrid microgrid (Figure 3.3). The VSC can operate in voltage controlled mode (VCM) or current controlled mode (CCM). In VCM the VSC can regulate the AC or DC bus voltage and CCM enables the regulation of the power flow. CCM is most used since it allows the use of P-f and Q-V droop control. Also, multiple VSCs in parallel can be used for a higher power exchange. Next to the VSC, other single-stage converters have been proposed in literature, each with different advantages [4]. In [30] a bidirectional quasi-Z-source inverter is investigated, which enables the features of maximum constant boost and reduced switch stress. Furthermore, a bidirectional boost converter is discussed in [31]. It offers better stability and fewer reactive components. Lastly, a modular multilevel converter with individual batteries integrated into each of the modules as a ILC, reduces the energy exchange between the subgrids and improves the total efficiency [32].

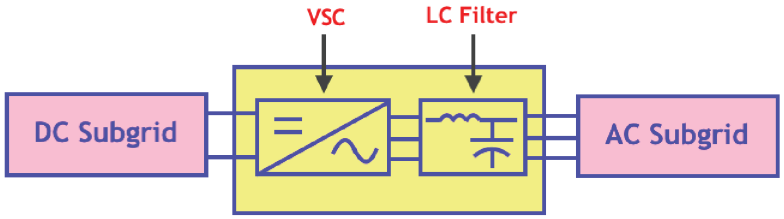

Figure 3.3: A VSC as a single-stage ILC [4]

The two-stage ILCs are either a cascaded or parallel combination of different types of converter. These ILCs allow more degrees of freedom in control and for additional power ports [4]. A common type of a two-stage ILC consists of a boost converter with a VSC. This converter topology can be used to integrate storage [33]. Similarly, a back to back converter that has two VSC stages enables the integration of storage as well as the integration of a DC subgrid. It can also be used to interface multiple AC microgrids with different frequencies [34]. On a similar note, [35] proposes a combination of a diode rectifier in parallel with a three-level neutral point converter as an active front.

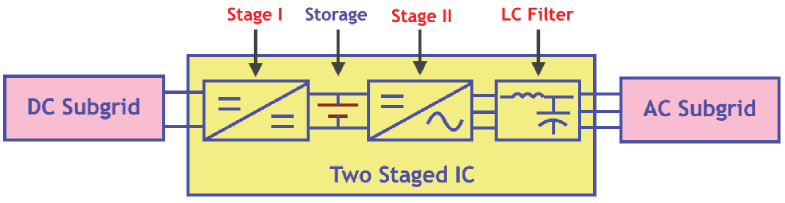

Figure 3.4: Two-stage ILC with a BESS at the DC link [4]

The last category of ILCs either uses an advanced control strategy or have an atypical ILC configuration to achieve multiple control objectives. For example, the use of multiple ILCs to interface the AC microgrid as well as the main grid is proposed in [36, 37]. This allows the AC grid to operate at a different frequency than the main grid. Furthermore, a three port converter is suggested in [38], which is a complex ILC configuration. This converter interfaces the main grid, the DC microgrid, and the AC microgrid. Consequently, the power from local generators and the grid can constantly be mixed, ensuring reliability

and providing controllable power to the loads. This category also includes the single-phase ILC, which can be used to connect a single-phase AC microgrid with a DC microgrid [39].

3.2 Hybrid microgrid control

Control of a hybrid microgrid presents significant challenges and for a large part determines the role of the ILC. Ref. [4] presents several sub-areas of control of which two are of interest in this research; power management strategies, and coordinated control and communication architecture. These subareas are discussed individually next.

3.2.1 Power management

Power management can be subdivided into several areas of control: active power control, reactive power control, AC and DC bus voltage control, storage power control and the control of ILCs in parallel.

Firstly, active power control is required to balance the active power within the hybrid microgrid and determines the power flow through the ILC. The loading conditions of the AC and DC microgrid can be based respectively on the frequency and the DC voltage. To able to apply droop control in a hybrid microgrid, the droop controllers of an AC microgrid and a DC microgrid need to be combined [40, 41, 42]. This can be done by normalizing the DC voltage and the AC frequency into a common term according to (3.1) and (3.2). The difference between these normalized terms can be used to determine the setpoint for the ILC by feeding it into a PI controller as shown in Figure 3.5 [43, 33]. Consequently, the change in load is shared over both sides of the hybrid microgrid. This decentralized control of the ILC has the downside that power is even flowing through the ILC for very low differences in load conditions among the subgrids [33]. To reduce this downside, [44] and [33] propose a control strategy that only allows power flow through the ILC if either of the subgrids is under loaded. Also, thresholds are set to limit the acceptable variations in DC voltage and frequency, before power flow is initiated. It is argued that the small variations are difficult to detect, which can lead to poorer performance. In [45], this issue was overcome by determining the exchange of power based on the DC voltage and the power flow through the ILC.

$$f_{pu} = \frac{f - 0.5(f_{max} + f_{min})}{0.5(f_{max} - f_{min})} \tag{3.1}$$

$$V_{DC,pu} = \frac{V_{DC} - 0.5(V_{DC,max} + V_{DC,min})}{0.5(V_{DC,max} - V_{DC,min})} \tag{3.2}$$

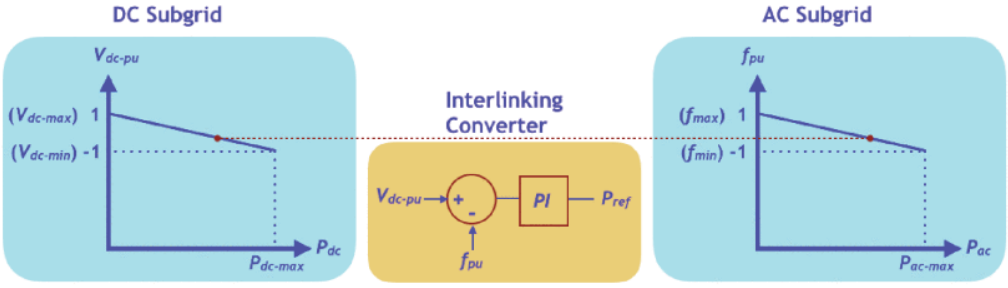

Figure 3.5: Droop control: normalization of the AC frequency and DC voltage [4]

On a similar note, [46] proposes a V_{DC}/V_{AC} droop control strategies to prevent frequent active power setpoint fluctuations. Ref. [47] presents an ILC control that considers the relative strengths and presence of critical loads in the subgrids.

Secondly, less of importance than active power control in hybrid microgrids, is reactive power control since only the AC microgrids considers reactive power. When only active power flows from the DC to the AC side of the microgrid, the ILC needs to contribute to the reactive power demand. Otherwise, the setpoint for reactive power is zero [4].

Thirdly, storage control is used in combination with intermittent DGs. An energy management system (EMS) tries to balance the intermittent power output of these DGs [7, 48] and maintain the energy balance by using energy storage [49, 50, 51]. Storage systems can be part of both sides of the microgrid. Preferably, DC storage is connected to DC microgrid and in case of islanding operation of the hybrid microgrid, it is responsible for maintaining the DC bus voltage [7, 48, 49, 52]. In [44] and [33] the EMS uses storage to minimize the energy flow between both sides of a hybrid microgrid. Ref. [52] proposes a centralized EMS to maximize the use of non-fossil DGs and minimize the use of storage. In [53] and [54] a decentralized EMS using droop based batteries is presented for power sharing during light and heavy loading conditions. Ref. [53], as well as [15], consider the integration of EVs as energy storage systems.

Next, AC and DC bus voltage control depends on the mode of operation of the hybrid microgrid. In islanded mode, the DC bus voltage is often regulated by an ESS. The AC bus can in this case be controlled by droop based inverter DGs [54, 48]. In grid-tied mode the ILC is usaully controlling the DC bus voltage. In [15], [30], [49], [34], [55] and [56] similar control strategies of the AC/DC bus voltage are discussed for both grid-tied mode and islanded mode. Furthermore, the droop control method proposed by [33] for the power exchange by the ILC leads to significant frequency variation, lower voltage quality and lower stability for the hybrid microgrid [45]. Ref. [45] and [57] propose control strategies to enhance the AC voltage based on VCM. In [55] a decentralized method is presented for DC bus control by using a disturbance observer based controller and in [58] a data driven model free voltage controller for the ILC is proposed. This controller can control both AC and DC voltage. Control of both AC and DC voltage and accurate proportional power sharing by only droop control is, however, difficult [58]. On a similar note, [33] makes a trade-off between maintaining small voltage deviations and accurate power sharing. Centralized or hierarchical control can be used to obtain both objective simultaneously [15, 59]. In [7] and [56] DGs are coordinated to simultaneously manage bus voltage control and power control. The DC bus stability and the DC bus voltage variations is controlled by DC storage that uses P/V_{DC} droop control. In a single phase AC microgrid, the ILC controls the active power flow by using droop control and the AC and DC bus voltage is regulated by using a central controller [39].

Lastly, multiple ILCs in parallel allow for larger power exchange between both sides of the hybrid microgrid. Ref. [60] states that the use of parallel ILCs leads to circulating currents, errors in reactive power sharing and DC power sharing. In [57], [61], [62] and [59] the ILCs are controlled using centralized or hierarchical control to tackle the problems proposed by [60]. Ref. [63] discovered that unequal power sharing occurs with the ILCs that use the droop control method used by [33] since the ILCs detect different voltages. A solution is presented by [64], however, equal loading on both sides of the microgrid is not achieved.

3.2.2 Coordinated control and communication architecture

Ref. [4] defines three possible levels of control for a hybrid microgrid. The primary level of control is for the individual components and requires relative fast control loops. The secondary and tertiary level of control need relative slower control loops. This has an effect on the control structure, which can be classified as decentralized, distributed, and centralized, based on the flow and the extent of sharing information between the controlled subsystems [65, 4]. In the case of the primary level, decentralized control is preferred since this structure does not use communication. For the secondary and tertiary level of control, more often centralized or distributed control is used. In these cases control can be responsible for energy management within the hybrid microgrid [44, 49, 51, 50]. The communication architecture and different control structures will be discussed next based on the review of [4].

Communication allows to share information between the components in the hybrid microgrid, which enables them to perform functions such as energy management and optimization. The way the communication is organized and the design hereof entails the selection of a suitable communication network topology, protocols and links for the controllable entities [66]. This depends primarily on aspects such as power network topology, control objectives, band-width of the controllers and the amount of data flow required. For example, functions such as voltage control and power sharing need more real-time communication without delays, while for other functions information on a slower timescale would suffice [4]. Similarly, wired links have usually a higher bandwidth and are therefore better for information sharing at the primary control level. On the contrary, wireless links have generally a lower band-width and are therefore better suited for slower secondary and tertiary control functions [4].

Decentralized control is the first control structure discussed here. Droop control, which is already discussed in previous section, is a good example of decentralized control. It is preferably used for performing primary control objectives such as power sharing, bus voltage regulation, and frequency regulation. This control structure does not use communication with other components in the hybrid microgrid and determines its action solely on local available information. In [67] it is, however, argued that decentralized control techniques can cause steady-state deviation in the nominal values of the AC frequency or DC voltage. This can be solved by using coordinated control with low band-width communication among control entities.

Secondly, centralized control uses two-way communication with the components in the hybrid microgrid to receive their status and return the setpoints. This control structure is commonly used to fulfill functions that require system-wide information such as accurate power management [67, 68] and optimal energy exchange between both sides of the microgrid [67, 54]. In [67] a secondary control layer is added to primary power sharing between ILCs to correct for the steady-state deviations. To eliminate these deviations and to achieve power sharing among the DGs and subgrids, [68] proposes modified normalization equations. In [15] a three layered centralized controller is suggested for EVs as storage system. The first layer is responsible for controlling the DC subgrid, while the secondary and tertiary layer are, respectively, responsible for active and reactive power in the AC subgrid. Also, optimization functions such as day-ahead scheduling, unit commitment [49, 69, 70, 71] and short-term optimal or economic dispatch are very well suited for centralized control structures [72, 73, 74]. In [70] on forecasted data and real-time power pricing of the dispatchable DGs, economic dispatch is based. Ref. [74] optimizes the energy cost and real-time harmonic voltage compensation of the AC bus. Furthermore, central controllers allow for optimal respond to meet demand based on real-time grid prices by controlling dis-

patchable loads. [49, 69, 75]. When grid prices are low the dispatchable loads can be used and thereby lower peak demand [75]. Also, loads that are less important can be curtailed depending on current grid prices and available power from the DGs [49]. These two principles can be combined in optimizing the power exchange with the grid by coordinate the charging and discharging of EVs [69].

Thirdly, distributed control is characterized by little communication between controlled entities and achieving consensus on the system-wide variables [76]. In [77] a consensus algorithm in the second control layer is used to control the frequency of the AC subgrid. Ref. [78] proposes a real-time control algorithm in a distributed multi-agent system for power management of a hybrid microgrid operating in both islanding and grid-tied mode.

The last control structure discussed in this review is hierarchical control. It is considered to be a structured approach of using centralized or distributed control [65]. This control structure is perfectly suited for complex controllable hybrid microgrids. It defines, depending on the control bandwidth, the tasks of the primary, secondary and, tertiary control layer. In [51] an EMS is proposed using hierarchical control to optimize the active power control. Decentralized control was used in the primary control layer of proportional power sharing. In the secondary layer, drift from nominal values of voltage and frequency is corrected, whereas the tertiary layer is responsible for generating setpoints for the DGs based on marginal generation costs. Ref. [79] presents a three layered hierarchical control to control power flow between multi-microgrids. Active power exchange is controlled via decentralized control as was proposed by [33]. The frequency and voltage deviations caused by this are controlled via the secondary control layer and economic optimization was done by using the tertiary layer.

3.3 Basic DC-DC converters

Next to the ILC interconnecting the AC and DC microgrid, several other converters are needed to interface the different components in the DC microgrid. Converters can be needed for several reasons, which can determine the type of converter that is required. To interconnect the solar array, BESS and EVs different DC-DC converters are need. Therefore, this section will discuss three basic types of DC-DC converters and explain the basic working.

3.3.1 Buck converter

To step down voltage, a buck converter can be used. The circuit of a DC-DC converter is shown in Figure 3.6. This converter can step down the input voltage (V_{in}) resulting in the output voltage (V_{out}). The converter uses PWM to regulate the switch. If the switch is closed (Figure 3.7a), the circuit is closed resulting in that the diode is reversed biased and the V_{in} is applied to the output. If the switch is opened (Figure 3.7b), the inductor current (I_L) will flow through the diode. By changing the duty cycle (3.3), which depends on the time the switch is closed (t_{on}) and the cycle time (T_s), V_{out} can be regulated as stated in (3.4). This relation only applies when the converter is in continuous conduction mode, meaning that the current through the inductor never reaches zero [80, 81, 82].

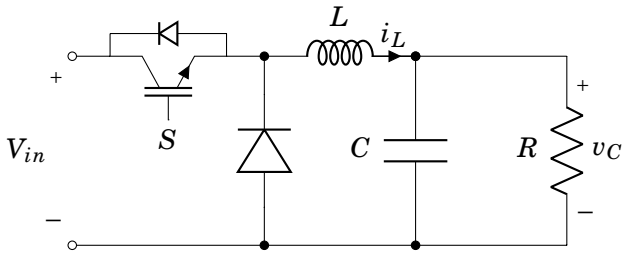

Figure 3.6: Circuit topology of DC-DC buck converter

$$D = \frac{t_{on}}{T_s} \tag{3.3}$$

$$v_c = D * V_{in} \tag{3.4}$$

In case the switch is on, current will flow according to Figure 3.7a. Based on this configuration, (3.5) and (3.6) represent the system dynamics. Together, both equations can be put in state space form, as is in (3.7).

(a) S is closed (t=on)

(b) S is open (t=off)

Figure 3.7: Circuit topology of DC-DC buck converter

$$L\frac{d}{dt}i_L = V_{in} - v_C \tag{3.5}$$

$$C\frac{d}{dt}v_C = i_L - \frac{v_C}{R} \tag{3.6}$$

$$\begin{bmatrix} \dot{i_L} \\ \dot{v_C} \end{bmatrix} = \begin{bmatrix} 0 & \frac{-1}{L} \\ \frac{1}{C} & \frac{-1}{RC} \end{bmatrix} \begin{bmatrix} i_L \\ v_C \end{bmatrix} + \begin{bmatrix} \frac{1}{L} \\ 0 \end{bmatrix} V_{in} \tag{3.7}$$

Similarly, in case the switch is off, the current flow in the buck converter changes (Figure 3.7b). The dynamics change accordingly into:

$$L\frac{d}{dt}i_L = -v_C \tag{3.8}$$

$$C\frac{d}{dt}v_C = i_L - \frac{v_C}{R} \tag{3.9}$$

$$\begin{bmatrix} \dot{i_L} \\ \dot{v_C} \end{bmatrix} = \begin{bmatrix} 0 & \frac{-1}{L} \\ \frac{1}{C} & \frac{-1}{RC} \end{bmatrix} \begin{bmatrix} i_L \\ v_C \end{bmatrix} + \begin{bmatrix} 0 \\ 0 \end{bmatrix} V_{in}. \tag{3.10}$$

By using (3.4), the state space form in case the switch is open and closed can be combined in average state space form:

$$\begin{bmatrix} \dot{i_L} \\ \dot{v_C} \end{bmatrix} = \begin{bmatrix} 0 & \frac{-1}{L} \\ \frac{1}{C} & \frac{-1}{RC} \end{bmatrix} \begin{bmatrix} i_L \\ v_C \end{bmatrix} + \begin{bmatrix} \frac{D}{L} \\ 0 \end{bmatrix} V_{in}. \tag{3.11}$$

3.3.2 Boost converter

The boost converter (Figure 3.8) is able to step up the voltage by, similar to the buck converter, using PWM. When the switch is closed (Figure 3.9a), the circuit is closed resulting in that the diode is reversed biased and the V_{in} is applied to the inductor. When the switch opens (Figure 3.9b), the stored energy in the inductor is released resulting in a higher voltage at the output V_{out}. The duty cycle, as mentioned for the buck converter, determines the ratio of V_{in} and V_{out}, as in (3.12) in case the converter is operating in continuous conduction mode [80, 81, 82].

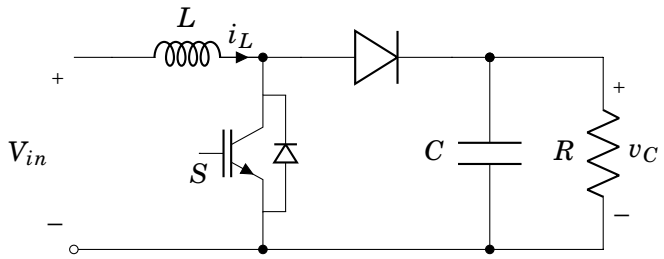

Figure 3.8: Circuit topology of DC-DC boost converter

$$\frac{v_C}{V_{in}} = \frac{1}{1-D} \tag{3.12}$$

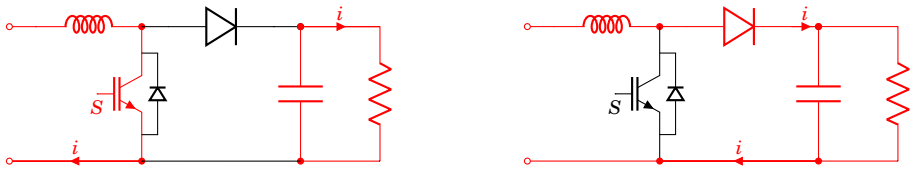

(a) S is closed (t=on)

(b) S is open (t=off)

Figure 3.9: Circuit topology of DC-DC boost converter

When the switch is on (Figure 3.9a), (3.13) and (3.14) can be derived, resulting in the state space equations in (3.15).

$$L\frac{d}{dt}i_L = V_{in} \tag{3.13}$$

$$C\frac{d}{dt}v_C = -\frac{v_C}{R} \tag{3.14}$$

$$\begin{bmatrix} \dot{i_L} \\ \dot{v_C} \end{bmatrix} = \begin{bmatrix} 0 & 0 \\ 0 & \frac{-1}{RC} \end{bmatrix} \begin{bmatrix} i_L \\ v_C \end{bmatrix} + \begin{bmatrix} \frac{1}{L} \\ 0 \end{bmatrix} V_{in} \tag{3.15}$$

In case the switch is open (Figure 3.9b), the current can flow around the circuit, resulting in (3.16) and (3.17), and together in state space form in (3.18).

$$L\frac{d}{dt}i_L = V_{in} - v_C \tag{3.16}$$

$$C\frac{d}{dt}v_C = i_L - \frac{v_C}{R} \tag{3.17}$$

$$\begin{bmatrix} \dot{i_L} \\ \dot{v_C} \end{bmatrix} = \begin{bmatrix} 0 & \frac{-1}{L} \\ \frac{1}{C} & \frac{-1}{RC} \end{bmatrix} \begin{bmatrix} i_L \\ v_C \end{bmatrix} + \begin{bmatrix} \frac{1}{L} \\ 0 \end{bmatrix} V_{in} \tag{3.18}$$

In case of continuous operation, the boost converter can be defined in one set of state space equations in (3.19).

$$\begin{bmatrix} \dot{i_L} \\ \dot{v_C} \end{bmatrix} = \begin{bmatrix} 0 & \frac{-(1-D)}{L} \\ \frac{(1-D)}{C} & \frac{-1}{RC} \end{bmatrix} \begin{bmatrix} i_L \\ v_C \end{bmatrix} + \begin{bmatrix} \frac{1}{L} \\ 0 \end{bmatrix} V_{in} \tag{3.19}$$

3.3.3 Buck-boost converter

In the buck-boost converter the input voltage can be stepped down and up. This type of converter is a combination of the buck converter and the boost convert (Figure 3.10) and is also using PWM. The operating mode of the buck-boost converter depends on the duty cycle. The ratio between V_l and V_h for a buck-boost converter (3.20) illustrates that a duty cycle of 50% is the tipping point of the operation mode. A duty cycle more than 50% enables boost mode and less than 50% the buck mode [81, 82].

$$\frac{V_h}{V_l} = \frac{D}{1-D} \tag{3.20}$$

In buck-mode the current will flow from the right side of the buck-boost converter to the left side (3.11a) and in boost mode vice versa (Figure 3.11b). To present this, the notation of current is positive in boost mode and negative in buck mode. Based on the topology of the buck-boost converter as shown in Figure 3.10, the state-space equation can be derived for both modes of operation by using the state-space equations of the buck and boost converter.

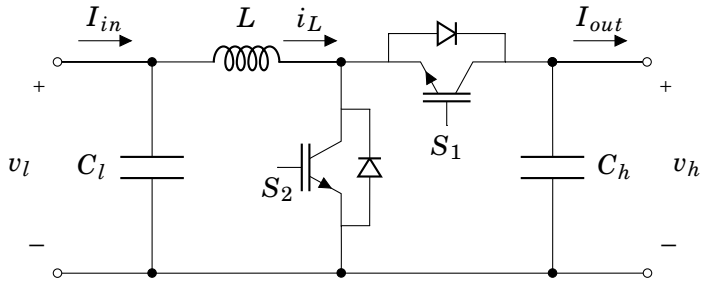

Figure 3.10: Circuit topology of DC-DC buck-boost converter

(a) Buck mode (S1 is switching) (b) Boost mode (S2 is switching)

Figure 3.11: Buck-Boost circuit topology

When the buck-boost converter is buck mode and the switch (S_1) is on, (3.21), (3.22), and (3.23) apply, which can be rewritten in state space form in (3.24).

$$L\frac{d}{dt}i_L = v_l - v_h \tag{3.21}$$

$$C_l\frac{d}{dt}v_l = I_{in} - i_l \tag{3.22}$$

$$C_h\frac{d}{dt}v_h = i_l - I_{out} \tag{3.23}$$

$$\begin{bmatrix} \dot{i_L} \\ \dot{v_l} \\ \dot{v_h} \end{bmatrix} = \begin{bmatrix} 0 & \frac{1}{L} & \frac{-1}{L} \\ \frac{-1}{C_l} & 0 & 0 \\ \frac{1}{C_h} & 0 & 0 \end{bmatrix} \begin{bmatrix} i_L \\ v_l \\ v_h \end{bmatrix} + \begin{bmatrix} 0 & 0 \\ \frac{1}{C_l} & 0 \\ 0 & \frac{-1}{C_h} \end{bmatrix} \begin{bmatrix} I_{in} \\ I_{out} \end{bmatrix} \tag{3.24}$$

Similarly, when the switch (S_1) is off in buck mode, (3.25), (3.26), and (3.27) represent the dynamics of the converter. Combined in the state space form (3.28) applies.

$$L\frac{d}{dt}i_L = v_l \tag{3.25}$$

$$C_l\frac{d}{dt}v_l = I_{in} - i_L \tag{3.26}$$

$$C_h\frac{d}{dt}v_h = -I_{out} \tag{3.27}$$

$$\begin{bmatrix} \dot{i_L} \\ \dot{v_l} \\ \dot{v_h} \end{bmatrix} = \begin{bmatrix} 0 & \frac{1}{L} & 0 \\ \frac{-1}{C_l} & 0 & 0 \\ 0 & 0 & 0 \end{bmatrix} \begin{bmatrix} i_L \\ v_l \\ v_h \end{bmatrix} + \begin{bmatrix} 0 & 0 \\ \frac{1}{C_l} & 0 \\ 0 & \frac{-1}{C_h} \end{bmatrix} \begin{bmatrix} I_{in} \\ I_{out} \end{bmatrix} \tag{3.28}$$

By combining the (3.24) and (3.28), the averaged state space of the buck-boost converter in buck mode is defined:

$$\begin{bmatrix} \dot{i_L} \\ \dot{v_l} \\ \dot{v_h} \end{bmatrix} = \begin{bmatrix} 0 & \frac{1}{L} & \frac{-D_1}{L} \\ \frac{-1}{C_l} & 0 & 0 \\ \frac{D_1}{C_h} & 0 & 0 \end{bmatrix} \begin{bmatrix} i_L \\ v_l \\ v_h \end{bmatrix} + \begin{bmatrix} 0 & 0 \\ \frac{1}{C_l} & 0 \\ 0 & \frac{-1}{C_h} \end{bmatrix} \begin{bmatrix} I_{in} \\ I_{out} \end{bmatrix}. \tag{3.29}$$

In case the buck-boost converter changes its mode of operation to boost mode (Figure 3.11b), the system dynamics change accordingly. When the switch (S_2) is on in boost mode (3.30), (3.31), (3.32), and (3.33) hold.

$$L\frac{d}{dt}i_L = v_l \tag{3.30}$$

$$C_l \frac{d}{dt} v_l = I_{in} - i_L, \tag{3.31}$$

$$C_h \frac{d}{dt} v_h = -I_{out}, \tag{3.32}$$

$$\begin{bmatrix} \dot{i_L} \\ \dot{v_l} \\ \dot{v_h} \end{bmatrix} = \begin{bmatrix} 0 & \frac{1}{L} & 0 \\ \frac{-1}{C_l} & 0 & 0 \\ 0 & 0 & 0 \end{bmatrix} \begin{bmatrix} i_L \\ v_l \\ v_h \end{bmatrix} + \begin{bmatrix} 0 & 0 \\ \frac{1}{C_l} & 0 \\ 0 & \frac{-1}{C_h} \end{bmatrix} \begin{bmatrix} I_{in} \\ I_{out} \end{bmatrix}. \tag{3.33}$$

For the buck-boost converter in boost mode (3.34), (3.35), (3.36), and (3.37) represent the dynamics when the switch (S_2) is off.

$$L \frac{d}{dt} i_L = v_l - v_h \tag{3.34}$$

$$C_l \frac{d}{dt} v_l = I_{in} - i_L \tag{3.35}$$

$$C_h \frac{d}{dt} v_h = i_L - I_{out} \tag{3.36}$$

$$\begin{bmatrix} \dot{i_L} \\ \dot{v_l} \\ \dot{v_h} \end{bmatrix} = \begin{bmatrix} 0 & \frac{1}{L} & \frac{-1}{L} \\ \frac{-1}{C_l} & 0 & 0 \\ \frac{1}{C_h} & 0 & 0 \end{bmatrix} \begin{bmatrix} i_L \\ v_l \\ v_h \end{bmatrix} + \begin{bmatrix} 0 & 0 \\ \frac{1}{C_l} & 0 \\ 0 & \frac{-1}{C_h} \end{bmatrix} \begin{bmatrix} I_{in} \\ I_{out} \end{bmatrix} \tag{3.37}$$

For the representation of the buck-boost converter in boost mode, the averaged state space form can be stated:

$$\begin{bmatrix} \dot{i_L} \\ \dot{v_l} \\ \dot{v_h} \end{bmatrix} = \begin{bmatrix} 0 & \frac{1}{L} & \frac{-(1-D_2)}{L} \\ \frac{-1}{C_l} & 0 & 0 \\ \frac{(1-D_2)}{C_h} & 0 & 0 \end{bmatrix} \begin{bmatrix} i_L \\ v_l \\ v_h \end{bmatrix} + \begin{bmatrix} 0 & 0 \\ \frac{1}{C_l} & 0 \\ 0 & \frac{-1}{C_h} \end{bmatrix} \begin{bmatrix} I_{in} \\ I_{out} \end{bmatrix}. \tag{3.38}$$

3.3.4 Closed-loop control

To control the power flows in a circuit, closed-loop control systems are used. Closed-loop systems depend on feedback, which means that the output (y) is compared to the desired value (r) of the system. This comparison results in an error (e) that is transformed to a control signal (u) by means of a controller. The control signal is fed to the system resulting in a new output, which is again used in the next iteration. Possibly, the system can be subjected to disturbances that can affect the performance of the system [83].

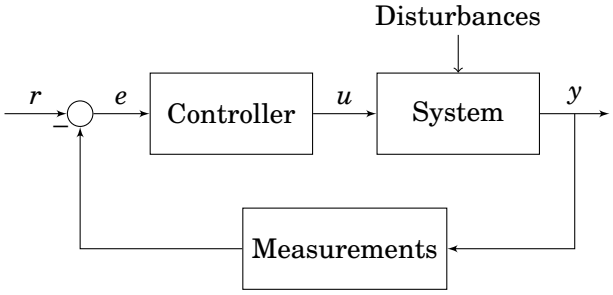

Figure 3.12: Closed-loop feedback control system

Implementing closed-loop control provides several advantages to the operation of the system. Ref. [83] states that by adding closed-loop control to a system several features are gained:

- Reduced effect of nonlinearities and distortions
- Increased accuracy
- Increased system bandwidth
- Less sensitivity to variation of system parameters
- Reduced effects of external disturbances.

It must, however, be mentioned that the controller design is crucial to ensure stable operation of the system. If the controller is designed poorly and the system is unstable, the system cannot function properly.

The control system as shown in Figure 3.12, can operate in different modes. This research, however, only includes CCM and VCM. In CCM (Figure 3.13a) the controller aims to maintain a constant reference current (I^*). Similarly, in VCM (Figure 3.13b) a constant reference voltage (V^*) is the objective. Both control modes generate the control signal for the plant [83].

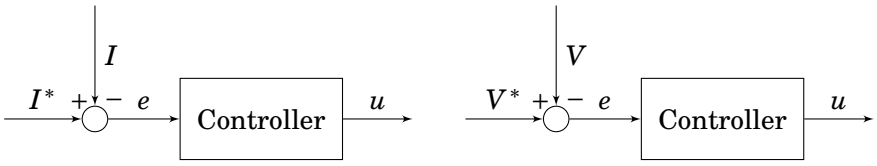

(a) Current controller (CCM) (b) Voltage controller (VCM)

Figure 3.13: Operation mode of a control system

3.3.5 PWM

PWM is used to regulate the switches of DC-DC and AC-DC converters, by transforming a control signal to the required gate signal. The switches of these converters can either be turned on or off. Each cycle the switch can only be turned on and off once. This can be represented as a square wave and when it is repeated a harmonic profile is visualized. To obtain this continuous binary switching signal, sinusoidal PWM (SPWM) is used. Other existing PWM techniques are outside the scope of this research since SPWM is considered to be the simplest technique and sufficient for the application in this research [84, 85].

SPWM compares (Figure 3.14) a sinusoidal reference signal (modulating wave) to a high frequency triangular wave (carrier wave). When the carrier wave is exceeding the modulating wave the switch should be on and when it is less that the modulating wave the switch should be off. As shown in Figure 3.15, the resulting gate signal corresponds to the comparison of the triangular carrier signal and the sinusoidal reference signal [84, 85].

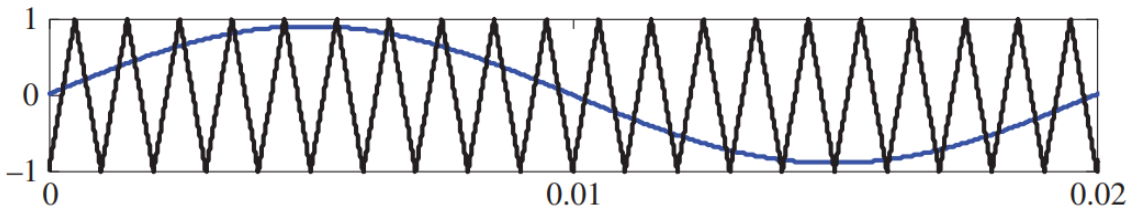

Figure 3.14: Modulating wave (blue) and carrierwave (black) of SPWM

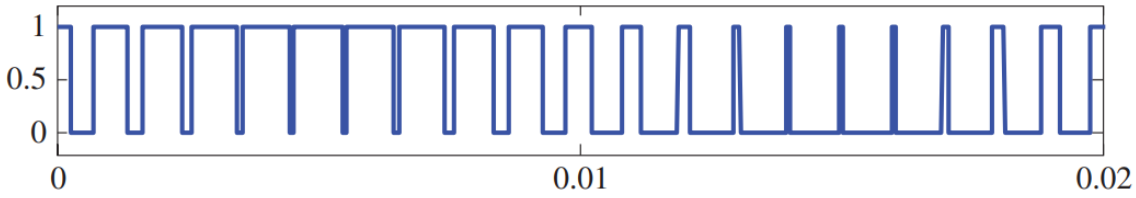

Figure 3.15: Gating signal of SPWM

According to (3.39), the carrier wave limits the range the PWM can regulate the gate signal. The modulation index (m) represents the ratio of the peak amplitude of the modulating wave and of the carrier wave, which are generally representing voltages. The modulation index should not be more than one ($m \leq 1$), otherwise the degrees of freedom are reduced [84, 85].

$$m = \frac{A_{mod}}{A_{car}} \tag{3.39}$$

This limitation results also in a limitation for AC-DC conversion. The amplitude of the phase voltages must be less than half the DC voltage in order to not exceed a modulation index of 1 based on (3.39) and basic power electronics. When expressed in RMS voltage, (3.41) is obtained, which provides a maximum ratio for the AC and DC bus voltage [84, 85].

$$V_{a,b,c} \leq \frac{V_{DC}}{2} \tag{3.40}$$

$$V_{rms} \leq 0.5\sqrt{\frac{3}{2}}V_{DC} \tag{3.41}$$

3.3.6 Conduction mode

A converter can be controlled in two conduction modes, continuous conduction mode and discontinuous conduction mode. In case of continuous conduction mode, the current over the inductor will never reach zero. In Figure 3.16a an example is given of a buck converter in continuous conduction mode. When the switch is on (T_{On}), the current over the inductor (I_L) increases until the switch is turned off (T_{Off}). Gradually, the inductor current decreases till the next switching cycles starts [86].

The discontinuous conduction mode, works similarly to the previously described continuous mode. In this mode, however, the current over the inductor reaches zero before the end of the switching cycle (Figure 3.16b). As a consequence, the operation of a converter is different in both conduction modes. Only converters in continuous conduction mode are considered here further since this mode is less complex and it is sufficient for its use in this

research. In line with this, the mathematical representation of the different converters is only provided in continuous conduction mode [86].

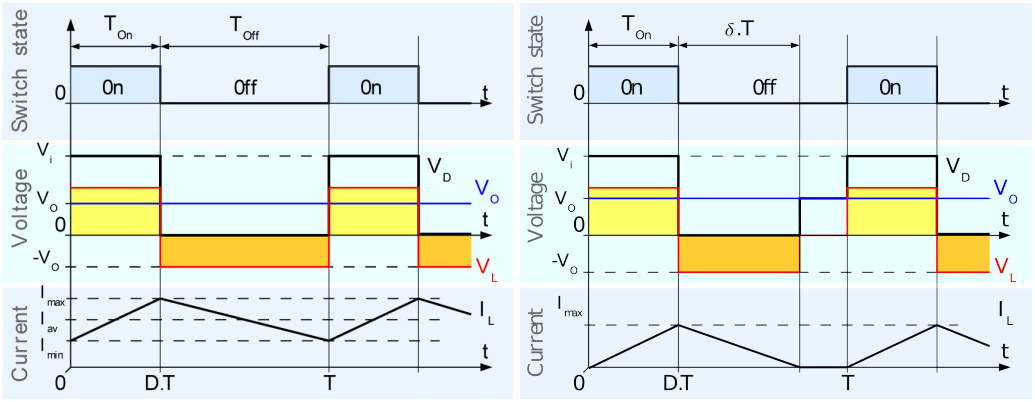

(a) Continuous conduction mode

(b) Discontinuous conduction mode

Figure 3.16: Conduction modes of operation of a buck converter [87]

3.3.7 Switching frequency versus sampling frequency

The speed at which the switches of converters are turned on and off depend on the switching frequency of a PWM controller. Higher frequencies are preferable since it results in faster transient response and reduced output ripple [88]. The switching frequency, however, is related to the sampling frequency, which represents the number of intervals per second of the modeled signals. More precisely, the sampling rate theorem states that the sample rate must be greater than twice as fast as the highest frequency component present in order to be able to reproduce the original wave form. In other words, this means that the highest switching frequency is based on the sampling rate. In theory, the minimum sampling rate is referred to as the Nyquist rate [89]. This principle is especially of importance for the modeling of the hybrid microgrid and its PWM controllers.

3.4 Maximum power point tracking

During operation of a solar cell the voltage and current can change. The mathematical relation of the current and voltage of a solar cell, results in an $I-V$ and $P-V$ curve (Figure 3.17). At every moment in time, only one combination of current and voltage is optimal, resulting in maximum power output. This specific point, is called the maximum power point (MPP). The temperature and irradiance affect the $I-V$ and $P-V$ curve and thereby also the MPP. To maximize the output power over time, a PV cell needs to operate constantly at this MPP. Adjusting to this MPP is MPPT and requires some sort of control. A MPPT device on itself controls the operating point, however, it cannot adjust it. A DC-DC converter is required to do so. The MPPT can be performed and adjusted on different levels depending on the setup of the PV system. Depending on the PV system setup the MPPT is done by the main centralized converter or by distributed converters [90, 80, 81].

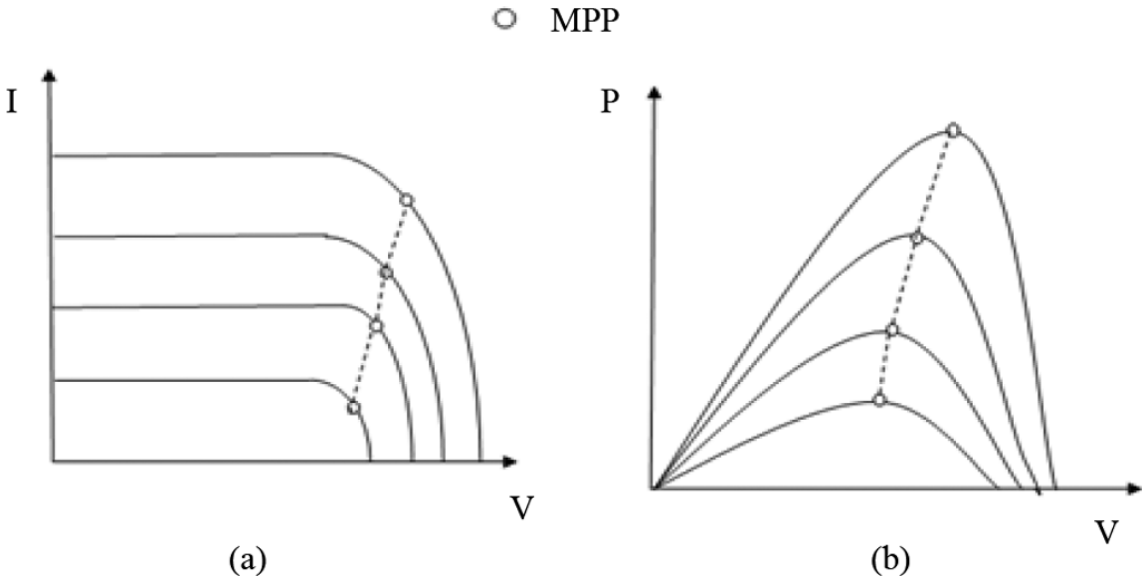

Figure 3.17: (a) I-V and (b) P-V characteristics of PV panel at different environmental conditions

Two MPPT techniques often used are the perturbation and observation (P&O) technique and the incremental conductance (IC) technique [91]. The first technique, P&O is also known as the "hill-climbing" algorithm. The basic P&O technique introduces a perturbation to the voltage of the PV system. As result, the power output will change. Depending on the current operating point in comparison to the MPP, the power output will either increase or decrease. If it increases the next perturbation will also increase the voltage if the previous perturbation increased the voltage. Similarly, the next perturbation will decrease the voltage if the previous perturbation decreased the voltage. In the case, the power output will decrease, the next perturbation will do exactly the opposite. Consequently, with each perturbation the operating point will converge to the MPP [81, 91]. A flow chart representing this principle is shown in Figure 3.18a. A more developed P&O technique, including a PI digital controller, is discussed in [92].

The IC technique uses the mathematical principle of the derivative of the $P-V$ curve being zero at the MPP:

$$\frac{dP}{dV} = 0. \tag{3.42}$$

This can be rewritten as (3.43).

$$\frac{dP}{dV} = \frac{d(IV)}{dV} = I + V\frac{dI}{dV} \tag{3.43}$$

If the sampling steps are taken small enough (3.44) can be used as an approximation.

$$\frac{dI}{dV} \approx \frac{\Delta I}{\Delta V} \tag{3.44}$$

In this case, $\Delta I/\Delta V$ is called the incremental conductance and I/V the constanteneous conductance. Given these equations the following three states can be defined:

$$\frac{\Delta I}{\Delta V} = -\frac{I}{V} \quad \text{if} \quad V = V_{mpp}, \tag{3.45}$$

$$\frac{\Delta I}{\Delta V} > -\frac{I}{V} \quad \text{if} \quad V < V_{mpp}, \tag{3.46}$$

$$\frac{\Delta I}{\Delta V} < -\frac{I}{V} \quad \text{if} \quad V > V_{mpp}. \tag{3.47}$$

By identifying the states of the system, with each iteration the system can be adjusted and controlled to aim for the MPP. In Figure 3.18b the control flow chart is shown for the IC technique [81, 91]. Also, a more advanced IC technique including a PI controller is discussed in [92].

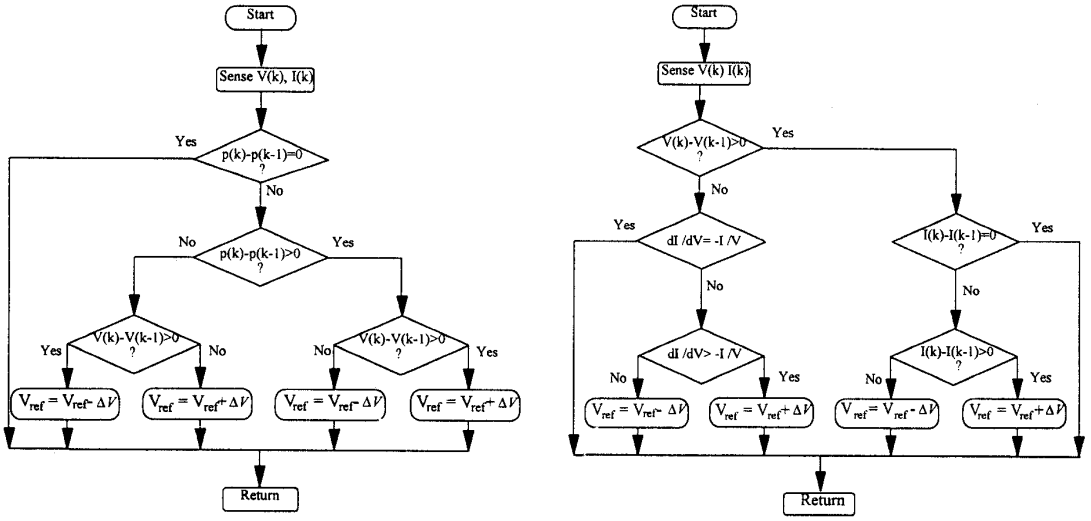

(a) Perturbation and Observation technique

(b) Incremental Conductance technique

Figure 3.18: Control flow chart [91]

With each iteration, the MPPT techniques determine the required control for the solar PV system to be operating at the MPP. Consequently, a converter uses PWM to adjust the operating point according to the MPP tracker [81].

3.5 Control techniques

This research proposes a design for a two-layer control strategy. For the lower level controllers PI controllers are used and for the higher level controller MPC is considered. These two control techniques are therefore discussed next.

3.5.1 PI control

PID (Proportional Integral Derivative) control is widely used in the process control industry. The proportional component of a PID controller increases the speed of the transient response. The integral part of the controller can drive the steady-state error to zero and, lastly, the derivative component provides a way to respond quickly. This research, however, does not include the D component since it is difficult to tune and, generally, not needed for the complexity of the system considered here [93].

Based on the closed-loop feedback control system (Figure 3.12), the PI controller can be represented as part of the control loop (Figure 3.19). The individual P and I component are presented separately [93].

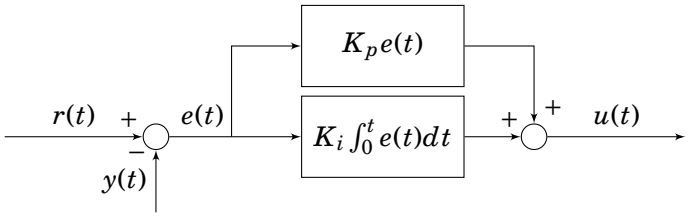

Figure 3.19: PI controller

The output of the PI controller is the input for the plant that is being controlled. The output, the control signal ($u(t)$), can be defined according to Figure 3.19:

$$u(t) = K_p * e(t) + K_i \int_0^t e(t)dt, \tag{3.48}$$

where

$$e(t) = r(t) - y(t). \tag{3.49}$$

The tuning of the PI controller is done by adjusting K_p and K_i. The goal of tuning the controller is enabling stable operation of the system without a steady-state error. This means that the output stabilizes at the desired value over time, resulting in zero error (3.50) [93].

$$\lim_{x \to \infty} r(t) - y(t) = e(t) = 0 \tag{3.50}$$

3.5.2 MPC

MPC provides an intuitive approach to optimally control systems under some form of constraints. For this reason, MPC, as advanced control strategy, is widely accepted in the industry. It utilizes a wide range of control methods, which use a model to determine the control signal by minimizing a cost function. MPC chooses the best of all feasible input sequences over a future horizon under some constraints. Every iteration the first input of this sequence is applied to the system. At the next sampling time, when the MPC receives new state information, the horizon recedes and the procedure is repeated. This way MPC can solve a constrained dynamic optimal control problem by repeating an online optimization of an open-loop problem [94].

Although MPC has some similarities to other predictive control methods, there are several advantages over other methods. Ref. [94] defines the following to be the most important:

- The concept is very intuitive and the tuning is relatively easy.
- It can be applied to a great variety of systems, ranging from simple systems to complex systems that are even unstable.
- Different performance criteria can be fulfilled.
- Compensation of measurable disturbances is easily derived.
- The controller is easy to implement.
- Its extension to the multivariable case is conceptually straightforward.
- Future references can easily be integrated.

Next to the advantages, some important disadvantages can be distinguished. Firstly, deriving the MPC controller is more complex than that of more conventional controllers. Secondly, MPC is highly depending on the availability of an appropriate model of the system. In case of mismatch of the real system and model that is used, the performance will be negatively affected [94].

The working of the MPC controller can be described by the following strategy [94], corresponding to Figure 3.20:

1. At each sampling instant (t), the future outputs are predicted over a determined horizon, the prediction horizon (N), by using a dynamic model of the system. The predicted outputs are represented as $y(t+k|t)$, where $k = \{1,...,N\}$. These outputs depend on all states, past inputs, and past outputs that are known at instant t and the computed future control signals ($u(t+k|t)$, where $k = \{0,...,N-1\}$).

2. The future control signals are calculated by optimizing a cost function. This optimization aims the output to approach a setpoint. Generally, this cost function is of a quadratic form and represents the error between the predicted output and the setpoint.

3. The control signal at the current time instant t ($u(t|t)$) is sent to the process, while the control signals for next time instants are neglected. This is done because at the next time instants $y(t+1)$ is already known. After the control signal is sent to the process, step 1 and 2 are repeated with this new value to calculate $u(t+1|t+1)$. This is called the receding horizon concept.

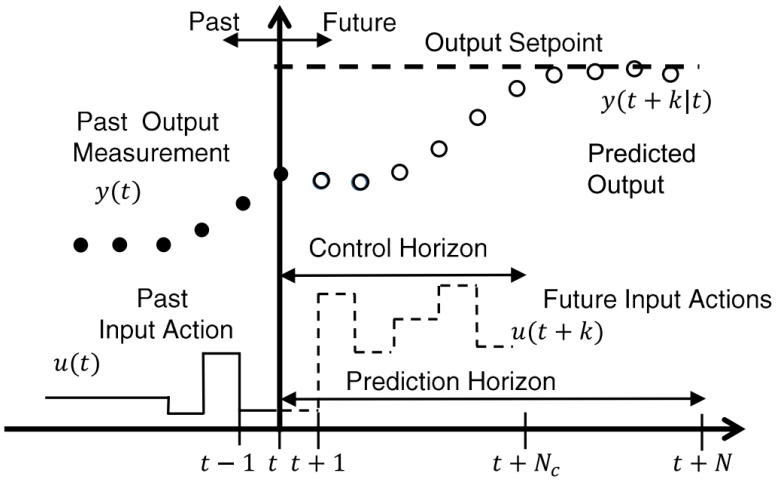

Figure 3.20: MPC strategy [94]

When the MPC strategy is implemented, the structure as shown in Figure 3.21 can be used. Based on the states, past inputs, past outputs, and future inputs the predicted outputs are modeled by using a dynamical model. Next, the error can be predicted which forms the input of the optimizer taking the cost function and constraints into account.

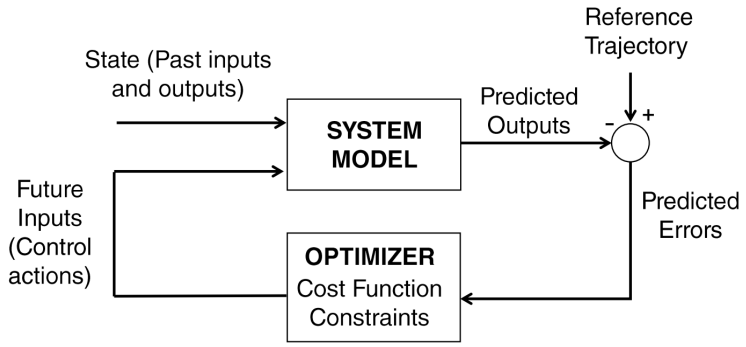

Figure 3.21: Basic structure of MPC [94]

Chapter 4

System model

In this section, first the modeling software is discussed. Furthermore, all individual components are discussed including their mathematical model, accompanied with its corresponding Simulink model.

4.1 Matlab Simulink

To build a simulation of the hybrid microgrid discussed in this research, Matlab Simulink is used. Simulink is a build-in module of Matlab. It enables to visually model the hybrid microgrid and is available at the University of Groningen. Furthermore, this software program is considered suitable since all components, control strategies, and features of the system can be implemented, either in Simulink or Matlab. Lastly, existing models for the bidirectional DC-DC converter [95], PV array, and grid connection [96] can be used.

4.2 ILC

As discussed previously, the ILC is responsible for the power exchange between the AC and DC side of the hybrid microgrid. To translate this to a model, the ILC needs to be specified. For the microgrid of interest in this research, a PWM bidirectional VSC is used. This type of ILC is considered to be the best fit for multiple reasons. To start, the defined system in section 2.4 complies best with the conventional power topology, for which a PWM bidirectional VSC is most suitable. Also, the system setup is considered not to be complex allowing for a rather simple ILC in the form of single stage ILC. Last, the ILC only needs to regulate the power flow between the AC and DC bus, of which a VSC is capable.

A single PWM VSC is commonly used in literature as the ILC in hybrid AC/DC microgrids. Generally, the VSC is paired with a filter. Different types of filters have been used such as a RLC filter [97, 58, 56, 98, 99, 100, 7], LCL filter [55, 101], RL filter [102] and L filter [33, 103]. The different converter topology also result in different system dynamics. For the configuration in this research a RL filter is used, as it should suffice for the system setup.

The circuit diagram of configuration of the ILC applied in this research is shown in Figure 4.1. Compared to most ILCs used in literature, an extra capacitor is added. The voltage over this capacitor (V_c) is an important element that determines the power flow over the ILC. Based on basic power electronics, the power flow will be regulated by adjusting the voltage of this capacitor compared to the constant DC bus voltage (V_{DC}). As a result of difference in voltage, current will flow between the ILC and the DC bus, and power can be transferred via the ILC.

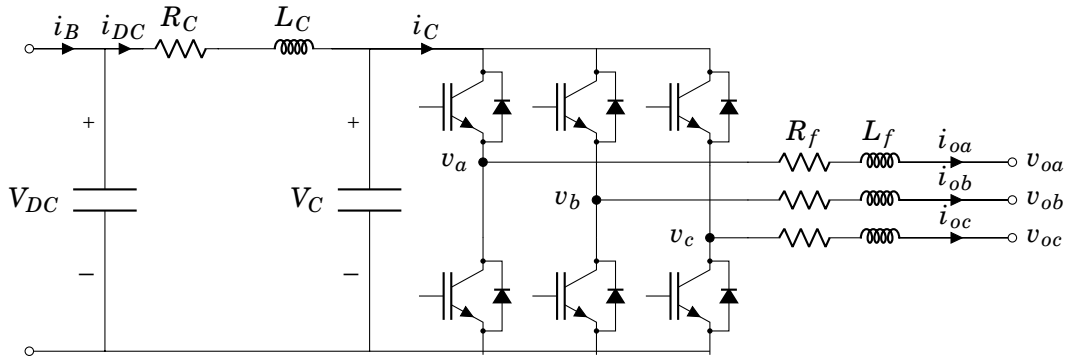

Figure 4.1: Circuit of VSC with a RL filter as ILC

Based on the circuit shown in Figure 4.1, (4.1) can be deducted using Kirchhoff's voltage law (KVL) at the DC side of the converter.

$$L_C \frac{d}{dt} i_{DC} = V_{DC} - R_C i_{DC} - V_C \tag{4.1}$$

Similarly, by using the Kirchoff's current law (KCL), (4.2) and (4.3) can be deducted for the DC side of the converter.

$$C_{DC} \frac{d}{dt} V_{DC} = i_B - i_{DC} \tag{4.2}$$

$$C_C \frac{d}{dt} V_C = i_{DC} - i_C \tag{4.3}$$

For the AC side of the converter KVL can be applied to derive the equations for the three phases:

$$L_f \frac{d}{dt} \begin{bmatrix} i_a \\ i_b \\ i_c \end{bmatrix} = \begin{bmatrix} v_a \\ v_b \\ v_c \end{bmatrix} - R_f \begin{bmatrix} i_{oa} \\ i_{ob} \\ i_{oc} \end{bmatrix} - \begin{bmatrix} v_{oa} \\ v_{ob} \\ v_{oc} \end{bmatrix}. \tag{4.4}$$

The equation representing the three-phase AC side of the converter can be transformed using the Park and Clarke transformations to d-q coordinates [104] resulting in (4.5). This transformation simplifies three-phase time-domain signals in a stationary phase coordinate system, to a rotating coordinate system. The d-component can be used to control active power and the q-component reactive component. Further details on this transformation our outside the scope of this research.

$$L_f \frac{d}{dt} \begin{bmatrix} i_d \\ i_q \end{bmatrix} = \begin{bmatrix} -R_f & \omega L_f \\ -\omega L_f & -R_f \end{bmatrix} \begin{bmatrix} i_d \\ i_q \end{bmatrix} + \begin{bmatrix} v_d \\ v_q \end{bmatrix} - \begin{bmatrix} v_{od} \\ v_{oq} \end{bmatrix} \tag{4.5}$$

For the simulation model in Simulink, the exact model as described here above, was implemented. Figure 4.2 displays the ILC, where the left side is connected to the DC bus and the right side to the AC bus.

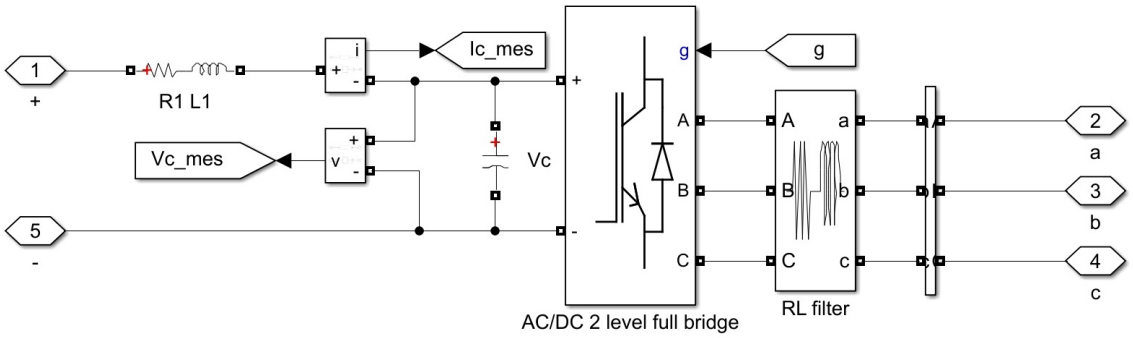

Figure 4.2: Representation of the ILC in Simulink

4.3 Solar PV array

The solar carports consist of PV panels which can be broken down into single PV cells. In Figure 4.3 the standard equivalent of the electric circuit of a PV cell is shown [105]. Based on the equivalent circuit of a solar cell, the mathematical model of a solar module can be derived as shown in (4.6), (4.7), where the parameters are defined in Table 4.1 [80, 81, 92, 106, 107].

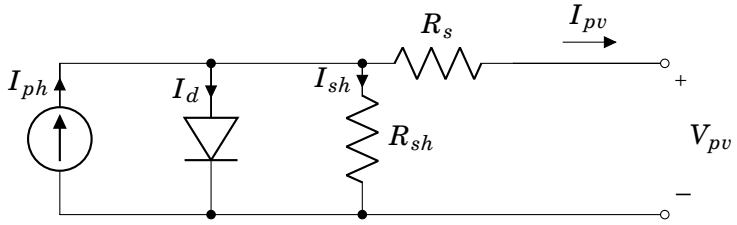

Figure 4.3: Equivalent circuit of solar PV cell

$$I_{pv} = I_{ph} - I_s \left[\exp\left(\frac{V_{pv} + I_{pv} R_s}{m V_t} \right) - 1 \right] - \frac{V_{pv} + I_{pv} R_s}{R_{sh}} \tag{4.6}$$

$$V_t = \frac{N_s k T}{q} \tag{4.7}$$

Table 4.1: Solar PV cell parameters

Symbol	Description	Value	Unit
I_{ph}	Photon current	6.468	[A]
I_s	Diode saturation current	$1.9162 * 10^{-10}$	[A]
R_{sh}	Shunt resistance	298.531	[Ω]
R_s	Series resistance	0.36964	[Ω]
m	Ideality factor	1.0903	[-]
N_s	Cells in series	96	[-]
k	Boltzmann constant	$1.38 * 10^{-23}$	[J/K]
T	Cell temperature	298.15	[K]
q	Electrical charge	$1.6 * 10^{-19}$	[C]

For the modeling of a solar panel the SPR-E20-327 by SunPower is used. This type was rated best in 2017 of all panels by SunPower [108]. Each type of panel has its own set of parameters for the individual cells, shown in Table 4.1. As a module, the SunPower solar panel has the characteristics as shown in Table 4.2. Corresponding to the characteristics of the solar panel the dynamics of the power point is shown in Figure 4.4. The total power output of the solar array depends on the number of panels as well as the irradiance the panels are receiving. Consequently, based on the reference system the solar carports contains 140 solar panels.

Table 4.2: SPR-E20-327 by SunPower characteristics

Description	Value	Unit
Maximum power	327.106	[W]
Efficiency	20.40	[%]
Open circuit voltage	65.1	[V]
Short-circuit current	6.46	[A]
Cells per module	96	[-]
Voltage at maximum power point	54.7	[V]
Current at maximum power point	5.98	[A]
Length	1.5580	[m]
Width	1.0460	[m]

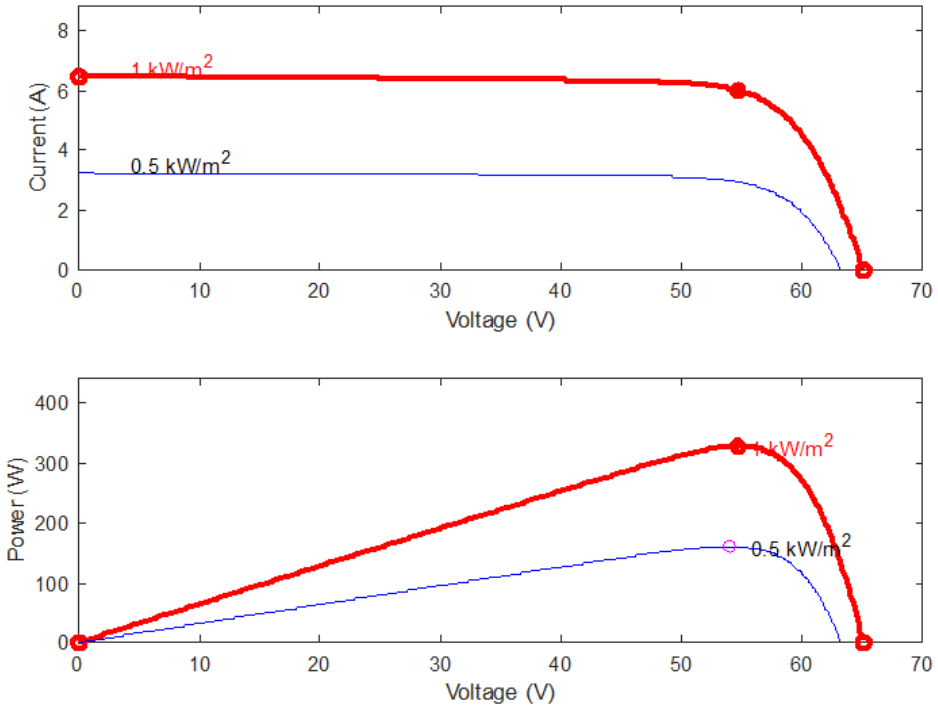

Figure 4.4: The I-V and P-V curves of the SPR-E20-327 solar panel at 25°C for 1000W/m^2 and 500W/m^2. The maximum power points are also shown on both curves in the P-V graph.

For the representation of the PV array in Simulink, an existing model is used provided by [96]. The plus and minus of the PV array in Figure 4.5 are connected to the right side of the boost converter in Figure 4.6. The boost converter is connected to the DC bus.

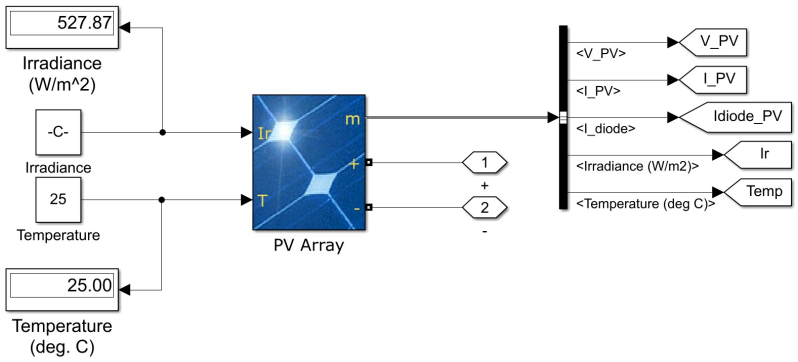

Figure 4.5: Representation of the PV array in Simulink

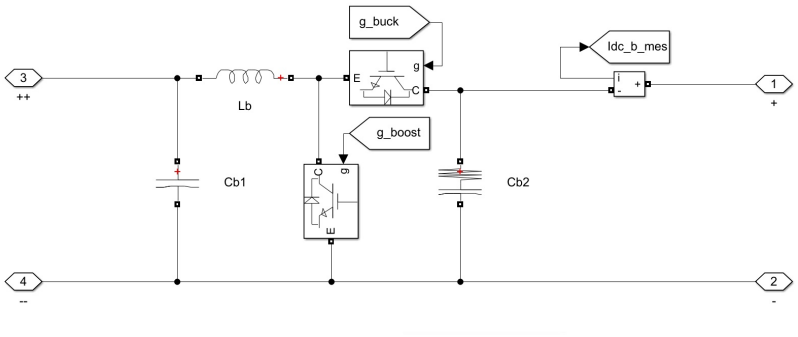

Figure 4.6: Representation of the boost converter for the PV array in Simulink

4.4 BESS

The DC side of the microgrid is fitted with a BESS to regulate the DC voltage. Mathematically the BESS can be represented by a set of equations. When the BESS is discharging and charging, respectively, (4.8) and (4.9) apply [109]. Both equations are very similar, only the equation for charging is a slightly altered version of the discharging equation. This alteration is made in the second term, which represents the polarization resistance. In case the discharge equation would also represent the charging behavior, the polarization resistance would theoretically go to infinity if the battery would be fully charged ($Q_{max} = Q(t)$). In practice this is not the case. Research has shown that the contribution of the polarization resistance is shifted by about 10% of the battery capacity resulting in (4.9) to describe the charging behavior [110].

All parameters depend on the actual BESS that is used. For the modeling, a BESS is used with the same storage capacity as a Tesla Powerpack, which is a lithium-ion battery with a capacity of 210 kWh [111]. All considered parameters definitions for the BESS are shown in Table 4.3.

$$V_{BESS}(t) = V_0 - K\frac{Q_{max}}{Q_{max} - Q(t)} i_{lf}(t) - K\frac{Q_{max}}{Q_{max} - Q(t)} Q(t) + Ae^{-BQ(t)} \tag{4.8}$$

$$V_{BESS}(t) = V_0 - K\frac{Q_{max}}{Q(t) + 0.1Q_{max}} i_{lf}(t) - K\frac{Q_{max}}{Q_{max} - Q(t)} Q(t) + Ae^{-BQ(t)} \tag{4.9}$$

Table 4.3: BESS parameters

Symbol	Description	Value	Unit
$V_{BESS}(t)$	Battery voltage over time		[V]
V_0	Constant voltage	395.791	[V]
K	Polarization constant	$4.7528 * 10^{-3}$	[V/Ah]
Q_{max}	Maximum battery capacity	575.3425	[Ah]
$Q(t)$	Extracted capacity		[Ah]
$i_{lf}(t)$	Low-frequency current dynamics		[A]
A	Exponential voltage	30.6512	[V]
B	Exponential capacity	0.10613	[1/Ah]

Based on the stated equations and the BESS parameters a discharge curve can be derived, as shown in Figure 4.7. The exponential area shows that the voltage drops rapidly

when the battery is fully charged. When the voltage drops slightly under the 400V the voltage becomes more stable the nominal voltage (365V) is reached. If the BESS is discharged further the voltage will drop rapidly again until it is fully discharged.

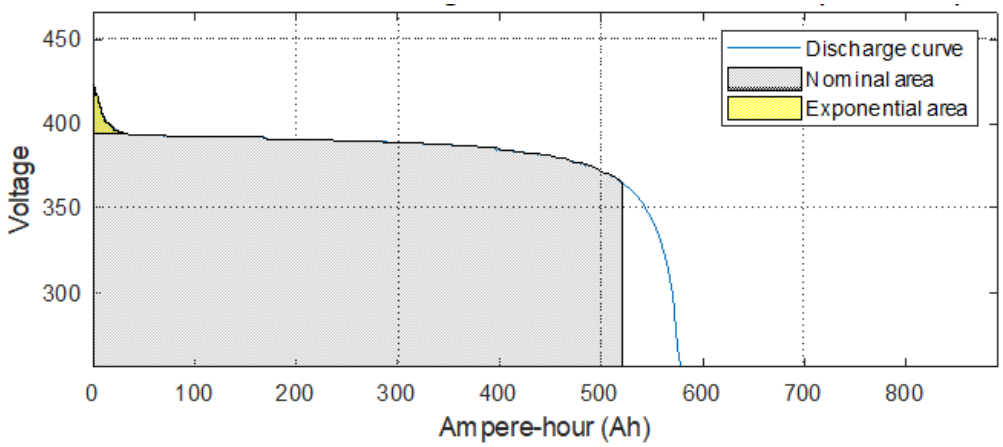

Figure 4.7: BESS discharge characteristics

To model the BESS in Simulink, the BESS model present in the Simulink library is used [109]. The right side of the BESS is connected to the bidirectional DC-DC converter (Figure 4.8), which is modeled based on [95]. The left side of the converter corresponds to the lower voltage side and the right side to the higher voltage side, which is the voltage at the DC bus (Figure 4.9).

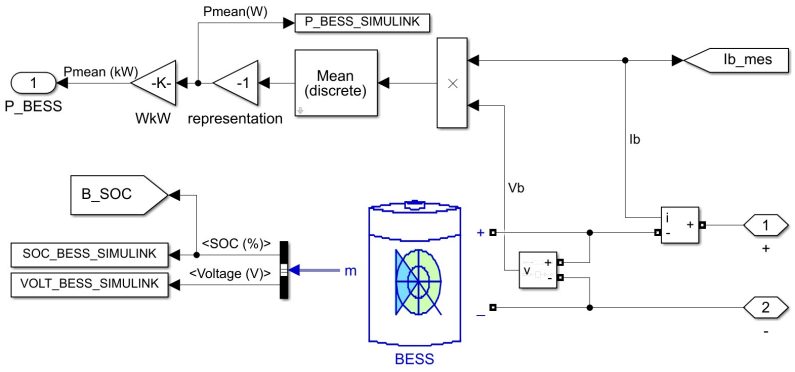

Figure 4.8: Representation of the BESS in Simulink

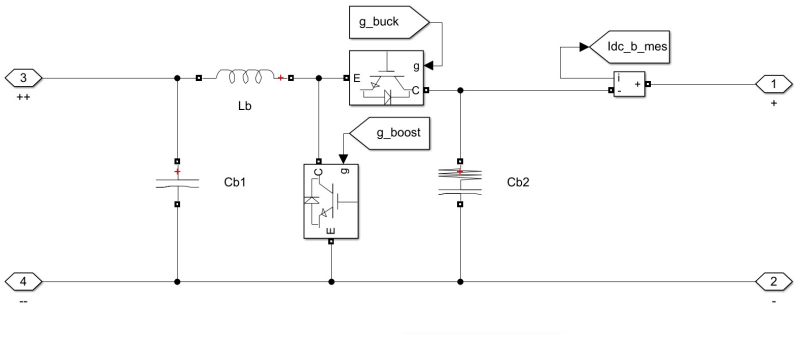

Figure 4.9: Representation of the bidirectional DC-DC converter for the BESS in Simulink

4.5 EVs

The last components that are part of the DC microgrid are EVs. Although, nowadays several different types of EVs exist, this research only includes full electric EVs with a lithium-ion battery. In contrast to the BESS, EVs are not always present in the system. To model different EVs in the hybrid microgrid, only three different types are considered. Each EV has its own battery characteristics. A Tesla Model S [112], a Nissan Leaf e+ [113], and a BMW i3s [114] are included and the details are shown in Table 4.4.

Throughout this research, the assumption is made that the details on the EVs are considered to be known for the controllers. These details include the arrival time, departure time, state of charge (SOC) upon arrival, and the desired SOC upon departure. This assumption is not considered to be a representation of reality. It is, however, made to simplify the system of interest. This assumption does allow for a first exploration of the potential of this system. Similarly, the different values set for the EV details are to some extent arbitrarily. They are primarily to illustrate the basic behavior of the EVs since this suffices for the purpose of this research. A more realistic approach to the role of the EVs is, therefore, outside the scope of this research.

Furthermore, the numbers of EVs considered throughout this research are depending on the setup of the different simulations. The number of EVs including the corresponding details is elaborated on per scenario.

Table 4.4: EV characteristics

Characteristic	**Tesla Model S**	**Nissan Leaf e+**	**BMW i3s**	**Unit**
Battery capacity	100	62	42.2	[kWh]
Charging capacity	200	100	49	[kW]
Discharging capacity	200	100	49	[kW]
Nominal voltage	365	365	365	[V]

For the mathematical model of an EV, similar to the BESS, the model of an lithium-ion battery is used [109]. When the EV is discharging Equation (4.10) applies and when charging Equation (4.11). The different battery characteristics of the individual EVs result also in different parameters to describe the behavior of the EVs.

$$V_{EV}(t) = V_0 - K\frac{Q_{max}}{Q_{max} - Q(t)} i_{lf}(t) - K\frac{Q_{max}}{Q_{max} - Q(t)} Q(t) + Ae^{-BQ(t)} \tag{4.10}$$

$$V_{EV}(t) = V_0 - K\frac{Q_{max}}{Q(t)+0.1Q_{max}}i_{lf}(t) - K\frac{Q_{max}}{Q_{max}-Q(t)}Q(t) + Ae^{-BQ(t)} \tag{4.11}$$

Table 4.5: EV parameters

Symbol	Tesla Model S	Nissan Leaf e+	BMW i3s	Unit
V_0	395.791	395.791	395.791	[V]
K	$9.981 * 10^{-3}$	$16.098 * 10^{-3}$	$23.652 * 10^{-3}$	[V/Ah]
Q_{max}	273.9726	169.8630	115.6164	[Ah]
A	30.6512	30.6512	30.6512	[V]
B	0.22288	0.35948	0.52814	[1/Ah]

The Simulink model for the EVs is rather similar to the model of the BESS (Figure 4.10). The right side of the BESS is connected to the bidirectional DC-DC converter (Figure 4.9), and also based on [95]. Also, the DC-DC converter, connecting the EV to the DC bus is similar, where the left side of the converter corresponds to the lower voltage side and the right side to the higher voltage side.

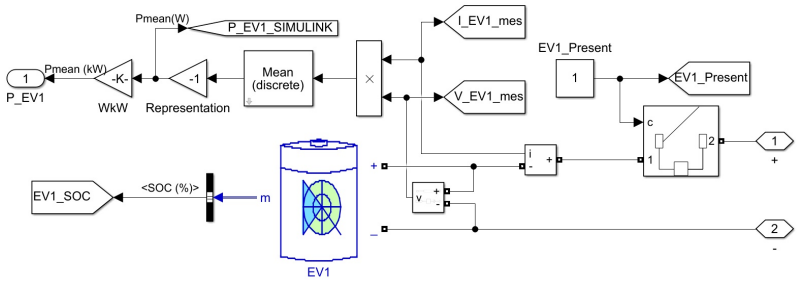

Figure 4.10: Representation of an EV in Simulink

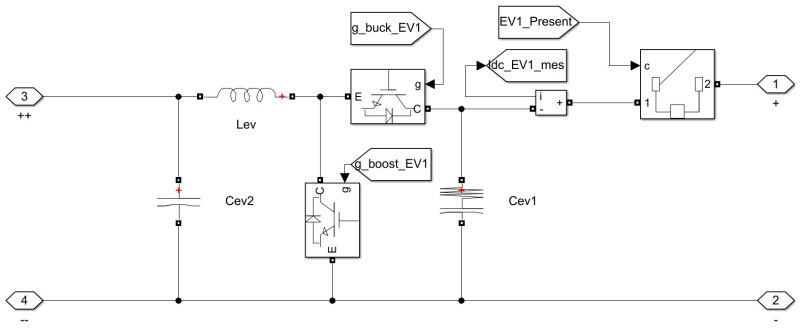

Figure 4.11: Representation of the bidirectional DC-DC converter for an EV in Simulink

4.6 AC load

On the AC side of the microgrid an AC load is modeled that represents the AC power demand. In more practical terms this means that it represents the demand of the neighboring building, facility or office. It is a dynamic purely resistive load that changes over time with, generally, daily, weekly and seasonal trends. The AC load is connected to the AC bus together with the ILC and the utility grid connection. As shown in Figure 4.12, the AC load is represented by R_{load} and i_o and i_g are, respectively, the current flow from the converter and to the grid.

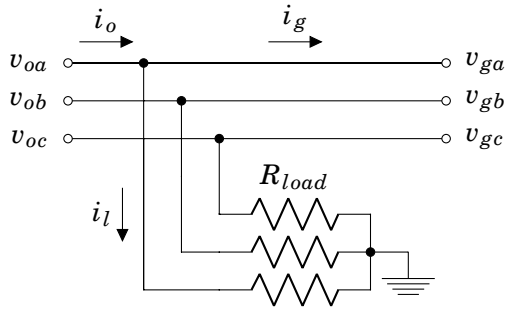

Figure 4.12: Circuit of the AC load

Based on the circuit of the AC load the mathematical model can be derived. For the three-phase current Equation (4.12) can be formulated and transformed using the Park and Clarke transformations [104] to d-q coordinates in Equation (4.13). The AC load is assumed to only use active power this means that the reactive component is zero ($i_{lq} = 0$).

$$\begin{bmatrix} i_{la} \\ i_{lb} \\ i_{lc} \end{bmatrix} = \frac{1}{R_{load}} \begin{bmatrix} v_{oa} \\ v_{ob} \\ v_{oc} \end{bmatrix} = \begin{bmatrix} i_{oa} \\ i_{ob} \\ i_{oc} \end{bmatrix} - \begin{bmatrix} i_{ga} \\ i_{gb} \\ i_{gc} \end{bmatrix} \tag{4.12}$$

$$\begin{bmatrix} i_{ld} \\ i_{lq} \end{bmatrix} = \frac{1}{R_{load}} \begin{bmatrix} v_{od} \\ v_{oq} \end{bmatrix} = \begin{bmatrix} i_{od} \\ i_{oq} \end{bmatrix} - \begin{bmatrix} i_{gd} \\ i_{gq} \end{bmatrix} \tag{4.13}$$

The simple model of the AC load results also in simple Simulink model (Figure 4.13). For the load, a dynamic load from the Simulink library is used [115] and it is directly connected to the AC bus. The amount of power that is required by the load is based on the hourly demand of a facility in California [116]. Its electricity demand is normalized such that only a pattern is left. By combining this pattern with the demand required by the reference system, as defined in section 2.4.2, a representative demand pattern acquired.

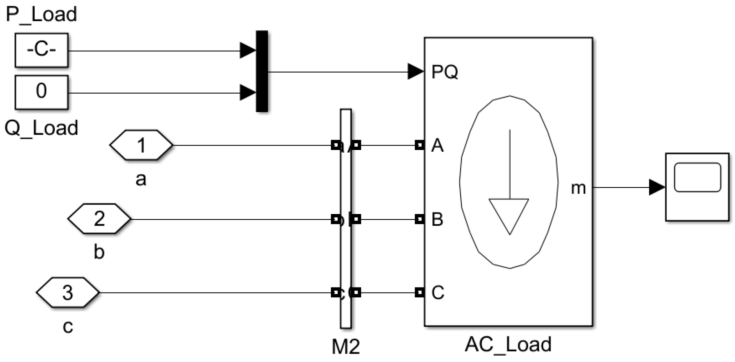

Figure 4.13: Representation of the AC load in Simulink

4.7 Utility grid

The last component at the AC side of the microgrid is the utility grid connection. It operates as a slack bus for the AC bus. This means that power shortages or surpluses at the AC bus are compensated by the utility grid. Also, the utility grid determines the frequency and voltage at the AC bus. Due to the complexity of the utility grid, the modeling hereof is out of the scope of this research.

To simulate the utility grid, an existing model by [96] is used. Figure 4.14 displays the representation of the grid, where the left side is connected to the AC bus.

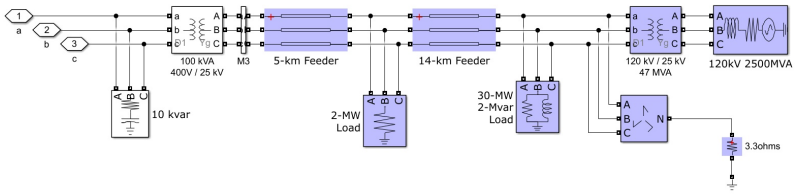

Figure 4.14: Representation of the utility grid in Simulink

4.8 Simulink model

In the previous sections for each component, the Simulink model is shown. Each component is interconnect as part of the hybrid microgrid. In Figure 4.15 an overview is provided of the complete Simulink model.

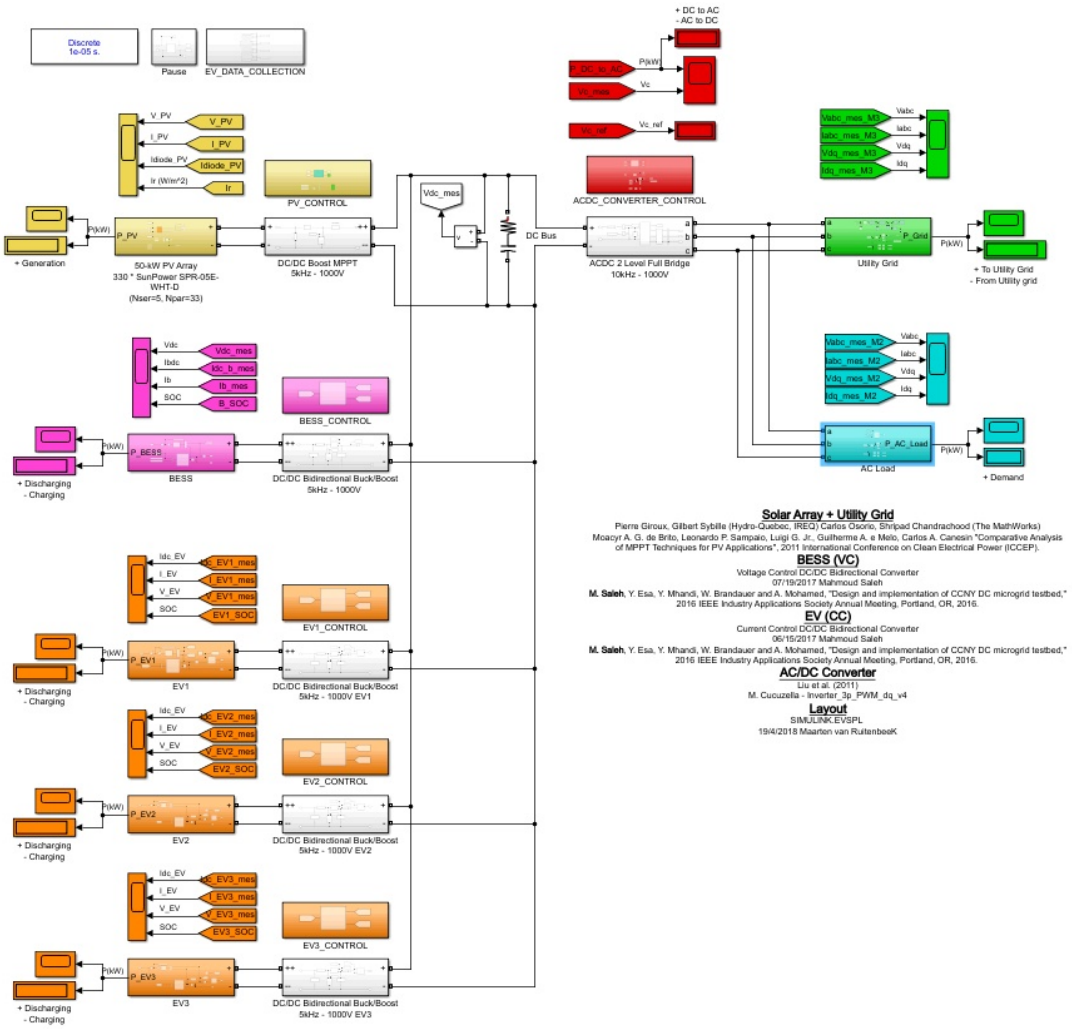

Figure 4.15: Representation of the hybrid microgrid in Simulink

Chapter 5

Control strategy

A two-level control strategy is used to control the hybrid microgrid. The lower-level control layers consists of several individual PI controllers each with different control objectives. These controllers, except for the boost converter interfacing the solar array, receive set-points from the higher-level control, which uses MPC to determine these. Both control layers will be discussed individually in this section.

5.1 Lower-level control

5.1.1 ILC

The ILC is a critical component of the hybrid microgrid. It has several responsibilities and therefore multiple control objectives. First of all, the ILC is responsible to regulate the active power flow between the DC and AC side of the hybrid microgrid. In line with this, the ILC takes care of the synchronization of the voltage with the alternating voltage of the AC bus. For this, Phase-Locked Loop (PLL) is used [117]. Further details on the PLL are outside the scope of this research. The last objective of the ILC is to regulate the reactive power to zero, which means that the q-component of the three-phase current is regulated towards zero ($i_q = 0$).

To regulate the power transfer via the ILC, the voltage on the DC side of the ILC is regulated to enable current to flow between the DC bus and the ILC, as was discussed in section 4.2. Therefore, the reference for this voltage (V_C^*) needs to be determined based on the power transfer setpoint provided by the higher-level controller (P_{ILC}^*). This is done by considering (4.1) in steady state. It becomes (5.1), where $\bar{V}_{DC}$, $\bar{i}_{DC}$ and $\bar{V}_C$ are the steady state values. For the value of the DC bus voltage, the average is taken, instead of the reference value (V_{DC}^*). In case of a possible small offset in the DC bus voltage, taking the average value enables the ILC to adapt to this. Consequently, it can be rewritten into (5.2).

$$0 = \bar{V}_{DC} - R_C \bar{i}_{DC} - \bar{V}_C \tag{5.1}$$

$$\bar{i}_{DC} = \frac{\bar{V}_{DC} - \bar{V}_C}{R_C} \tag{5.2}$$

Furthermore, (4.3) is also considered in steady state resulting in (5.3) and (5.4). By combining this with (5.2) one obtains (5.5).

$$0 = \bar{i}_{DC} - \bar{i}_C \tag{5.3}$$

$$\bar{i}_{DC} = \bar{i}_C \tag{5.4}$$

$$\frac{\bar{V}_{DC} - \bar{V}_C}{R_C} = \bar{i}_C \tag{5.5}$$

The reference power transferred via the ILC in steady state can be defined as:

$$P^*_{ILC} = \bar{V}_C * \bar{i}_C = \bar{V}_C * \frac{\bar{V}_{DC} - \bar{V}_C}{R_C}, \tag{5.6}$$

resulting in a term for $\bar{V}_C$ in steady state:

$$\bar{V}_C = \frac{\bar{V}_{DC} \pm \sqrt{\bar{V}^2_{DC} - 4R_C P^*_{ILC}}}{2}. \tag{5.7}$$

Eq. (5.7) provides two solutions that are mathematically correct. Yet, when considering $R_C > 0$ and $\bar{V}_{DC} > 0$, the solution with the minus term will never allow $\bar{V}_C$ to exceed $\bar{V}_{DC}$. This is, however, required to enable a bidirectional power flow based on (5.5). Since the solution with the plus term does allow the bidirectional power flow, this solution is only considered further on.

Moreover, since $\bar{V}_C$ is a steady state value, it is set as the reference value V^*_C. Consequently, the ILC calculates this reference value according (5.8), based on the setpoint P^*_{ILC} provided for by the higher-level controller, which will be discussed in section 5.2, .

$$V^*_C = \frac{\bar{V}_{DC} + \sqrt{\bar{V}^2_{DC} - 4R_C P^*_{ILC}}}{2}. \tag{5.8}$$

For the ILC a cascaded control loop is used based on [7] and is shown in Figure 5.1. The first PI controller retrieves the error of the voltage at the DC side of the ILC. The output of this controller is corrected by -1 to represent the correct direction of the power flow and acts as the reference value for the direct component of the AC current. The next two PI controllers correct for the differences between i_d and i_q and their reference values respectively. Hereafter, the controller outputs are corrected with the actual voltage and a feedforward loop, where ω is the AC frequency and L_f the inductance of the ILC filter. Finally, V_{cd} and V_{cq} are transformed back into a three-phase signal, to determine the gate signals for the six switches of the ILC by using PWM.

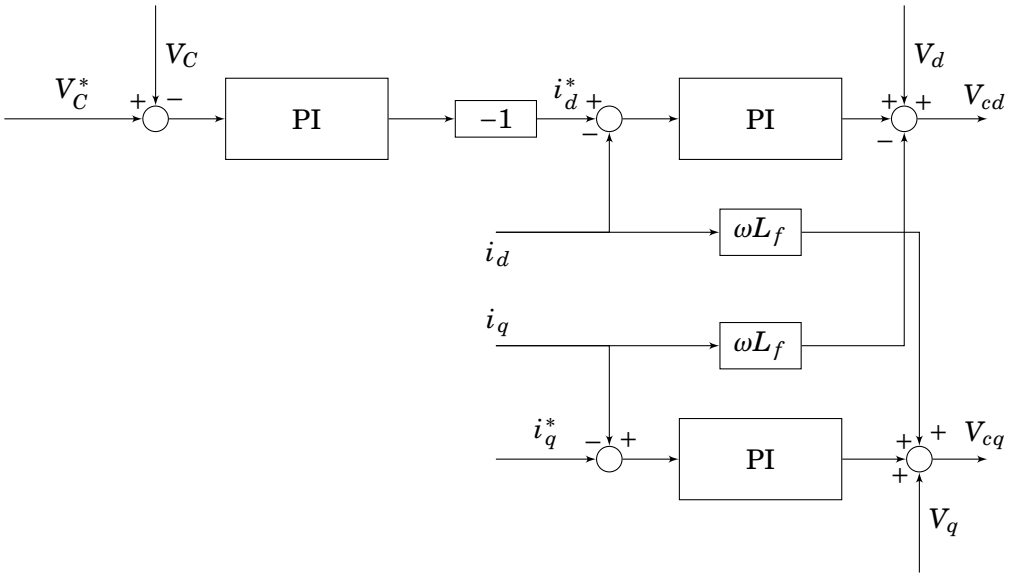

Figure 5.1: Control scheme of the ILC, where V_C, V_d, V_q, i_d, and i_q are the actual values.

5.1.2 Solar array

The solar array is interfaced with a boost converter as discussed in section 3.3.2. It is responsible for ensuring the array to operate at MPP. Two MPPT techniques, the P&O and the IC technique, have been discussed in section 3.4 of which the IC technique is selected. For the simulation an existing model by [96] is used, which produces the gate signal regulating the switch of the boost converter. Some alterations had to be made to make suitable for the hybrid microgrid. This boost converter operates independently and is not affected by the other controllers or the higher-level controller.

5.1.3 BESS

A buck-boost converter is connecting the BESS to the DC bus. The converter enables a bidirectional power flow, either charging or discharging the BESS. The control objective is to regulate the DC bus voltage to its reference value ($V_{DC}^* = 1000V$). The BESS is in this case in VCM. Given the discussed buck-boost converter in section 3.3.3, V_{DC} corresponds to the high voltage side and V_{BESS} to the low voltage side. Depending on the actual voltage, the buck-boost converter operates in either buck or boost mode. This means that when the bus voltage is higher than its reference the converter is in buck mode and therefore charging the battery. In case the bus voltage is lower the opposite applies. The output signal is in both cases transformed into a gate signal for the corresponding switch.

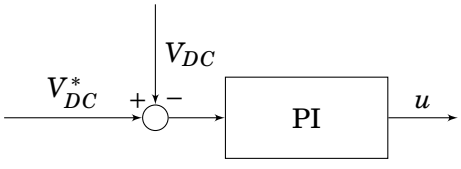

Figure 5.2: Control scheme of the BESS, where V_{DC} is the actual voltage and y the output signal.

5.1.4 EV

Similar to the BESS, an EV is also connected to the DC bus via a buck-boost converter. The control objective of the buck-boost converter for an EV is, however, different. The converter is in this case responsible for a stable current flow to or from the EV battery and is therefore in CCM (Figure 5.3). The reference value for the current (i^*_{EV}) is based on the setpoint provided by the higher level controller. Based on the direction of the current the EV acts either as a load or generator in the DC microgrid.

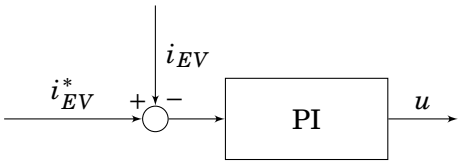

Figure 5.3: Control scheme of the EV, where i_{EV} is the actual current to or from the EV and y the output signal.

5.2 Higher-level control

The higher-level controller is a centralized control scheme that uses MPC to control the hybrid microgrid. It uses a simplified model of the hybrid microgrid by only considering the power flows (Figure 5.4) to predict the behavior of the hybrid microgrid. Based on this model, it provides setpoints, P^*_{ILC}, P^*_{BESS} and I^*_{EV} to the ILC, BESS, and the EVs respectively. The main objective of this controller, while determining these setpoints, is to minimize the power exchange with the utility grid. Next, shortly an overview of all different parameters will be provided (Table 5.1), after which the MPC controller is introduced. The latter is discussed in three parts: the MPC model, the objective and the constraints.

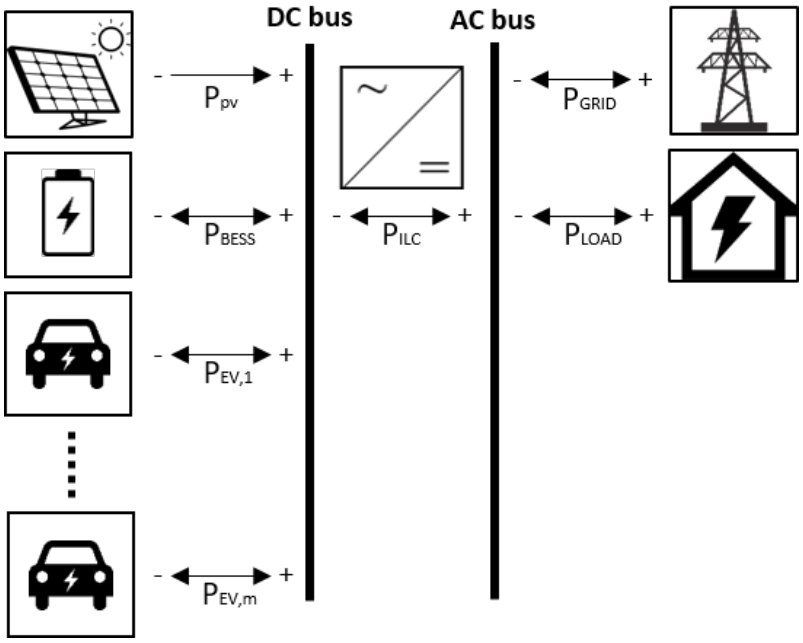

Figure 5.4: Simplified MPC model of the hybrid AC/DC microgrid.

Table 5.1: Parameters for MPC

Symbol	Description
Indices	
$t \in \{1,...,T\}$	Index of time instants
$k \in \{1,...,N\}$	Index of prediction time instants
$m \in \{1,...,M\}$	Index of EVs
Variables	
$SOC_{BESS}(t)$	SOC of the BESS at time t
$SOC_{BESS,0}$	SOC of the BESS at $t = 0$
$C_{BESS,cap}$	Storage capacity of the BESS
η_{BESS}	BESS efficiency
$SOC_{BESS,max}$	Maximum SOC of the BESS
$SOC_{BESS,min}$	Minimum SOC of the BESS
$P_{BESS,max}$	Discharging capacity of the BESS
$P_{BESS,min}$	Charging capacity of the BESS
$P^*_{BESS}(t)$	Setpoint for $P_{BESS}(t)$ at time t
$SOC_{EV,m}(t)$	SOC of EV m at time t
$SOC_{EV,m,arr}$	Initial SOC of EV m upon arrival
$C_{EV,m,cap}$	Storage capacity of EV m
$\eta_{BESS,m}$	Efficiency of the battery of EV m
$SOC_{EV,m,des}$	Desired minimum SOC of EV m
$P_{EV,m,max}$	Discharging capacity of EV m
$P_{EV,m,min}$	Charging capacity of EV m
$t_{EV,m,arr}$	Time of arrival of EV m
$t_{EV,m,dep}$	Time of departure of EV m
$V_{EV,m}(t)$	Voltage of EV m at time t
$i^*_{EV,m}(t)$	Setpoint for current of EV m at time t
$P_{ILC}(t)$	The power transfer via the ILC at time t
$P^*_{ILC}(t)$	Setpoint for $P_{ILC}(t)$ at time t
$P_{ILC,max}$	Capacity of the ILC for power transfer from DC to AC
$P_{ILC,min}$	Capacity of the ILC for power transfer from AC to DC
P_{PV}	Generation pattern of the solar array
P_{LOAD}	Demand pattern of the AC load
$\hat{P}_{PV}(k)$	Predicted power generated by the PV array at time k
$\hat{P}_{BESS}(k)$	Predicted power exchanged with the BESS at time k
$\hat{P}_{EV,m}(k)$	Predicted power exchanged with EV m at time k
$\hat{P}_{ILC}(k)$	Predicted power exchanged via the ILC at time k
$\Delta\hat{P}_{ILC}(k)$	Predicted increase or decrease of $\hat{P}_{ILC}(k)$ at time k
$\hat{P}_{GRID}(k)$	Predicted power exchanged with the grid at time k
$\hat{P}_{LOAD}(k)$	Predicted power consumed by the AC load at time k
$\hat{SOC}_{BESS}(k)$	Predicted SOC of the BESS at time k
$\hat{SOC}_{EV,m}(k)$	Predicted SOC of EV m at time k

5.2.1 MPC controller

The MPC controller requires several initial inputs before it can run the model of the hybrid microgrid and solve the optimization problem (Figure 5.5). Initially, the controller retrieves the PV pattern (P_{PV}), the load pattern (P_{LOAD}) and data on the EVs to simplify the controller design and operation. This data includes the arrival time, departure time, and the desired state of charge. This assumption is made to simplify the controller design. A more detailed approach is not considered to be required for the purpose of this research. Next to these initial variables, the MPC controller receives for every iteration the actual power transfer over the ILC ($P_{ILC}(t)$), the SOC of the BESS ($SOC_{BESS}(t)$) and the SOC of the EVs ($SOC_{EV,m}(t)$). Once the optimization problem is solved, $\Delta\hat{P}_{ILC}$, $\hat{P}_{BESS}$, and $\hat{P}_{EV,m}$ are given as the output. These outputs are, however, not the setpoints for the individual components. The setpoints for the components are defined in (5.9), (5.10), and (5.11). For setpoint of the ILC, the previous setpoint is corrected with $\Delta\hat{P}_{ILC}$. The ILC will then deduce the reference voltage according to (5.8).

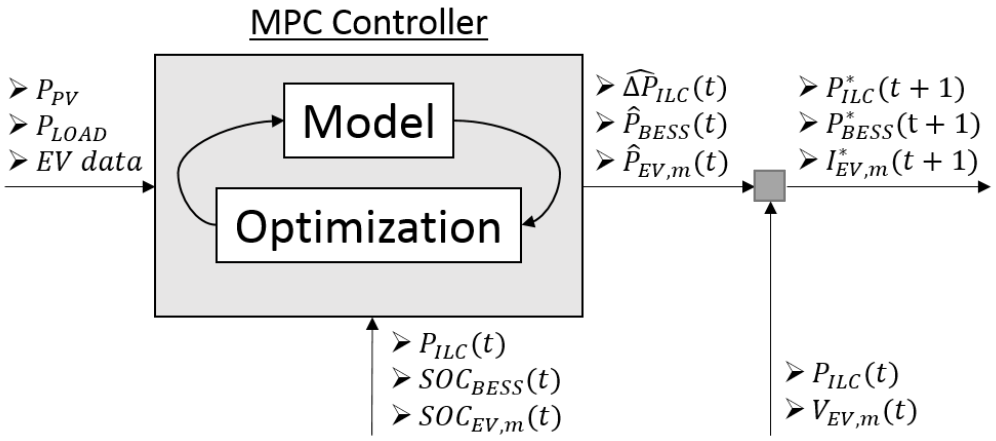

Figure 5.5: Schematic of inputs and output of the MPC model, where $m = \{1,...,M\}$.

$$P^*_{ILC}(t+1) = P_{ILC}(t) + \Delta\hat{P}_{ILC}(t) \quad \forall t \tag{5.9}$$

$$P^*_{BESS}(t+1) = \hat{P}_{BESS}(t) \quad \forall t \tag{5.10}$$

$$I^*_{EV,m}(t+1) = \frac{\hat{P}_{EV,m}(t)}{V_{EV,m}(t)} \quad \forall t, m \tag{5.11}$$

The setpoint for the BESS (P^*_{BESS}) is actually a value that will not be used by the BESS directly. For the design of the controller of the BESS, it has been chosen to regulate the power transfer to and from the BESS indirectly. This is done by exploiting the main control objective of the BESS, regulating the DC bus voltage. Generally, when $P^*_{BESS}(t+1) \neq 0$, a surplus or shortage of power at the DC bus would arise due to the balance of power. Consequently, the voltage will either increase or decrease. However, due to its main control objective, the BESS will react to these voltage changes and, thereby, indirectly power is transferred to or from the BESS.

The reason for regulating the power as described is twofold. Firstly, the complexity of the controller of the BESS would increase if the power was controlled directly. Next to the current control loop that regulates the DC voltage, the controller would require an

extra control loop to regulate the power flow. Secondly, in case the controller would have these two control objectives, they may contradict each other. This is the result of using a simplified model of the hybrid microgrid as part of the MPC controller. Since this model does not include any losses, the energy balance in the microgrid may not correspond to the actual situation. Consequently, the MPC controller could dictate that power should be transferred to the BESS, while actually the BESS should be supplying power to maintain the DC voltage and the actual balance of power at the DC bus or vice versa.

To determine the setpoint of the EVs at $t+1$, the voltage of the EV at t used by applying the power law. Considering the time interval of the MPC controller, the SOC of the EV will not change by large amounts. Together with the voltage behavior of the EVs, it is assumed that the voltage of the battery remains rather stable over one time interval. For this reason $V_{EV,m}(t)$ is used instead of $V_{EV,m}(t+1)$.

5.2.2 The MPC model

A simplified model, based on the active power balance within the microgrid, is used as the MPC model. This means for the DC side of the hybrid microgrid that the PV generation should be in balance with the total power exchange with the BESS, EVs, and the AC side. Similarly, the power balance applies for the AC part of the microgrid. This means that the AC loads should either be supplied with DC power via the ILC or by the utility grid.

First of all, the dynamics of the BESS need to be defined. The power flowing to or from the BESS affects the SOC of the BESS. The SOC of the BESS is determined by adding the previous SOC of the BESS to the previous power flow to or from the BESS:

$$\hat{SOC}_{BESS}(k+1) = \hat{SOC}_{BESS}(k) + c_{BESS}\hat{P}_{BESS}(k) \quad \forall k, \tag{5.12}$$

Coefficient c_{BESS} can be expressed as $c_{BESS} = \eta_{BESS}T/C_{BESS,cap}$. Similarly, to the BESS, the SOC of the EVs at each time instant can also be described based on the SOC and the power flow at the previous time instant. For every EV_m, $m = 1,...,M$, the following equation can be stated:

$$\hat{SOC}_{EV,m}(k+1) = \hat{SOC}_{EV,m}(k) + c_{EV,m}\hat{P}_{EV,m}(k) \quad \forall k, \tag{5.13}$$

where coefficient $c_{EV,m}$ represents $c_{EV,m} = \eta_{EV,m}T/C_{EV,m,cap}$. Furthermore, the EVs are not always considered present in the microgrid. In this case, the power exchange with this particular EV is forced to zero.

Next, the power transfer by ILC is defined. The power transferred by the ILC is determined by surplus or shortage of power at the DC side of the hybrid microgrid. A positive $\hat{P}_{ILC}$ means power is transferred from the DC bus to the AC bus and a negative $\hat{P}_{ILC}$ means power is provided to the DC bus from the AC bus. Therefore, the power transfer via the ILC at each time instant can be represented as:

$$\hat{P}_{ILC}(k+1) = \hat{P}_{ILC}(k) + \Delta\hat{P}_{ILC}(k) \quad \forall k \tag{5.14}$$

such that:

$$\hat{P}_{ILC}(k) = \hat{P}_{PV}(k) + \hat{P}_{BESS}(k) + \sum_{m=1}^{M} \hat{P}_{EV,m}(k). \tag{5.15}$$

No further dynamics are present in the AC side of the microgrid. As can be seen in (5.16), a simple relation is defined for the power exchange with the grid, especially since the demand from the AC load is considered to be known.

$$P_{GRID}(k) = P_{ILC}(k) - P_{LOAD}(k) \quad \forall k \tag{5.16}$$

Finally, all dynamics can be represented in state space equations. The set of equations depend on the number of EVs ($m = 1, ..., M$). Therefore, the following can be stated:

$$\begin{cases} x_1(k+1) = x_1(k) + u_1(k) \\ x_2(k+1) = x_2(k) + c_{BESS} u_2(k) \\ x_{m+2}(k+1) = x_{m+2}(k) + c_{EV,m} u_{m+2}(k) \\ y_1(k) = x_1(k) \\ y_2(k) = x_2(k) \\ y_{m+2}(k+1) = x_{m+2}(k), \end{cases} \tag{5.17}$$

where $x_1 = P_{PV} + u_2 + u_3$ holds, and where

$$x = \begin{bmatrix} \hat{P}_{ILC} \\ \hat{SOC}_{BESS} \\ \hat{SOC}_{EV,m} \end{bmatrix} \in X \subset \mathbb{R}^{M+2}, \tag{5.18}$$

is the state vector. The input vector is then:

$$u = \begin{bmatrix} \hat{\Delta P}_{ILC} \\ \hat{P}_{BESS} \\ \hat{P}_{EV,m} \end{bmatrix} \in U \subset \mathbb{R}^{M+2} \tag{5.19}$$

and the output $y = x, \in \mathbb{R}^{M+2}$.

5.2.3 Objective

The objective of the MPC is to minimize the power exchange with the grid. The reason is twofold. Firstly, consuming less power from the utility grid reduces the utility bill costs. Secondly, minimizing the supply of power to utility grid maximizes the consumption of internal supply. This objective can be represented mathematically as the first term in the following objective function:

$$J(t) = w_1 \sum_{k=1}^{N} \hat{P}^2_{GRID}(t+k|t) + w_2 \sum_{m=1}^{M} \sum_{k=1}^{N} \hat{P}^2_{EV,m}(t+k|t) + w_3 \sum_{k=1}^{N} \hat{P}^2_{BESS}(t+k|t). \tag{5.20}$$

The second and third term are only present to prevent unnecessary power transfers, as well as it smooths the power transfer over longer periods of time. Also, the three different terms are multiplied with a weight ($w = \{w_1, w_2, w_3\}$). These weights enable to prioritize the three different terms.

5.2.4 Constraints

For the optimization problem several constraint can be defined. First of all, a maximum and minimum SOC of the BESS is defined to represent the physical limits of the BESS. Also, a maximum and minimum charge are defined to resemble the discharge and charge capacity, respectively:

$$\begin{array}{llll} 0 & \leq \hat{SOC}_{BESS}(k) & \leq 1 & \forall k \\ P_{BESS,min} & \leq \hat{P}_{BESS}(k) & \leq P_{BESS,max} & \forall k. \end{array} \tag{5.21}$$

Also, for the EVs, $m = 1, ..., M$, maximum and minimum SOCs are defined in constraints. The minimum is considered to be dynamic, such that it enforces the EV to charge and depart with a minimal desired SOC. Furthermore, similar to the BESS, the maximum and minimum charge represent the discharge and charge capacity:

$$\begin{array}{llll} SOC^*_{EV,m}(k) & \leq S\hat{O}C_{EV,m}(k) & \leq 1 & \forall k \\ P_{EV,m,min} & \leq \hat{P}_{EV,m}(k) & \leq P_{EV,m,max} & \forall k. \end{array} \tag{5.22}$$

The reference SOC ($SOC^*_{EV,m}$), depends on the time of arrival and departure, and the difference between the initial and desired SOC:

$$SOC^*_{EV,m}(k) = SOC_{EV,m,arr} + \Delta SOC_{EV,m}(t + k - t_{EV,m,arr}) + \quad \forall k \tag{5.23}$$

where

$$\Delta SOC_{EV,m} = \frac{SOC_{EV,m,des} - SOC_{EV,m,arr}}{t_{EV,m,dep} - t_{EV,m,arr}}. \tag{5.24}$$

The reference state of charge is at $t_{EV,m,dep}$ at the desired SOC for each EV. The remaining capacity of the EV can be used to store excess power. Furthermore, the desired SOC is considered to be feasible, taking the maximum charging capacity into consideration.

For the ILC also a maximum and minimum capacity is set to limit, respectively, the transfer of power from DC to AC or from AC to DC:

$$P_{ILC,min} \quad \leq \hat{P}_{ILC}(k) \quad \leq P_{ILC,max} \quad \forall k. \tag{5.25}$$

Lastly, constraints can be derived from the MPC model, based on the preservation of energy for the DC side of the microgrid:

$$\hat{P}_{ILC}(k) = \hat{P}_{PV}(k) + \hat{P}_{BESS}(k) + \textstyle\sum_{m=1}^{M} \hat{P}_{EV,m}(k) \quad \forall k, \tag{5.26}$$

and for the AC side of the microgrid:

$$\hat{P}_{GRID}(k) = \hat{P}_{ILC}(k) - \hat{P}_{LOAD}(k) \quad \forall k. \tag{5.27}$$

Chapter 6

Scenarios

In the previous sections the simulation model and the control strategy of the hybrid microgrid were proposed. This section describes four sets of scenarios in which different aspects of the hybrid microgrid and its controller design are reviewed. After each scenario description and sub-scenario description, the results will be discussed. In the first set of scenarios, the different lower-level converters are discussed, to see whether they operate according to their design objectives. Second, the centralized MPC converter is analyzed to gain insight in its working. Hereafter, both control layers are combined and the two-level control strategy is evaluated. These three sets of scenarios discuss the actual working of the designed control strategy. Finally, by using the higher-level controller, the potential of the hybrid microgrid is investigated in a practical case study.

6.1 Scenario 1: Lower-level controllers

The first set of scenarios is used to view the working of the lower-level controllers. It is of importance for the hybrid microgrid as a whole that each controller is stable and operates according their control objectives. In case the designed controllers do not operate properly, they can harm the components in the system or cause the microgrid to malfunction.

6.1.1 Simulation setup

To test the different controllers, the hybrid microgrid is first simulated under neutral circumstances, as described in Table A.1 in the appendix. This starts at $t = 0$ till $t = 1$. Hereafter, the response of each converter is investigated under specified changes in the system in the form of a step response. These changes are different for each converter and can be direct or indirect depending on the objective of the controller. For simplicity, only one EV is considered for these scenarios as this suffices to investigate the design of the EV converters.

6.1.2 ILC

The ILC main responsibility is to control the power transfer via the ILC by controlling the voltage on the DC side (V_c). This power flow can go in both directions and the reference value that defines this flow is normally set by the higher-level controller. This power flow is controlled by controlling the direct component of I_d to its reference value which is based on the V_c error. Next to this, the ILC is also responsible for regulating the reactive power to zero. To investigate the effect of different setpoints, the scenarios as described in Table 6.1 are simulated. The starting reference value is considered to be zero for every scenario.

For these scenarios, V_c, I_d, and I_q are of interest as these terms are being controlled by the controller of the ILC.

Table 6.1: Different scenarios setups for the ILC

Scenario	$P^*_{ILC}(t)$	$P^*_{ILC}(t+1)$	**Conversion**
ILC20kW	0	20	DC to AC
ILC-20kW	0	-20	AC to DC
ILC10kW	0	10	DC to AC
ILC-10kW	0	-10	AC to DC
ILC5kW	0	5	DC to AC
ILC-5kW	0	-5	AC to DC

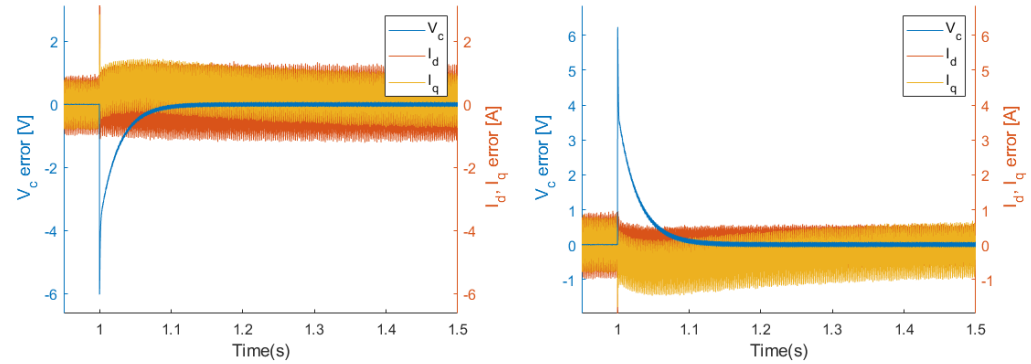

(a) Scenario ILC20kW

(b) Scenario ILC-20kW

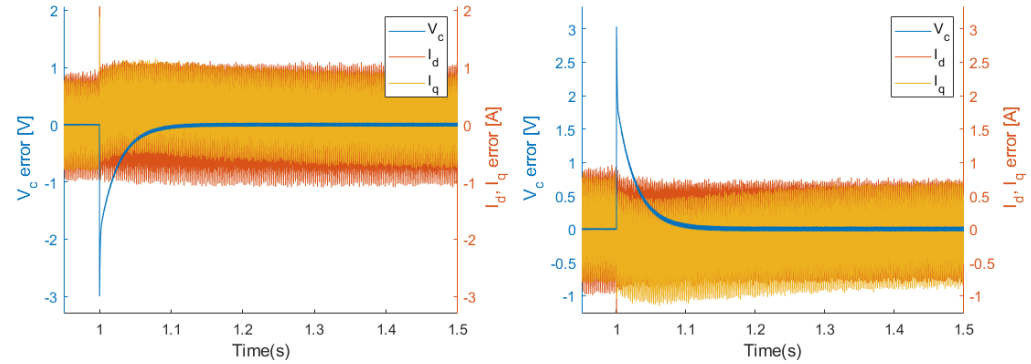

(c) Scenario ILC10kW

(d) Scenario ILC-10kW

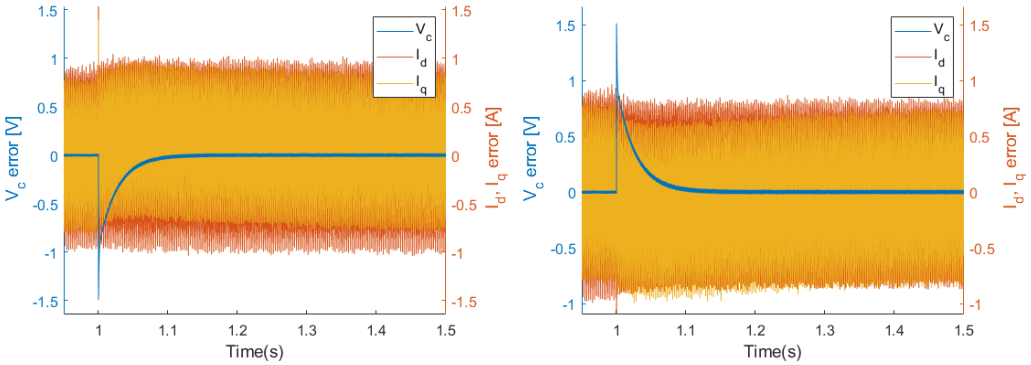

(e) Scenario ILC5kW

(f) Scenario ILC-5kW

Figure 6.1: The error of V_c, I_d and I_q for different ILC scenarios.

6.1.2.1 Results

In Figure 6.1 the results are shown for the ILC for the different defined scenarios. First of all, it must be mentioned that in all scenarios V_C, I_d and I_q converge nicely. The voltage, however, is clearly converging faster than the direct and indirect current. It only requires less than 0.1 second in all cases to converge. Both I_d and I_q require significantly more time to reach steady state than V_c. Also, both errors are affected by the amount of power that is transferred over the ILC. A higher power exchange results, logically, in a longer time the ILC requires to converge. Furthermore, it is noticeable that there is no clear difference

between the two modes of the ILC. Conversion from AC to DC and from DC to AC is only clearly reflected in having opposite errors.

6.1.3 BESS

The BESS is designed to regulate the DC bus voltage to 1000V at all times. This means in case of a power shortage or surplus on the DC side of the hybrid microgrid, the BESS responds. A shortage or surplus would otherwise affect the DC voltage. The higher-level control is responsible for maintaining the power balance at the DC bus. However, it can intentionally create a surplus or shortage at the DC side of the microgrid to indirectly control the power exchange with the BESS. The response of the BESS to the shortage or surplus depends partially on the speed of the other converters to reach there new setpoints. Therefore, to be able to test the working and the robustness of the BESS, a current source is connect to the DC bus to provide a sudden increase of current to the DC bus at t = 1. The power from the EV and the solar array will for these scenarios be balanced by the ILC (P^*_{ILC} = 19.14kW), such that the there is roughly a balance of power at the DC microgrid. Only when the initial power exchange by the BESS is roughly zero, the BESS can be tested on its performance during charging and discharging evenly. Furthermore, the reference value for the ILC is only an estimation since computing an exact balance is relatively complex due to the different losses within the microgrid.

The scenarios to simulate the BESS are described in Table 6.2, where the input by the current source is defined as I_{cs}. With a DC bus voltage around 1000V, the current causes either a surplus or shortage at the DC bus for the BESS to act upon. If the BESS functions as it was designed for, the power input provided by the current source should be fully transferred to the BESS by regulating the DC bus voltage. The actual power exchange with the BESS should, however, be corrected for the estimation error for P^*_{ILC}.

Table 6.2: Different scenarios setups for the BESS.

Scenario	$I_{cs}(t)$	$I_{cs}(t+1)$	**State DC bus**
BESS20kW	0	20	Surplus
BESS-20kW	0	-20	Shortage
BESS10kW	0	10	Surplus
BESS-10kW	0	-10	Shortage
BESS5kW	0	5	Surplus
BESS-5kW	0	-5	Shortage

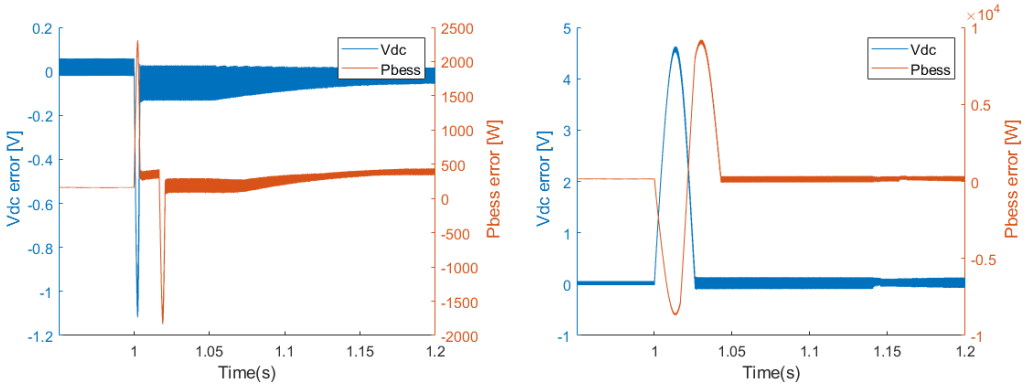

(a) Scenario BESS20kW

(b) Scenario BESS-20kW

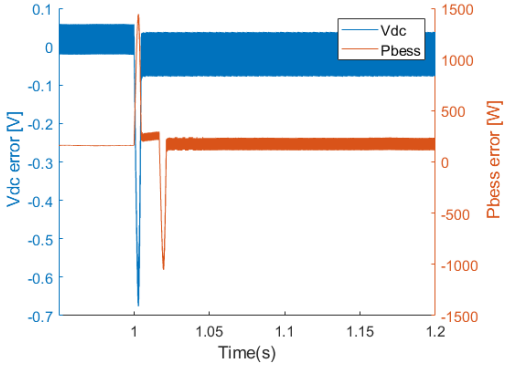

(c) Scenario BESS10kW

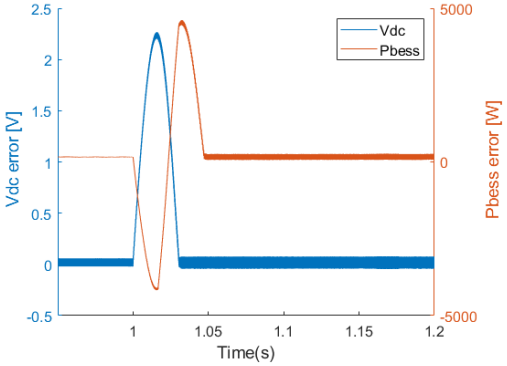

(d) Scenario BESS-10kW

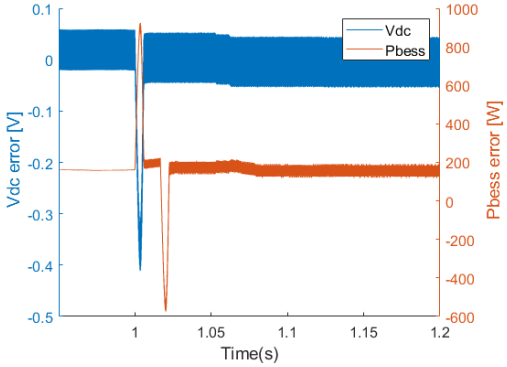

(e) Scenario BESS5kW

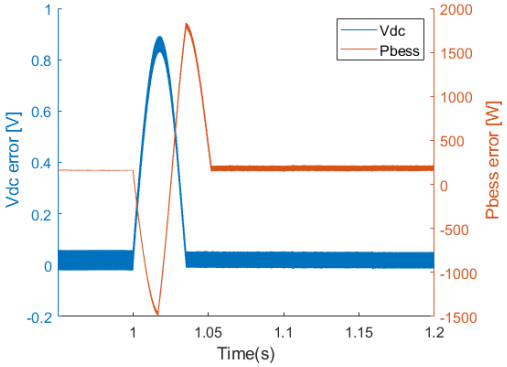

(f) Scenario BESS-5kW

Figure 6.2: The error of V_{DC} and P_{BESS} for different BESS scenarios.

6.1.3.1 Result

In Figure 6.2 the results of the different BESS scenarios are shown. In comparison with the ILC, it is clear that the BESS responds significantly faster. The converter is in particularly fast and accurate in regulating the DC bus voltage, which is considered key in this hybrid microgrid design. Also, the BESS responds relatively faster in case of surplus of power than in case of a shortage. Another noticeable fact is that in every scenario the error of P_{BESS} never reaches zero. This steady state error can be explained as the sum of all power losses in the DC side of the microgrid.

6.1.4 EV

The power flow to the EVs is regulated by controlling the current flow to and from the EVs. Similar to the BESS, the EVs are either in buck mode or boost mode depending on the direction of the desired power flow. For the EVs, the controller should be able to maintain a stable current flow at all times. Table 6.3 defines the different scenarios for the EV, where the reference current is adjusted. In these scenario, the EV is considered to be present in the system and is already charging or discharging. Two scenarios represent a transition moment, where the EV switches from charging to discharging or vice versa.

Table 6.3: Different scenarios setups for the EV.

Scenario	$I^*_{EV}(t)$	$I^*_{EV}(t+1)$	**Mode**
EV50A	5	50	Boost
EV-50A	-5	-50	Buck
EV20A	5	20	Boost
EV-20A	-5	-20	Buck
EV-5A	5	-5	Boost/Buck
EV5A	-5	5	Buck/Boost

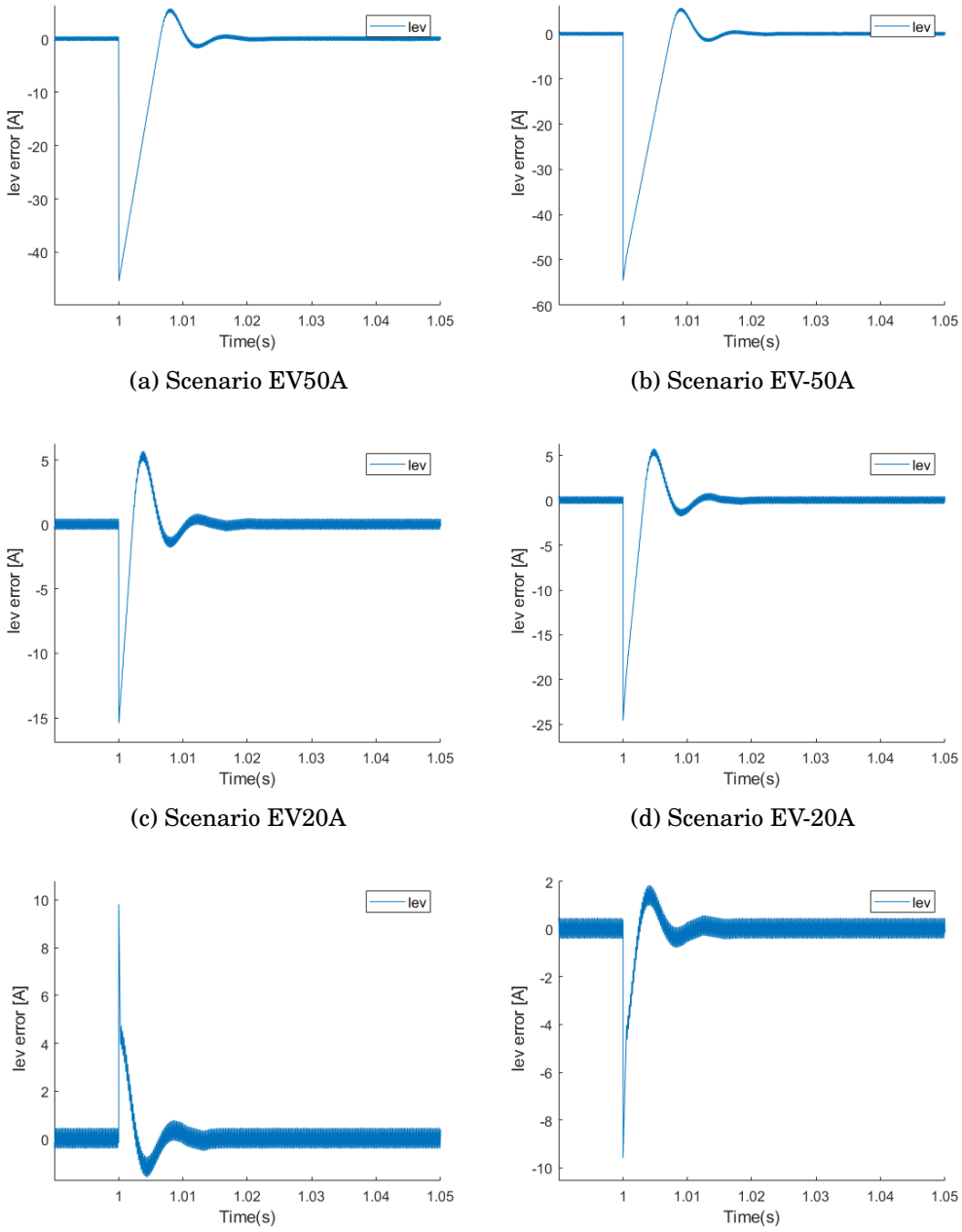

(a) Scenario EV50A

(b) Scenario EV-50A

(c) Scenario EV20A

(d) Scenario EV-20A

(e) Scenario EV-5A

(f) Scenario EV5A

Figure 6.3: The error of I_{EV} for different EV scenarios.

6.1.4.1 Results

The results of the simulation of the EV are shown in Figure 6.3. The EV converter is capable of converging fast to all reference values. As can be expected, in both modes a higher reference current requires the converter longer to converge. Furthermore, as only the errors of the current to the EV ($I^*_{EV} - I_{EV}(t)$) are shown, the different scenarios and their corresponding inverse, except for the last two, look similar. This is due to the fact that the simulation considers a negative current flow when the EV is charged in buck mode, and a positive current flow when the EV is discharged and in boost mode. While the controller

adjusts the sign of the current corresponding to the active mode of operation, these figures reflect the representation used in the Simulink model.

6.1.5 Solar array

To interface the PV array, a boost converter designed by [96] is used. This converter was not designed to be used in this setup and is therefore not expected to perform optimally. It is, however, expected that it functions to some reasonable extent.

The boost converter is enforcing the PV array to operate at the MPP. This means that for different radiation levels the converter must track this optimum accordingly. To test the working of this converter, the solar array is simulated with a radiation of $500W/m^2$ from $t = 0$ till $t = 1$, after which the radiation either increases or decreases significantly.

Table 6.4: Different scenarios setups for the solar array

Scenario	$GHI(t)$	$GHI(t+1)$	$V_{MPP}[V]$	$P_{MPP}[W]$
PV1000Wpm2	0	1000	547.0	45794.8
PV750Wpm2	0	750	544.6	34220.4
PV500Wpm2	0	500	539.7	22601.8
PV250Wpm2	0	250	527.0	11037.7

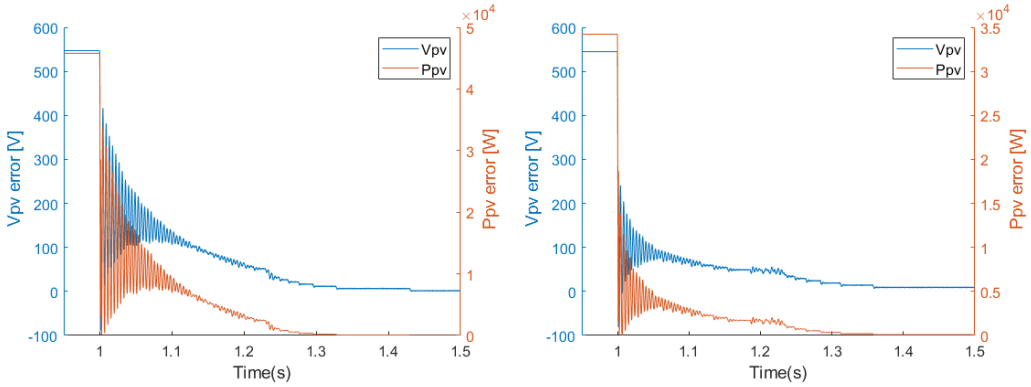

(a) Scenario PV1000Wpm2

(b) Scenario PV750Wpm2

(c) Scenario PV500Wpm2

(d) Scenario PV250Wpm2

Figure 6.4: The error of V_{PV} and P_{PV} compared to the MPP for different EV scenarios.

6.1.5.1 Results

Compared to the other converters in the hybrid microgrid the boost converter of the PV array converges relatively slow to the desired MPP as can be seen in Figure 6.4. The scenarios with the lower irradiance received by the solar array, result also in a relative larger error compared to the two scenarios with the highest irradiance. Although, not all scenarios reflect realistic situations, the converter is able to converge to some extent. In practice, this would result in a lower efficiency by the PV array. Therefore, this boost converter would benefit from some future improvements.

6.1.6 Conclusion

Based on the first sets of scenarios for the lower-level controllers, it can be concluded that the system could operate under the different circumstances that were simulated. Especially, the controllers of the BESS and EV are able to provide a quick response to sudden changes in the system or at a transition moment. The ILC is also able to perform its designed functions, however, in case of bigger changes, the converter requires relatively more time to converge. This accounts also to some extent for the boost converter of the PV array. The boost converter is to able to approach the MPP under different circumstances, nevertheless, its design could still be improved significantly.

In all cases, the converters were subjected to step function to test for their response. In most cases, the scenarios could be considered quite extreme and in some cases not realistic. Nonetheless, for the operation of the hybrid microgrid, the designs of the controllers are suitable. Especially, the BESS can provide the stability within the DC microgrid and the EV controller can coordinate the accurate charging of the EVs. During operation, both are subjected to relatively faster changes. The ILC is mainly depending on changes of its setpoint, which depends on the relatively slower higher-level controller. Therefore, the speed of the ILC is considered suitable.

6.2 Scenario 2: Higher-level controller

The higher-level controller is designed to regulate the overall power balance in the hybrid microgrid and to determine the setpoints for the lower-level controllers. These setpoints are the outcome of an optimization performed by the MPC controller. To test the performance of this controller, it is isolated and, therefore, the Simulink model is not being used for these scenarios. The designed MPC controller will first be modeled with different prediction horizons. Also, the effects of using weights in the objective function are analyzed. Hereafter, it is investigated how the controller behaves with different numbers of EVs. This provides insight into the scalability of the controller design. Last, to test the robustness of the MPC controller, it is modeled under different circumstances where the predicted generation or demand within the microgrid does not correspond to the actual generation or demand.

6.2.1 Simulation setup

For all scenarios, a full day will be modeled in 5 minute time steps. To represent the PV generation and the office load, an arbitrarily working day in May is taken as a reference. The generation and the demand are considered to be known and shown in Figure 6.5. Although, this is not necessarily realistic, it is suitable to test the operation of this controller. Similarly, the SOC upon arrival, the desired SOC, the arrival time and departure time of the EVs, are also assumed to be known. In reality this highly unlikely, however, it simplifies

the testing of several aspects of the MPC controller. In the reference scenarios six EVs are included which are defined in Table 6.5. Furthermore, the weights for the objective function are initially set as w = [1, 0.1, 0.01] and the the prediction horizon is set to be 12. In the different scenarios one or more of the aspects are changed. The basic simulation setup is selected to investigate the microgrid in relatively normal conditions. In the different scenarios, the individual aspects are tested for a wider range of values. By considering this approach, the focus of each scenario is on the actual contribution of the individual aspects.

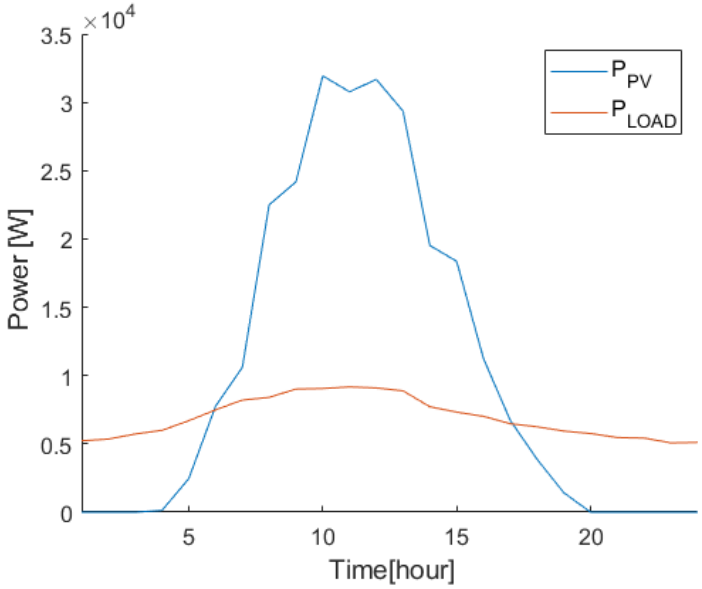

Figure 6.5: 24 hour PV and office load pattern used for Scenario set 2

Table 6.5: Parameters of the EVs in the reference scenario

EV index	Type	SOC_{arr}	SOC_{des}	t_{arr}	t_{dep}
1	Tesla s	50%	90%	09:00:00	17:00:00
2	Nissan Leaf e+	60%	80%	09:15:00	17:00:00
3	BMW i3s	40%	90%	08:30:00	12:30:00
4	Tesla s	70%	90%	08:20:00	16:35:00
5	Nissan Leaf e+	55%	80%	11:05:00	17:35:00
6	BMW i3s	80%	90%	08:55:00	17:40:00

6.2.2 Varying the prediction horizon

To gain insight in the effect of the prediction horizon on the MPC controller, one day is simulated with the different prediction horizons defined in Table 6.6.

Table 6.6: Prediction horizons of different scenarios

Scenario name	N1	N12	N24	Units
Prediction horizon	1	12	24	[-]
Prediction horizon	5	60	120	[min]

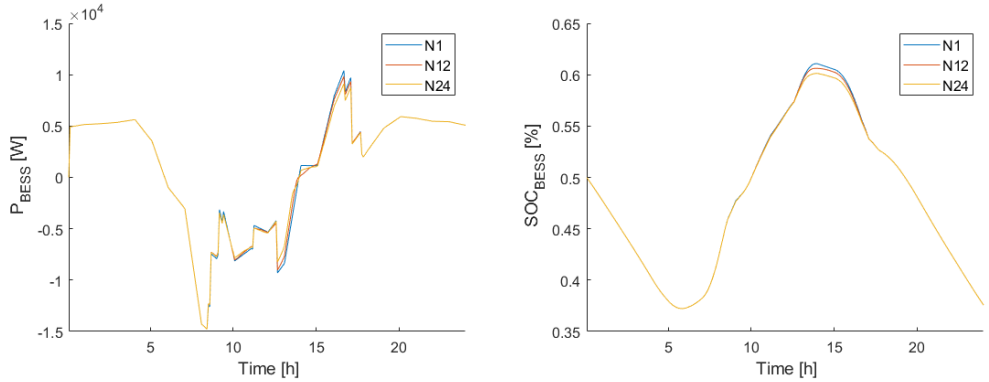

(a) Power exchange with the BESS

(b) SOC of BESS

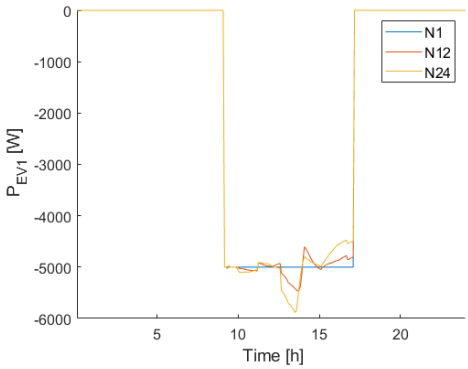

(c) Power exchange with the EV1

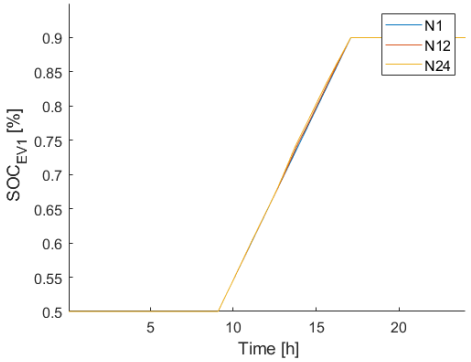

(d) SOC of EV1

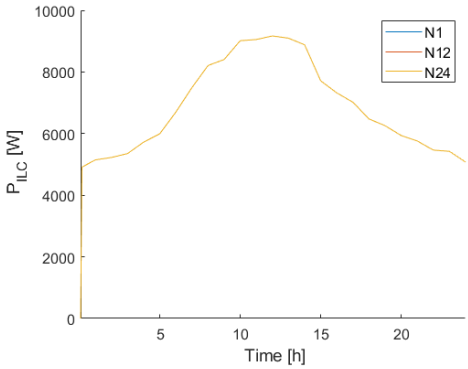

(e) Power exchange over the ILC

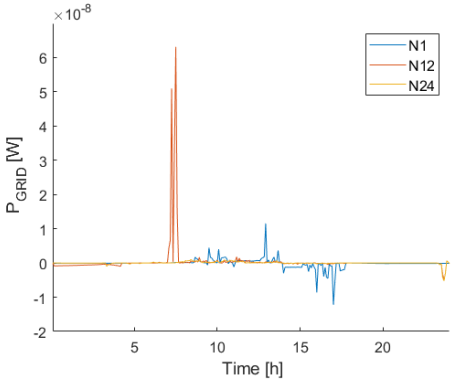

(f) Power exchange with the grid

Figure 6.6: The effect of different prediction horizons on the BESS, EV1, the ILC and the grid connection.

6.2.2.1 Results

By running the simulation for the different prediction horizons, Figure 6.6 is obtained. Of the EVs only EV1 is shown. The rest can be found in the appendix in Figures A.1 and A.2 since these figures are quite similar. Not in all figures, a clear difference can be seen between the different scenarios. First of all, it is clear that the microgrid is not depending on the utility grid. The BESS provides the office load with power when no PV power is generated. Once the PV generation is increasing, it starts to supply the office load as well as the EVs when they have arrived. At some point the total generation is more than the

total demand within the hybrid microgrid, at which the BESS also starts to charge. Once the PV power decreases, the BESS takes over the role of supplying the internal demand.

With respect to the different prediction horizon not many significant differences can be detected based on the figures alone. Only, with a prediction horizon of 1 ($N = 1$), the power flows to the EVs are clearly more constant than in the other two scenarios. In this case the EVs are charged linearly conform the constraint that enforces the charging of the EVs.

Table 6.7: Summary of scenarios with different prediction horizons

Scenario name	**N1**	**N12**	**N24**	**Units**
Calculation time	178.2	373.0	589.4	[s]
To the grid	0.00	0.00	0.00	[kWh]
From the grid	0.00	0.00	0.00	[kWh]
To the BESS	50.09	49.12	48.10	[kWh]
From the BESS	76.21	75.24	74.21	[kWh]
To the EVs	113.22	113.22	113.22	[kWh]
From the EVs	0.00	0.00	0.00	[kWh]

In Table 6.7 as summary is given of the calculation times, the power flows to and from the grid, BESS and all the EVs. It is clear that the longer the prediction horizon the more calculation time is required. Also, it results in more direct power flows since less power is flowing via the BESS. Furthermore, while considering the main objective of the controller, no better results for either one of the scenarios can be seen. This could be explained due to the large internal supply of power in the microgrid.

6.2.3 Varying the weights in cost function

Every iteration, the MPC controller optimizes a cost function to determine the next set-points. This cost function contains three terms. The first term represents the main objective of the controller, to minimize the power exchange with the grid. The next two terms represent the power exchange with the EVs and the BESS respectively. These terms are in place to balance out the power flow to the EVs and the BESS as well as minimize unnecessary and unwanted power flows. Also, by applying different weights, priority can be given to either use the BESS or the EVs to store power.

The different scenarios are shown in Table 6.8, where w(1), w(2), and w(3) correspond, respectively, to the terms of the cost function. The first scenario, in contrast to the other three scenarios, simulates the MPC controller without the second and third term. This means that the charging and discharging of the BESS and the EVs has no consequences for the objective function. In the second scenario, the the power flow to the BESS is prioritized over the power flow to the EV. The third scenario gives priority to the EVs and the final scenario, gives no priority to the BESS or EVs over the other. In these cases, priority defines the power flow that has the least effect on the objective function and is therefore preferred.

Table 6.8: Weights of the cost function for different scenarios

Scenario name	**W1**	**W2**	**W3**	**W4**
w(1)	1	1	1	1
w(2)	0	0.1	0.01	0.1
w(3)	0	0.01	0.1	0.1

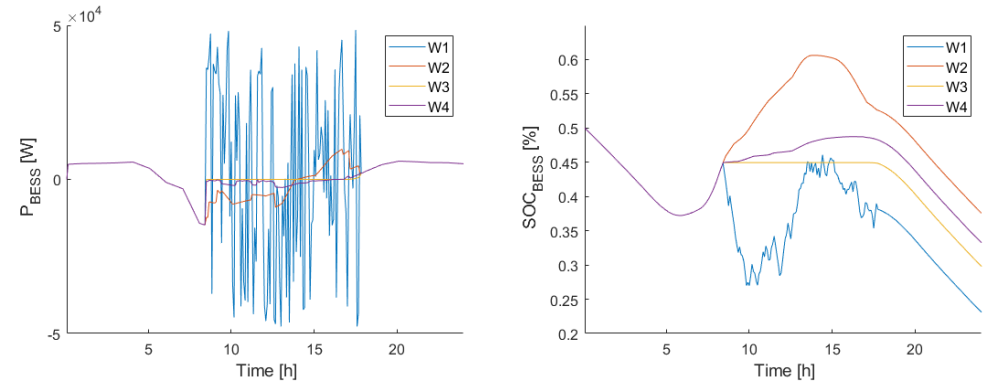

(a) Power exchange with the BESS

(b) SOC of BESS

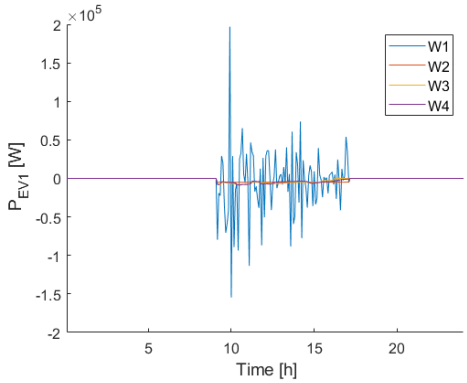

(c) Power exchange with the EV1

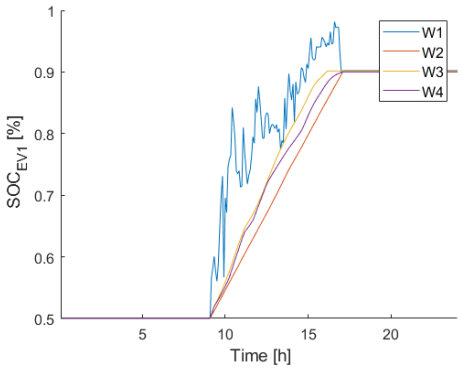

(d) SOC of EV1

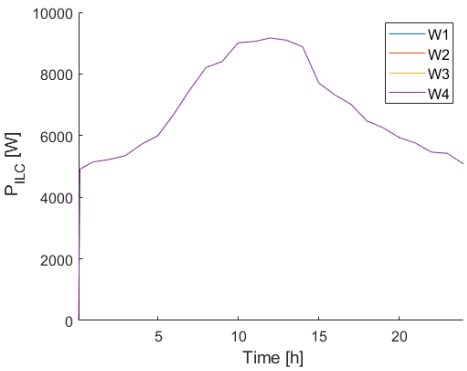

(e) Power exchange over the ILC

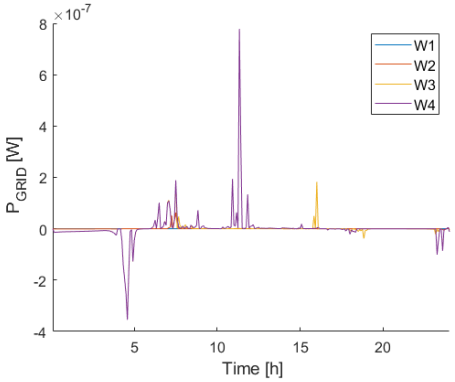

(f) Power exchange with the grid

Figure 6.7: The effect of different weights in the cost function on the BESS, EV1, the ILC and the grid connection.

6.2.3.1 Results

The results for the scenarios with different weights in the cost function are shown in Figure 6.7. Only the power to and from EV1 and its SOC is shown here. The power flows of the other EVs and their SOCs are shown in the appendix in Figures A.3 and A.4. First of all, the most noticeable scenario is $W1$. It results in very irregular power flows to the BESS and EVs. This is the result of not penalizing the power exchange with the BESS and the EVs. Due to this, the optimization only affects the power exchange with the grid allowing the BESS and the EVs, for example, to transfer to one and other for no reason.

All other three scenarios result in a smoother power flow to the BESS and EVs. Furthermore, based on the SOCs of the BESS and EVs, it is clear that scenario $W2$ prioritizes the power flow to the BESS over the flow to the EVs. Also, it can be seen that as result of prioritizing the power flow to the EVs in $W3$ and $W4$, more EVs depart with a higher SOC than desired.

Table 6.9: Summary of scenarios with different weights in the cost function

Scenario name	**W1**	**W2**	**W3**	**W4**	**Units**
Calculation time	471.7	380.8	369.0	371.1	[s]
To the grid	0.00	0.00	0.00	0.00	[kWh]
From the grid	0.00	0.00	0.00	0.00	[kWh]
To the BESS	130.51	49.12	16.23	24.17	[kWh]
From the BESS	186.98	75.24	58.64	59.37	[kWh]
To the EVs	540.52	113.22	130.03	122.38	[kWh]
From the EVs	396.95	0.00	0.52	0.08	[kWh]

Table 6.9, and also Figure 6.7, illustrate that the different weights do not affect the ability of the microgrid to support its own power demand for this specific simulation. Furthermore, the table also confirms the inefficient power flows for scenario $W1$. Large amounts of power that were stored in the BESS and in the EVs were also withdrawn, while the other scenarios kept this to a minimum. Moreover, it can be seen that $W2$ indeed uses primarily the BESS to store power while $W3$ the EVs. Scenario $W4$ shows as expected no preference for the storage system. As a result, in these two scenarios and also in $W1$, some EVs also leave with a higher SOC then desired (Figure A.4). Although this is not necessarily a bad thing, it is preferred to keep as much power as possible within the microgrid. This means that power is preferably stored in the BESS. Only if the BESS is fully charged, extra power should be stored in the EVs, possibly resulting in a higher SOC than desired. To this respect, scenario $W2$ shows the preferred behavior.

6.2.4 Different number of EVs

The higher-level controller has thus far been modeled with six EVs present in the system. To test the robustness with respect to the number of EVs, the controller is modeled with different numbers of EVs present in the system. Table 6.10 defines the number of EVs for the different scenarios. Scenario EV19 is based on the reference system. Based on the size of the reference system, a minimum of 19 parking lots should be present. The last scenario is proposed to see whether the controller design would still function when the number of EVs is scaled up.

The different EVs with their corresponding SOC upon arrival, time of arrival, desired SOC upon departure, and time of departure are shown in Table A.2 in the appendix. The first 6 EVs, are equal to the EVs proposed in Table 6.5. The other 34 EVs are randomly composed. The SOCs upon arrival lie for these EV between 20% and 70%, and the desired SOCs lie between 10% and 50% higher, with maximum SOC of 100%. Furthermore, all EVs arrive between 07:00 and 12:00 in the morning and depart between 15:00 and 20:00.

Table 6.10: The number of EVs for different scenarios

Scenario name	**EV1**	**EV6**	**EV19**	**EV40**
Number of EVs	1	6	19	40

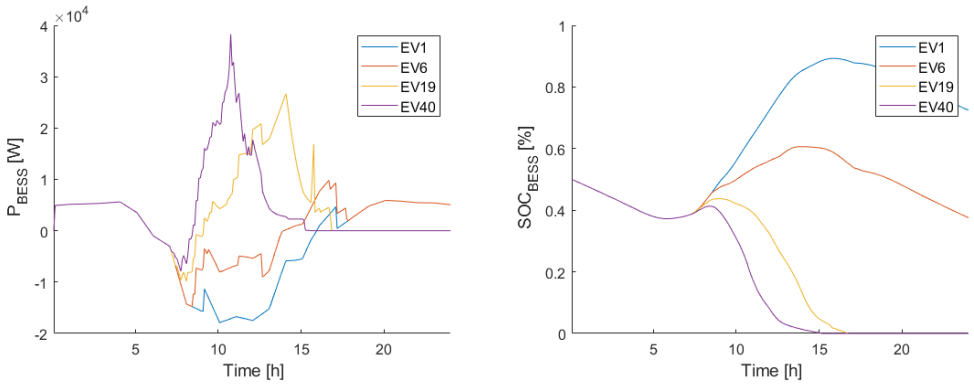

(a) Power exchange with the BESS

(b) SOC of BESS

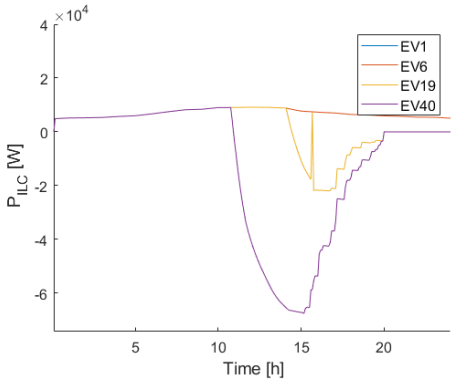

(c) Power exchange over the ILC

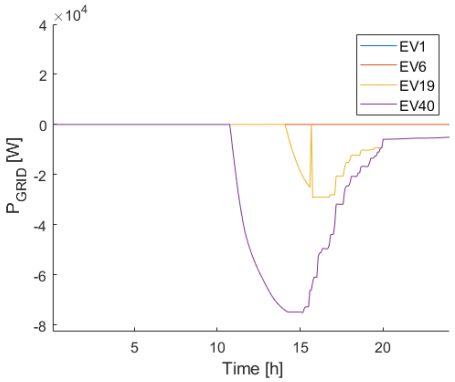

(d) Power exchange with the grid

Figure 6.8: The effect of different numbers of EVs on the BESS, the ILC and the grid connection.

6.2.4.1 Results

The effect of different numbers of EVs on the BESS, ILC and the grid is clearly visible in Figure 6.8. Overall, the more EVs present in the system the higher the total power they demand. For the scenarios E19 and E40 it is clear that the load of the EVs fully discharge the BESS and as consequence the grid needs to support the microgrid. This is also confirmed by Table 6.11. Due to the large load by the EVs, it is clear that the BESS is also utilized less to store power temporarily. Nonetheless, the higher-level controller is able to control the microgrid for different numbers of EVs. Only, the calculation time increases with an increasing number of EVs.

Table 6.11: Summary of scenarios with different numbers of EVs

Scenario name	**EV1**	**EV6**	**EV19**	**EV40**	**Units**
Calculation time	211.9	409.8	848.1	1591.4	[s]
To the grid	0.00	0.00	0.00	0.00	[kWh]
From the grid	0.00	0.00	123.68	442.62	[kWh]
To the BESS	109.28	49.12	13.79	8.57	[kWh]
From the BESS	62.18	75.24	118.79	113.57	[kWh]
To the EVs	40.00	113.22	315.88	634.72	[kWh]
From the EVs	0.00	0.00	0.10	0.00	[kWh]

6.2.5 Unpredicted circumstances

All previous scenarios have been modeled while assuming the PV generation, the officie load at the AC side of the microgrid, and the details of the EVs to be known. In practice, this is generally not the case. Even with modern prediction models for the received irradiance [118] and with load shifting possibilities to shape the load the some extent [119], errors or unexpected situations can occur. Similar, EVs can arrive and depart earlier or later as well as the SOC upon arrival and the SOC desired can be different than expected. This is, however, considered outside the scope of this research.

To investigate the effect of differences between the predicted values and the actual values, two scenarios are simulated. First of all, a scenario is modeled in which the solar PV generation is half of the expected value for the period of half an hour in the middle of the day. Based on the design of the lower-level controllers, the BESS reacts in case of a shortage or surplus on the DC side of the microgrid.

For the second scenario, a day is modeled where the real office load is 30% higher than predicted over a period of 2 hours. In this type of situation the extra power is coming from the grid. Both scenarios are modeled with a prediction horizon of 1 and 12, resulting in the scenarios shown in Table 6.12. Corresponding to the described scenarios, the PV generation and office load curve are shown in Figure 6.9.

Table 6.12: Scenarios with unpredicted PV generation and office load. For each scenario it is described what prediction horizon is considered and whether the PV generation or the office load is predicted (✓) or not (×).

Scenario name	**PV.N1**	**PV.N12**	**L.N1**	**L.N12**
Prediction horizon	1	12	1	12
Accurate P_{PV} prediction	×	×	✓	✓
Accurate P_{LOAD} prediction	✓	✓	×	×

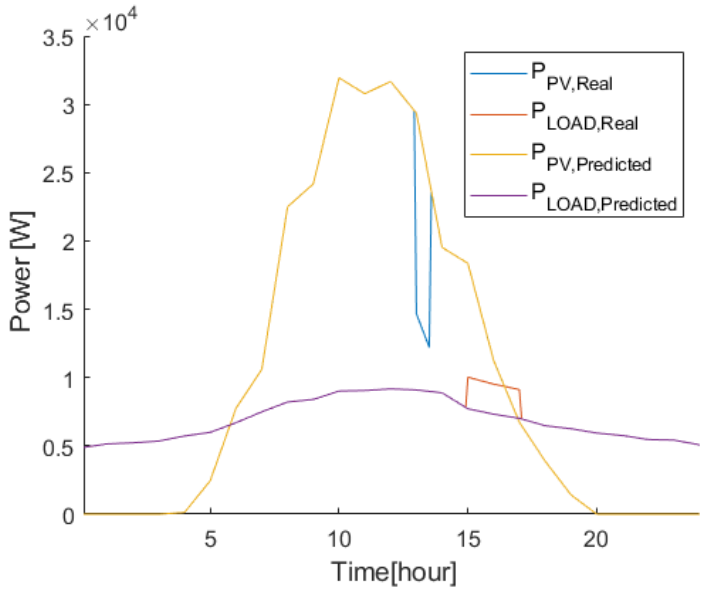

Figure 6.9: Predicted en actual PV generation and office load pattern

6.2.5.1 Results

In Figure 6.10 the effect of the unpredicted PV generation and load are shown. All left figures display the effect on the BESS, the ILC and the interaction with the grid. All figures on the right show the results in case the higher-level controller predicted the real PV generation and demand pattern, as shown in Figure 6.9, correctly.

As one would expect, the figures illustrate that the BESS is able to respond more accurately when it predicted a sudden decrease in PV generation. This is, however, only the case for PV.N12. When the prediction horizon is 1, no significant effect can be seen based on the figures and Table 6.13. On the contrary, for the scenarios including a sudden increase in demand, the effect is significant. With a prediction horizon of 1, the controller can enforce the microgrid to use power from the BESS and not from the grid. In both scenarios, the positive effect of a longer prediction horizon is confirmed.

In line with the previous, the unpredicted demand clearly affects the power flow to the grid since all required extra power is taken from it as can be seen in the figures and in Table 6.14. When the demand is predicted correctly, actually no support is needed at all. The microgrid is in this case able to transfer power from the BESS via the ILC.

Table 6.13: Summary of scenarios with unpredicted PV generation

	Unpredicted		**Predicted**		
Scenario name	**PV.N1**	**PV.N12**	**PV.N1**	**PV.N12**	**Units**
Calculation time	187.6	408.4	192.6	397.4	[s]
To the grid	0.00	0.00	0.00	0.00	[kWh]
From the grid	0.00	0.00	0.00	0.00	[kWh]
To the BESS	46.60	46.14	46.60	45.42	[kWh]
From the BESS	80.56	80.10	80.56	79.38	[kWh]
To the EVs	113.22	113.22	113.22	113.22	[kWh]
From the EVs	0.00	0.00	0.00	0.00	[kWh]

Table 6.14: Summary of scenarios with unpredicted demand

	Unpredicted		**Predicted**		
Scenario name	**L.N1**	**L.N12**	**L.N1**	**L.N12**	**Units**
Calculation time	190.0	411.1	189.52	421.6	[s]
To the grid	0.00	0.00	0.00	0.00	[kWh]
From the grid	4.60	4.60	0.00	0.00	[kWh]
To the BESS	50.09	49.12	50.09	49.12	[kWh]
From the BESS	76.21	75.24	80.80	79.83	[kWh]
To the EVs	113.22	113.22	113.22	113.22	[kWh]
From the EVs	0.00	0.00	0.00	0.00	[kWh]

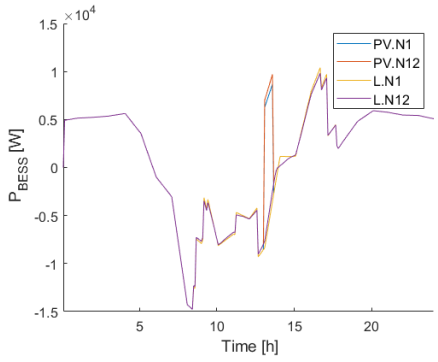

(a) Power exchange with the BESS [U]

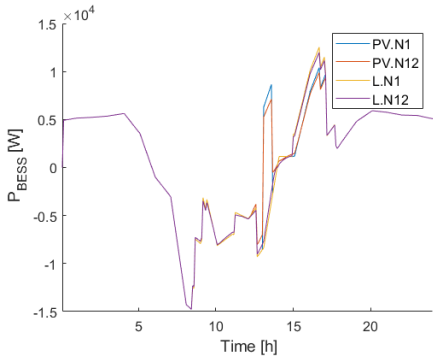

(b) Power exchange with the BESS [P]

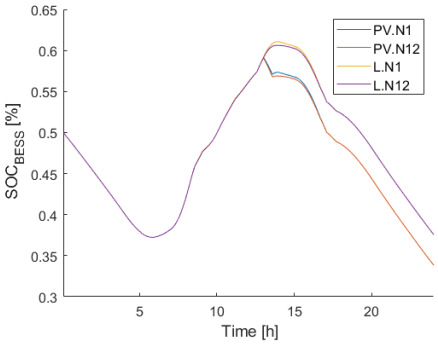

(c) SOC of the BESS [U]

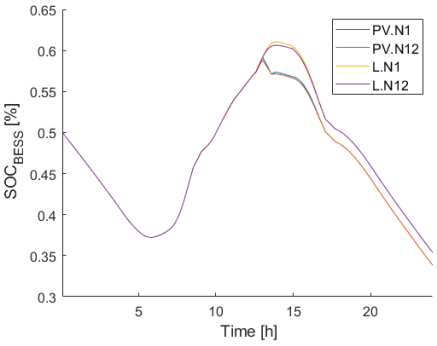

(d) SOC of the BESS [P]

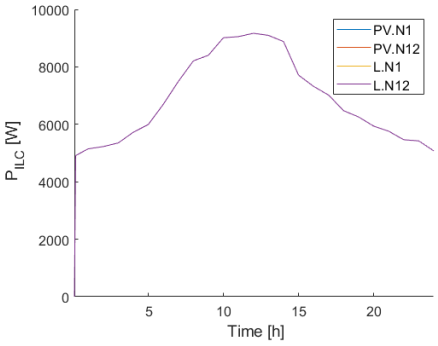

(e) Power exchange over the ILC [U]

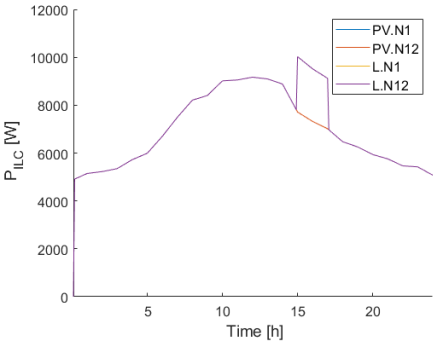

(f) Power exchange over the ILC [P]

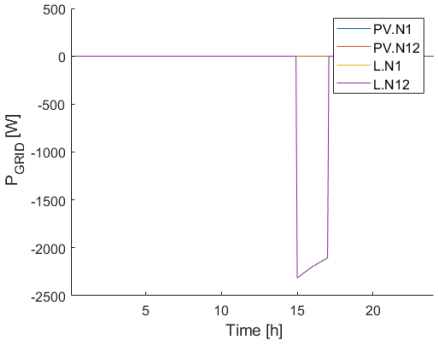

(g) Power exchange with the grid [U]

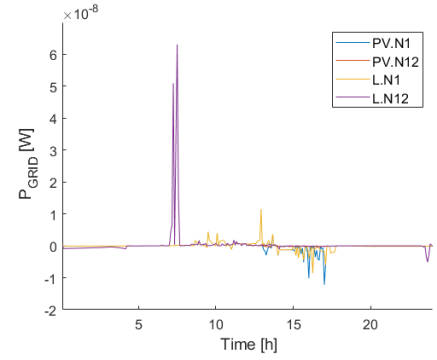

(h) Power exchange with the grid [P]

Figure 6.10: The effect of unexpected circumstances on the BESS, the ILC and the grid connection is shown on the left side and marked by [U]. All figures on the right, marked by [P], display the effect of the higher-level controller, in case it predicted the new real PV generation and demand pattern.

6.2.6 Conclusion

The higher-level controller was tested on several aspects in an isolated environment. This means that the lower-level control was not included during simulations. First of all, the scenarios were tested with different prediction horizons. It was shown that a longer prediction horizon showed better results in regulating the power flows more efficient. The calculation time, however, increased significantly with an higher prediction horizon.

The effects of different weights in the cost function was tested next. While the main objective of the higher-level controller is to minimize the power exchange with the grid, the effect of penalizing the power exchange with the BESS and EVs showed interesting results. By assigning different penalties, the controller is able to determine whether the BESS or the EVs are used as the primary storage system. Depending of the required way of operation, the weights can be tuned as preferred.

The third aspect that was tested, was the scalability of the designed controller with respect to the number of EVs. Without an issue the controller is able to handle different numbers of EVs. It is, however, worth to mention that the relative impact of the microgrid reduces if the number of EVs becomes disproportionately large compared to the rest of the microgrid.

Last, the higher-level controller was investigated in dealing with unpredicted PV generation or demand. Based on the scenarios, it can be concluded that more accurate predictions lead to better performance of the controller. It must be mentioned that the controller is still able to control the microgrid in case of unpredicted circumstances. Furthermore, improvements could be made to the controller if the predicted PV generation or demand would be less accurate than it is considered in this research. This is however outside the scope of this research.

6.3 Scenario 3: Interaction lower and higher control layer

In the previous two sets of scenarios the lower-level controller and the higher-level controller have been investigated as two separate control layers. For the actual microgrid a combination of both is required to operate as it is designed for. This section will therefore simulate the working of the hybrid microgrid by combining the Simulink model with the MPC controller in Matlab. First of all, it is explained how this simulation is performed after which the setup of the simulation will be described. Finally, the results of the simulation will be discussed.

6.3.1 Modeling

Due to the large computation time of the Simulink model, and to some extent of the MPC controller, it is not feasible in terms of time and memory of Simulink to run simulations that have long time frame. The operation of the microgrid and the interaction of the two control layers is, however, especially interesting over a relative longer time period. Therefore, an customized simulation is performed that only includes the transition moments.

For this simulation a half-hour period will be simulated, where the higher-level controller has a sample time of 5 minutes. Every 5 minutes it calculates new setpoints for the lower-level controllers based on the latest state of the hybrid microgrid. The Simulink model will only be modeled for 1 second after it receives the new setpoints. This gives the lower-level controllers enough time to converge to their new setpoints and reach steady-state. The steady-state values are then used to manually calculate the new states of the

microgrid over the next 4 minutes and 59 seconds, after which the cycle repeats itself. Effectively, only 6 seconds have to be simulated in Simulink this way.

6.3.2 Simulation setup

For the simulation, a half-hour period is modeled, starting at 11:00 till 11:30. The PV generation and the demand pattern used in section 6.2 and shown in Figure 6.5 in the appendix, are again considered for this simulation. However, they are only used for the defined time window. Also, the higher-level controller is able to predict the PV generation and load. To represent the EVs, three EVs are simulated. The details are shown in Table 6.15 and defined such that in the specific time window one EV arrives, one departs and one is present throughout the simulation.

The higher-level controller is setup with a prediction horizon of 12, and weights w = [1, 0.1, 0.01]. Furthermore, although the simulation entails only a half-hour period, the prediction horizon will include predictions beyond this time window.

To determine the beginning states of the different components and the setpoints at $t_0 = 11:00$, the simulation of the higher-level controller is used. These setpoint are shown in Table A.3 in the appendix.

Table 6.15: Parameters of the EVs in the scenario of the two-level control strategy

EV index	Type	SOC_{arr}	SOC_{des}	t_{arr}	t_{dep}
1	Tesla s	50%	90%	08:00:00	16:00:00
2	Nissan Leaf e+	60%	80%	09:15:00	11:25:00
3	BMW i3s	40%	90%	11:10:00	18:30:00

6.3.3 Results

The results of the simulation of the two-level control strategy for the BESS, ILC, grid, load and PV array are shown in Figure 6.11. It must be mentioned that all MPC graphs have data points every 5 minutes, while the Simulink graphs one every one hundredth of a second. Consequently, together with the fact that the setpoints only change once every 5 minutes, the Simulink simulation results in the stepped lines.

First of all, similar to the results in the first set of scenarios, the power exchange with the BESS does not match the setpoints, which are in this case provided for by the MPC controller. All losses experienced in the DC microgrid sum up and result in this error between the actual power exchange with the BESS and its setpoints. This is caused by the indirect nature of the control objective of the BESS as discussed previously. Nevertheless, based on the figure, it can be said that the power exchange with the BESS does follow the trend of the setpoints nicely with a relatively constant error. Furthermore, at 10 minutes a small spike can be detected which is caused by the arrival of EV3.

The power exchange with the BESS directly affects its SOC as can be seen in Figure 6.11b. Compared to the power flows, which remain constant until a next setpoint is set, the SOC changes constantly if the power exchange with the BESS is nonzero. The first second of every 5 minutes of the Simulink SOC is determined by the Simulink simulation. The rest of the 5 minutes is extrapolated based on the steady state power flow. The resulting increase in SOC was fed back to the Simulink simulation for the next cycle. As can be seen, this estimation of the Simulink simulation is quite accurate as it follows the trend of the MPC setpoints nicely. The difference between the both lines is, however, caused by the error

of the power exchange with the BESS. Because less power is transferred to the BESS than was set for by the MPC controller, the SOC is less than expected.

Next, the power exchange over the ILC is set such it can provide for the load on the AC side based on the values predicted by the MPC controller. As can be seen, the demand of the load is accurately predicted by the MPC. However, it does not result in zero power exchange with the grid as is aimed for by the MPC controller. This is caused, similar to the DC side of the microgrid, by the use of a simplified model of the microgrid for the MPC controller. Herein the losses are not included, which means that the losses of the ILC, the grid connection and all other losses at the AC microgrid are not taken into consideration. As result, these are compensated for by the grid.

The predicted PV generation is in contrast to the predicted load not as accurate. This was expected based on the not optimal functioning model for the converter of the PV array. The PV array is not constantly operating at the exact MPP resulting in this offset compared to the predicted value. This error results in a loss at the DC microgrid, which means that the BESS is compensating for it.

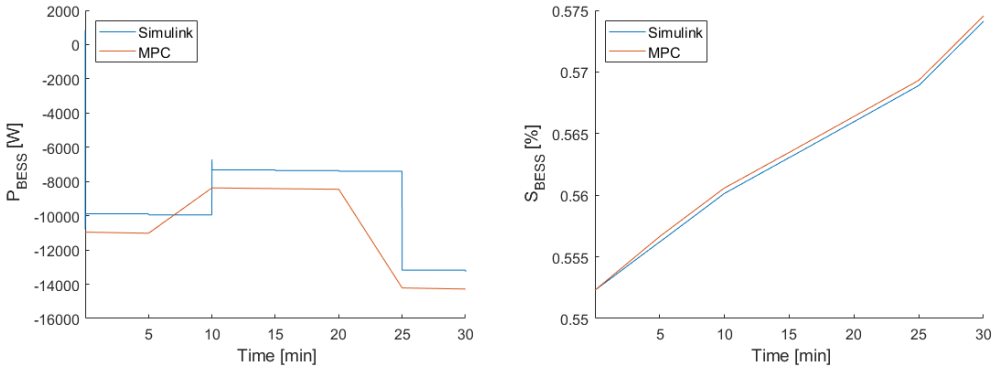

(a) Power exchange with the BESS

(b) SOC of BESS

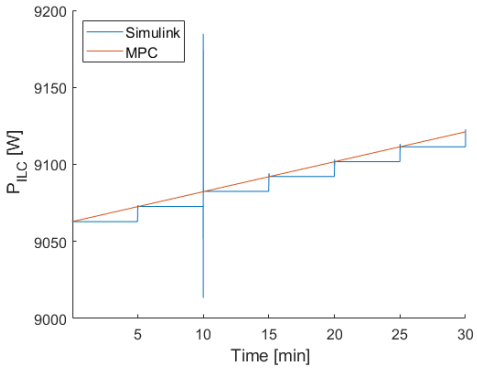

(c) Power exchange over the ILC

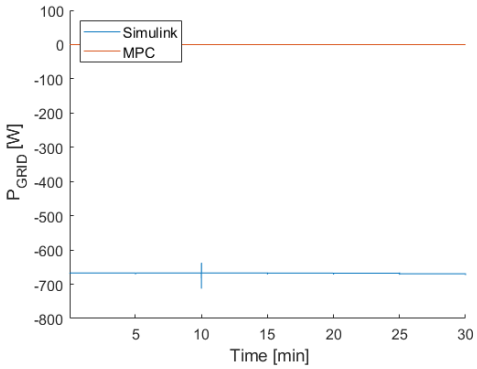

(d) Power exchange with the grid

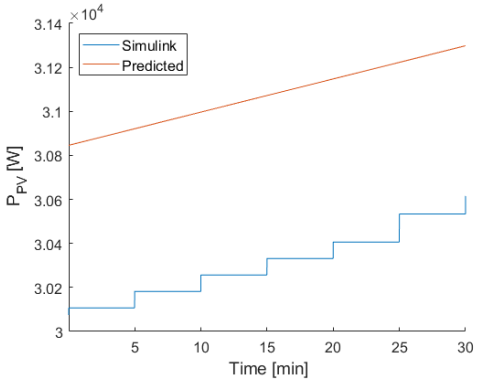

(e) Power generation by the PV array

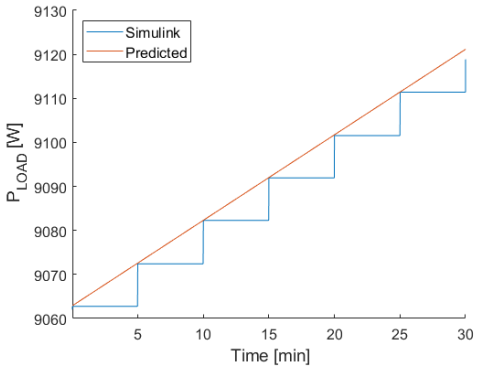

(f) Power demand by the load

Figure 6.11: The results of the two-level control strategy on different components of the microgrid.

Additionally, the resulting power flow to and from the three EVs and the SOCs are shown in Figure 6.12. Corresponding to the scenario description, it is clear the EV2 departs after 25 minutes and EV3 arrives after 10 minutes. Also, the figures of the power flows to the EVs show that the converters of the EVs converge nicely to the setpoints determined by the MPC controller in terms of power. Every cycle, the MPC controller changes the initial setpoint for the EVs only slightly. As a result of the accuracy of the controllers of the EVs in controlling the current flow to the EVS, the Simulink SOCs follows the SOCs determined by the MPC controller almost exact. Furthermore, the linear charging behavior is explained

by the linear constraint that is used by MPC controller to enforce the charging of the EVs. Also, due to used weights in the objective function, the BESS is in this simulation used to store the excess of power. Only when the BESS would be fully charged or reaching its maximum charging capacity, it is expected that the EVs would not be charged linearly.

Finally, it must be mentioned that modeling the microgrid by using extrapolation has consequences for some details, especially in the case of determining the SOCs of the BESS and the EVs. Most importantly, the normal voltage increase at the battery as a result of an increase in SOC was not considered fully in this simulation. In general the voltage of a battery changes depending on the SOC, as was shown in Figure 4.7. By extrapolating the power exchange with the battery, only the power flow was included and therefore not the dynamic characteristics of the battery. In the case of the EVs, where the controller maintains a constant current flow, this would normally have led to an increase of the power. It is, however, assumed that this would have had only a relative small effect since the voltages corresponding to the SOCs considered here do not differ significantly.

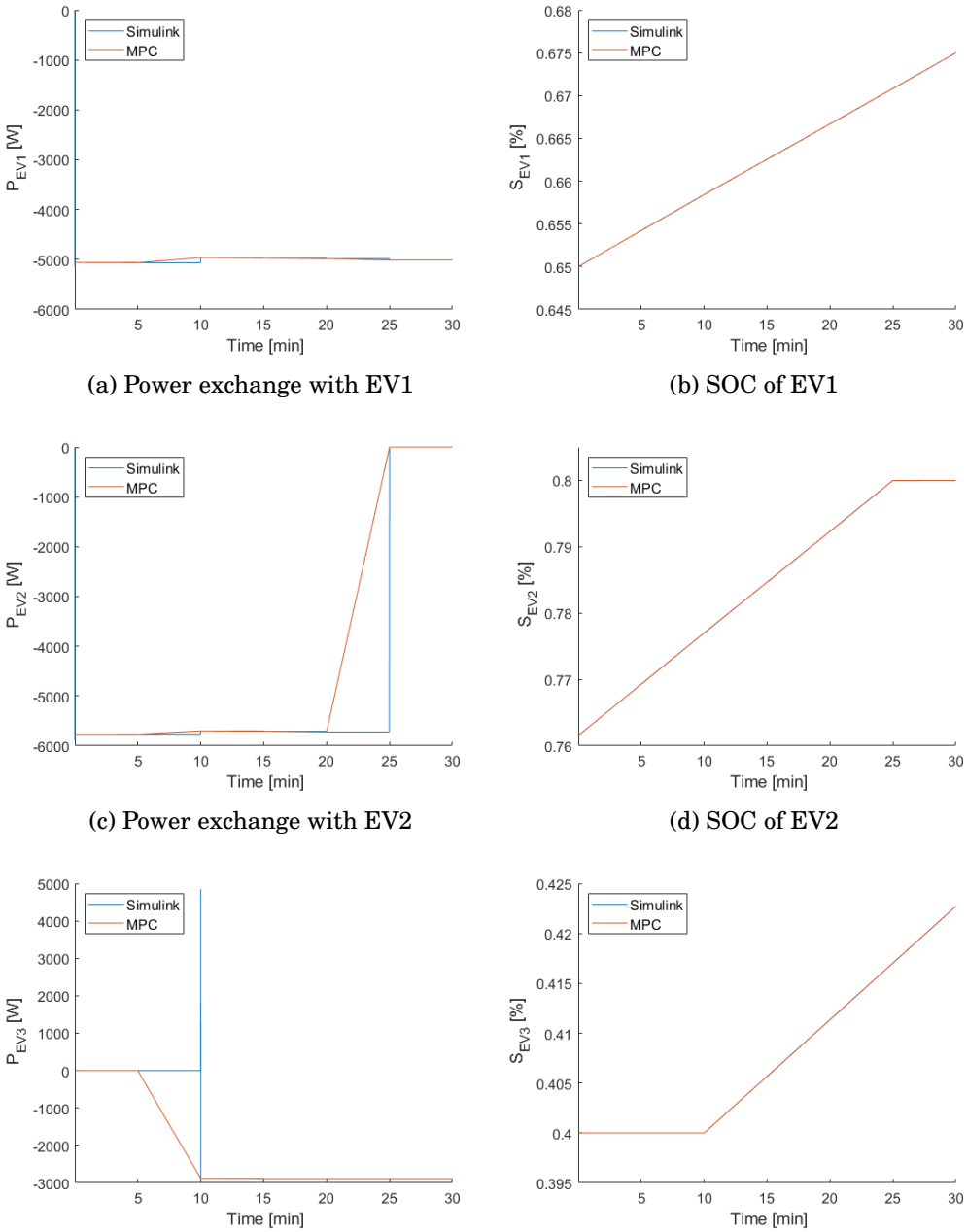

(a) Power exchange with EV1

(b) SOC of EV1

(c) Power exchange with EV2

(d) SOC of EV2

(e) Power exchange with EV3

(f) SOC of EV3

Figure 6.12: The SOC of the EVs for the different prediction horizons

6.4 Scenario 4: Impact of designed hybrid microgrid

In the previous three sets of scenarios the hybrid microgrid design is tested extensively. The lower-level controllers, the higher-level controller and the combination of both has proven itself to be operational. In this set of scenario, it is explored how the design actually impacts the internal demand and supply, and the power exchange with the grid. Also, a comparison is made to the situation where no hybrid microgrid or solar carport would be used.

6.4.1 Simulation setup

To model this set of scenarios only the higher-level controller is used. Based on the previous scenarios, the simulation of this controller is able to accurately simulate the behavior of the hybrid microgrid. The simulation is executed for four time periods of a week in respectively Spring, Summer, Autumn and Winter. In every case, the first week of the season is taken. The actual details of these weeks are not of interest since the four selected weeks are merely to illustrate the diverse operating conditions and the resulting behavior of the microgrid. The corresponding PV and load pattern are shown in the appendix in Figures A.5 and A.6. Furthermore, similar to the scenarios previously described this simulation uses a sample time of 5 minutes, a prediction horizon of 12 and w = [1, 0.1, 0.01] for the weights.

For the setup of the EVs in this scenario, a similar setup is used as in scenario 2 (Table 6.5). However, in contrast to scenario 2 this simulation consists of 7 days of which 5 working days and 2 weekend days. The EVs are only considered to be present during the week days. Consequently, during the weekend no EVs are present and is only the office demanding power according to the pattern in Figure A.6. In case of working days, the characteristics of the EVs are considered to be the same every day. This assumption is made to simplify the simulation setup. Also, more different characteristics are not required to illustrate the working of the the hybrid microgrid design.

6.4.2 Scenario description

Once the hybrid microgrid is simulated for four periods of a week in the different seasons, it is relevant to compare it to different system setups. In all comparisons, the AC load, the PV generation, and demand of the EVs is considered to be the same, unless stated otherwise. An overview of the different scenarios is shown in Table 6.16 and will be discussed next.

A first scenario (**CONV**) to which the hybrid microgrid is compared to is a conventional situation, where no solar carport is present. In this situation, all power to the EVs and to the load is provided for via the grid according the configuration shown in Figure 6.13a. The EVs are in this case connected to the power network of the local load. A second scenario (**SA**), includes an independent solar PV array, which directly provides its power to the grid (Figure 6.13b). This means that it has a separate connection with the utility grid. Scenario three (**SC**) contains also a independent PV array, however, here it is part of a solar carport which allows solar power to flow to the EVs. No battery is present in this case, which means that a surplus of PV power is directly supplied to the grid. Also, when the EVs are in need of power and the solar array cannot supply, it is supplied by the grid according to Figure 6.13c. The fourth scenario is again similar to the previous scenario (**SCL**), only here is the solar carport directly connected to the load (Figure 6.13d). All PV power that is not used by the EVs can be used by the load directly, before it is supplied to the grid. In all scenarios the BESS is absent, resulting in not having any flexibility. This means that all power that is generated within a time instant, needs to be consumed within that same time instant. Hence, the grid acts as an infinite buffer, that can supply in case there is a shortage or receive in case of a surplus. Furthermore, since no overarching control system is considered present in any of the scenarios, the EVs are linearly charged during the day. Once, they arrive they are charged to the desired SOC with a constant power flow. Consequently, the principle of V2G is not considered here.

Table 6.16: Scenario description for comparison

Scenario	Load	PV	EV	BESS	Configuration
HMG	✓	✓	✓	✓	Hybrid microgrid
CONV	✓		✓		Figure 6.13a
SA	✓	✓	✓		Figure 6.13b
SC	✓	✓	✓		Figure 6.13c
SCL	✓	✓	✓		Figure 6.13d

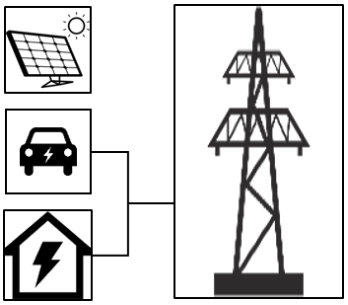

(a) Scenario CONV

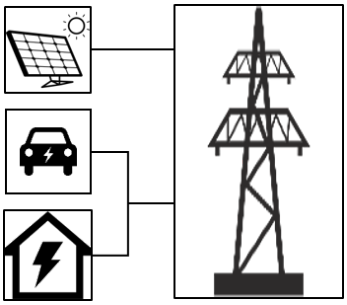

(b) Scenario SA

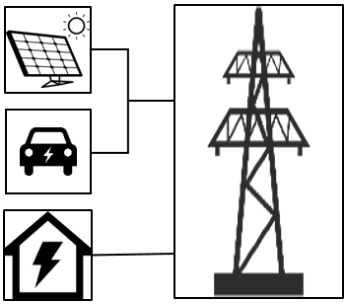

(c) Scenario SC

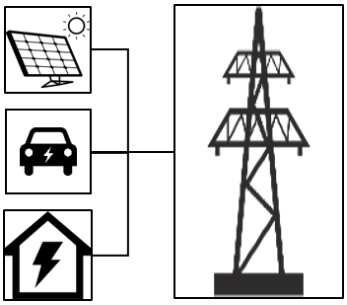

(d) Scenario SCL

Figure 6.13: The configurations of the compared scenarios. The scenarios differ by the connection of the PV array, EVs and load to the utility grid.

6.4.3 Results

In order to make a good comparison, the behavior of the hybrid microgrid during the four seasons is discussed first. It considered as scenario **HMG**. Afterwards, the results of the other scenarios are discussed, followed by a concluding comparison between all scenarios.

6.4.3.1 Hybrid microgrid

The resulting behavior of the hybrid microgrid during a week in four different seasons is shown Figure 6.14. It reflects the behavior of the BESS, EV5, the ILC and the grid connection. Only EV5 is shown to illustrate the behavior of the EVs as well as to illustrate that the EVs are used to store excess power. The figures on the behavior of all EVs can be found in Figure A.7 and A.8 in the appendix.

A first thing that can be noticed is that the BESS is clearly the primary storage system to compensate surpluses and shortages of power within the microgrid. EV5, and the other

EVs are for most part only charged according the desired charging behavior. Only, during the Summer week when the BESS was fully charged, EV5 and EV6 receive more power than desired. Furthermore, only during the Summer and Autumn week the BESS contributed significantly after the initial SOC of the BESS was used. In case of Winter and Spring, the contribution of the BESS was only small due to the low PV generation. Also, the BESS is only used to its full capacity when the PV generation is to its near maximum. When considering all of the above it can be argued that the storage capacity of the BESS can be reduced or the PV array can be enlarged to utilize the used storage system more effectively.

Based on the figure of the ILC it can be seen that especially during the Winter week, power was supplied to the DC side of the microgrid. In case of the Summer week it is clear that most power demanded by the AC load was supplied via the ILC. Also, when no EVs were present during the weekend, and the BESS was fully charged power was supplied to the grid. During all other weeks power was only taken from the grid, to supply the AC load and the EVs.

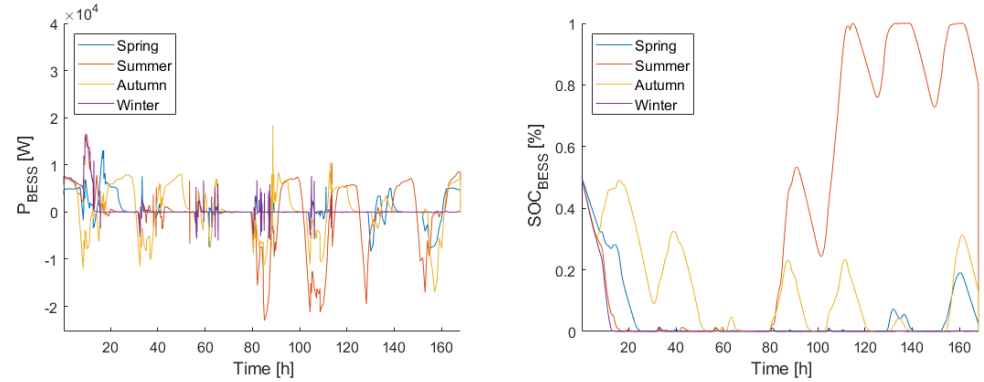

(a) Power exchange with the BESS

(b) SOC of BESS

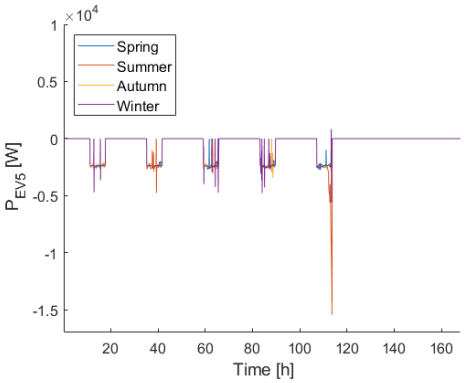

(c) Power exchange with the EV5

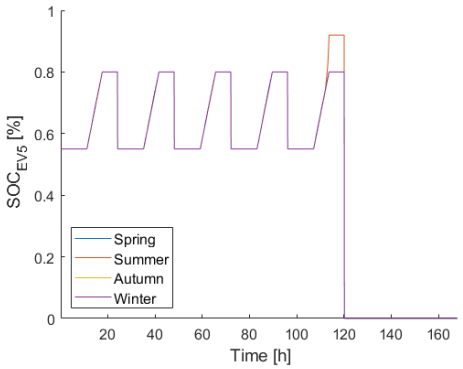

(d) SOC of EV5

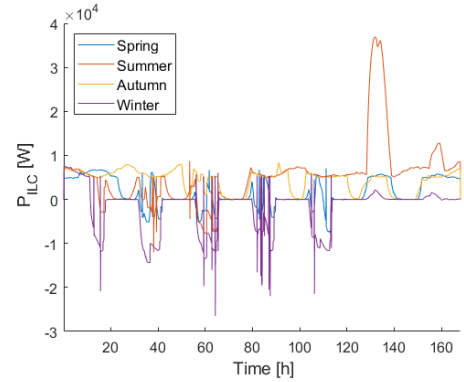

(e) Power exchange over the ILC

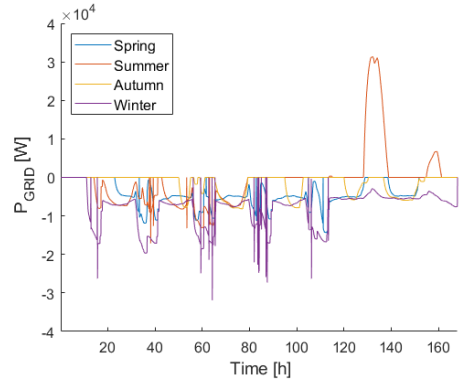

(f) Power exchange with the grid

Figure 6.14: The behaviour of the BESS, EV5, the ILC, and the grid connection during a week in the four different seasons.

The findings based on the figures are confirmed by the summary in Table 6.17. The different seasons have a clear effect on the PV generation and consequently on the power exchange with the grid. During the Winter week the microgrid is significantly more depending on the grid than in the other weeks, even though the total load per week changes only slightly for the different seasons. Furthermore, the table also confirms that the BESS is utilized more during the weeks with more PV generations.

Table 6.17: Summary of the hybrid microgrid during a week in the four seasons

Season	Spring	Summer	Autumn	Winter	Units
Calculation time	2573.2	2546.4	2533.4	2600.5	[s]
From PV array	717.28	1531.53	1219.18	150.36	[kWh]
To the load	936.02	1040.20	1013.17	993.36	[kWh]
To the BESS	75.94	393.47	277.08	16.78	[kWh]
From the BESS	175.37	330.72	354.72	121.78	[kWh]
To the EVs	566.11	577.73	566.10	566.67	[kWh]
From the EVs	0.01	0.02	0.00	0.57	[kWh]
To the grid	0.00	259.08	0.00	0.00	[kWh]
From the grid	680.54	408.21	282.46	1304.10	[kWh]

Finally, although Figure 6.14 provides a good view on the behavior of the hybrid microgrid, it is less useful to make a good comparison. To this purpose, the load duration curve (LDC) is introduced [120]. This curve (Figure 6.15) represents the net power exchange at each time instant with the grid. In the graph these data points are displayed in a descending order. Consequently, the positive area ($P_{GRID} > 0$) under the curve represents the total power transfer to the grid, while the negative area ($P_{GRID} < 0$) represents the power from the grid.

Based on the objective of the higher-level controller, to minimize the power exchange with the grid, a constant line at $P_{GRID} = 0$ is desired. Especially, during the Summer and Autumn week the higher-level controller is able to meet this objective for more than half of all time instants of the week. In case of the Winter week, it is clear that during almost all time steps there is a shortage of power in the microgrid. Finally, in line with Figure 6.14 and Table 6.17, only the Summer week supplies power to the grid.

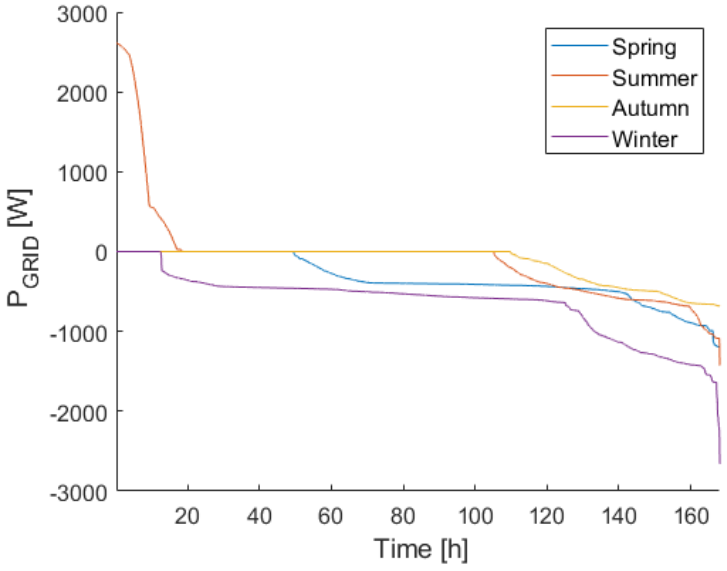

Figure 6.15: LDC for the hybrid microgrid.

6.4.3.2 Scenario CONV

Scenario CONV only considers the EVs and the load to be present, and interconnected to the grid via one connection. As can be expected and is shown in 6.18, is that all required

power comes from the grid. Also, since no power is generated internally, a maximum load is put on the grid. When considering the reference system, an office building, this scenario is for most office facilities the case.

Table 6.18: Summary of scenario **CONV** during a week in the four seasons.

Season	**Spring**	**Summer**	**Autumn**	**Winter**	**Units**
From PV array	0	0	0	0	[kWh]
To the load	936.02	1040.20	1013.17	993.36	[kWh]
To the EVs	566.10	566.10	566.10	566.10	[kWh]
To the grid	0.00	0.00	0.00	0.00	[kWh]
From the grid	1502.12	1606.30	1579.27	1559.46	[kWh]

When the load of the CONV scenario is displayed in an LDC, one obtains Figure 6.16. It is also clear that there is a constant load on the grid since the graphs are constantly far below zero. Furthermore, the graphs for the different weeks, do not differ that much since only the load is different for each week. The resulting load of the EVs is due to the scenario setup the same during each season. As a result, the similar looking stepped increments in each curve represent the combined loads of the EVs at different time instants.

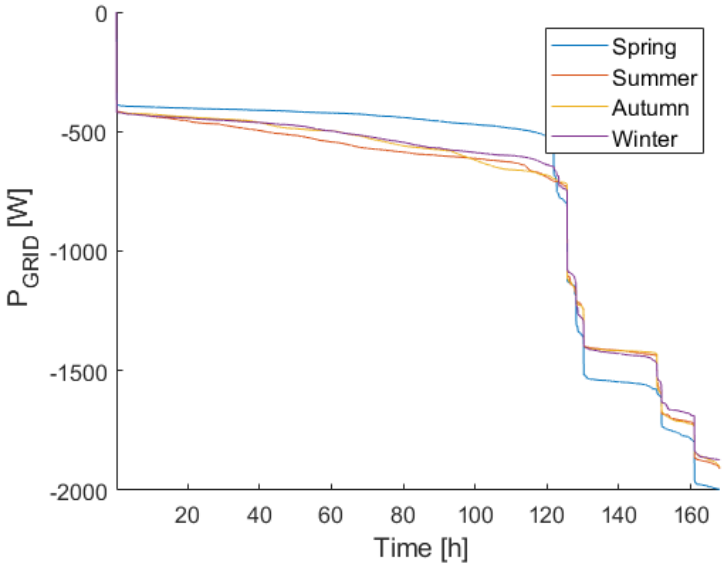

Figure 6.16: Load duration curve for scenario CONV.

6.4.3.3 Scenario SA

Scenario SA shows similar results to the previous discussed scenario. The only difference is that this scenario also includes an independent solar array. In practical terms this could be a solar carport, a rooftop solar array, or an independent solar configuration. Since the solar array is directly to the grid, the PV generation is also transferred directly to the grid (Table 6.19). Due to this configuration, no power will used from the grid via this connection. Other from this extra connection of the PV array, this scenario results in the same load on the grid as scenario CONV.

Table 6.19: Summary of scenario **SA** during a week in the four seasons. Grid1 represents the grid connection of the PV array. Grid2 represents the grid connection of the load and EVs.

Season	**Spring**	**Summer**	**Autumn**	**Winter**	**Units**
From PV array	717.28	1531.53	1219.18	150.36	[kWh]
To the load	936.02	1040.20	1013.17	993.36	[kWh]
To the EVs	566.10	566.10	566.10	566.10	[kWh]
To the grid1	717.28	1531.53	1219.18	150.36	[kWh]
From the grid1	0.00	0.00	0.00	0.00	[kWh]
To the grid2	0.00	0.00	0.00	0.00	[kWh]
From the grid2	1502.12	1606.30	1579.27	1559.46	[kWh]

Figure 6.17 displays the LDC of both individual connections. The LDC of the connection the PV array shows clearly the seasonal differences for the PV generation. These differences are reflected in the maximum power transfer as well as in the total hours PV power is generated. The LDC of the second connection is identical to the LDC of scenario CONV, for the previously stated reasons.

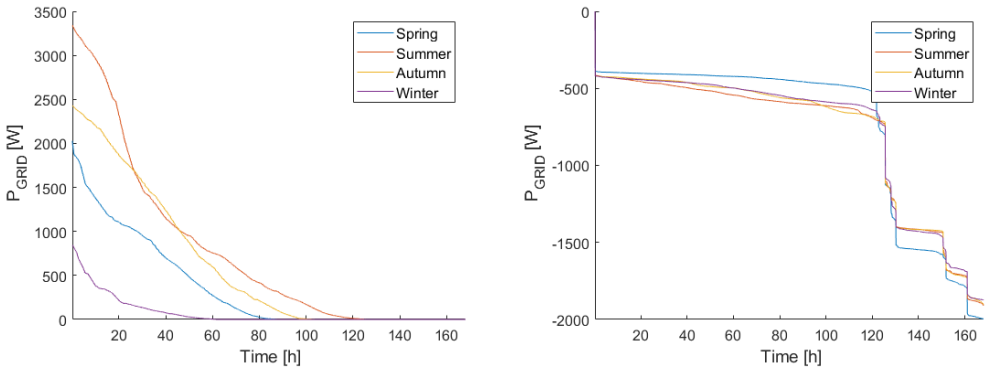

(a) Grid connection 1

(b) Grid connection 2

Figure 6.17: The LDC curve of scenario SA, where grid connection 1 represents the connection of the PV array and connection 2 the connection of the EVs and the load.

6.4.3.4 Scenario SC

Scenario SC allows the EVs to be charged by the PV power. This presents the advantages that local load can be supplied by local supply. Generally, this would only work if the EVs are present when the sun is shining and no form of energy storage is possible, which is in this scenario the case. Although, alternative situation are possible, the setup considered here is for an office building the most logical. Table 6.20 shows the power exchange over both grid connections. The effect of being able to supply the PV power directly to the EVs is visible. The power that is taken from the grid to charge the EVs is reduced significantly, especially for the Spring, Summer and Autumn week. The Autumn week evens requires the least power via this grid connection. A possible explanation for this that the load by the EVs has higher correlation with the generated PV power during this week compared to the other weeks. Also the power that is transferred to the grid is reduced significantly since it is being used directly by the EVs. The other grid connection shows no interesting results

since the normal load is fully provided for by the grid.

Table 6.20: Summary of scenario **SC** during a week in the four seasons. Grid1 represents the grid connection of the PV array and the EVs for scenario **SC**. Grid2 represents the connection of the load for scenario **SC**.

Season	**Spring**	**Summer**	**Autumn**	**Winter**	**Units**
From PV array	717.28	1531.53	1219.18	150.36	[kWh]
To the load	936.02	1040.20	1013.17	993.36	[kWh]
To the EVs	566.10	566.10	566.10	566.10	[kWh]
To the grid1	256.58	1062.95	662.96	16.28	[kWh]
From the grid1	105.39	97.52	10.22	430.20	[kWh]
To the grid2	0.00	0.00	0.00	0.00	[kWh]
From the grid2	936.02	1040.20	1013.17	993.36	[kWh]

The corresponding LDCs for scenario SC are shown in 6.18. In case of grid connection 1, the transfer of power shifts from predominantly transferring power to the grid during the Summer week to predominantly demanding power from the grid during the Winter week. Also, as result of internally supplying demand, the curves are more located around zero. Grid connection 2 shows no interesting results for the different weeks, whereas it only represents the power demanded by the load with small seasonal differences.

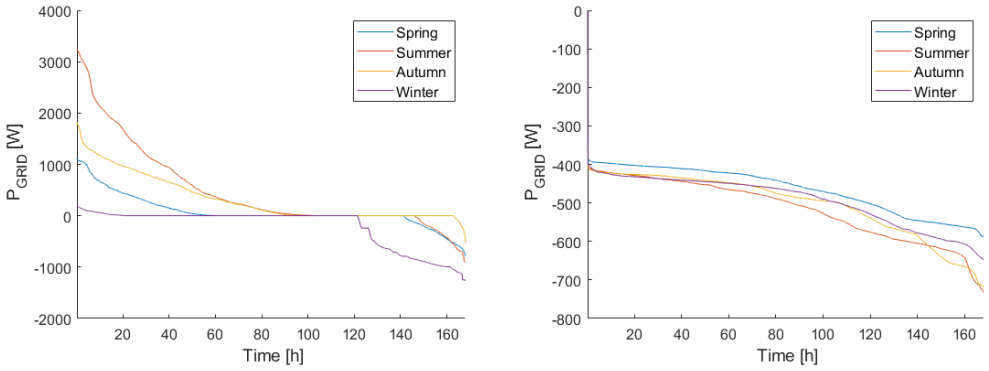

(a) Grid connection 1

(b) Grid connection 2

Figure 6.18: The LDC of scenario SC, where grid connection 1 represents the connection of the PV array and the EVs and connection 2 the connection of the load

6.4.3.5 Scenario SCL

Scenario SCL combines the PV generation, the load imposed by the EVs and the normal load, resulting in one grid connection in contrast to the previous two scenarios. Table 6.21 shows that this setup results in significant effects on the power exchange with the grid over this connection. The power transfer to the grid is reduced by more than half in all weeks and during the Winter week even to zero. Also, the power demanded from the grid is reduced significantly. Only, in the Winter week this effect is less since the generation of the PV array is also less. Almost half of the total internal demand can be supplied for in the other three weeks. Another interesting finding is that during the Autumn week less power is required from the grid compared to the Summer week even though more power

is generated then. Probably, the patterns of the PV generation and the total load in the Autumn week are more correlated than during the Summer week. The LDC in Figure 6.19 shows similar results. The graph of the Autumn is significantly more located around zero than the graph of the Summer week. Furthermore, when considering the LDCs of all four weeks, this scenario enables to minimize the burden on the grid to some reasonable extent.

Table 6.21: Summary of scenario **SCL** during a week in the four seasons. Grid represents the grid connection of the PV array, the EVs and the load.

Season	**Spring**	**Summer**	**Autumn**	**Winter**	**Units**
From PV array	717.28	1531.53	1219.18	150.36	[kWh]
To the load	936.02	1040.20	1013.17	993.36	[kWh]
To the EVs	566.10	566.10	566.10	566.10	[kWh]
To the grid	62.37	652.32	280.86	0.00	[kWh]
From the grid	847.21	727.08	640.95	1409.10	[kWh]

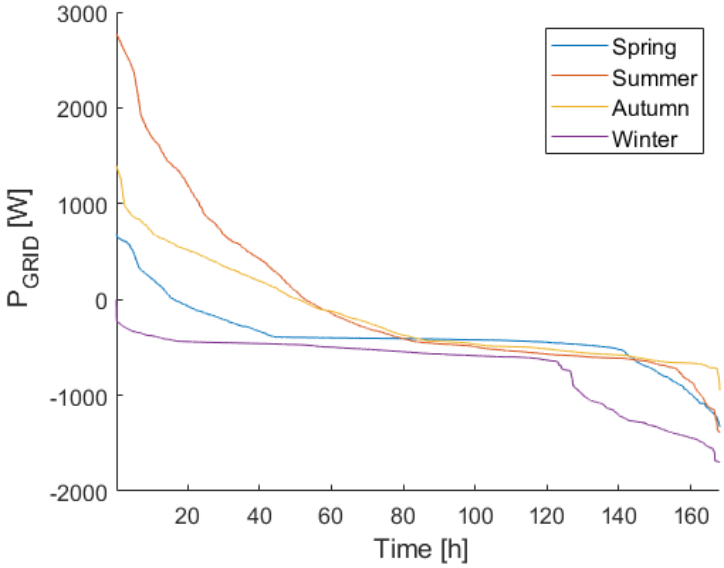

Figure 6.19: LDC for scenario SCL.

6.4.4 Concluding comparison

Now all individual scenarios are discussed, a comparison can be made. For this reason, the LDCs of the different seasons are combined and shown in Figure 6.20. In some scenarios the setup resulted in two independent grid connections. For these scenarios, the total power transfer to and from the grid of both connections, respectively, can be combined to make comparison with the other scenarios. The LDCs, however, cannot be combined since they would give a misrepresentation of the actual situation. More specifically, the role of the grid would be omitted if one connection is supplying power to the grid and one is demanding power.

Several scenarios, CONV, SA and SC, illustrate that if local demand or local supply are directly connected to the grid, it fully burdens the grid. As can be seen in Figure 6.20 and the individual tables, CONV (aligned with SA2), SA1, SA2 and SC2 represent a direct load or supply to the grid. Consequently, the performance of these scenarios or these connections

are the worst. The combination of local supply and demand in the scenarios SC1 and SCL show significant reductions on the actual power exchange with the grid. Using this principle works two ways. The load on the grid is reduced as well as the supply to the grid. The severity of this effect for the different setups differs considerably per seasons. This is largely due to the seasonality of the PV generation.

Also, when comparing SC and SCL, the addition of extra flexibility by combining an extra load in case of SCL, is beneficial to the performance of the setup. In line with this, the hybrid microgrid has an energy storage system as well as it can use the EVs as a storage system. Both provide even more flexibility. The result hereof can be seen when looking to the total power exchange with the grid and to the LDCs shown in Figure 6.20. In case of the hybrid microgrid, the performance is even better than in case of scenario SCL. This accounts even when the initial SOC of the BESS is taken out of the equation. It must, however, be mentioned that the performance of the hybrid microgrid does not differ significantly for the Winter week. The extra flexibility of the hybrid microgrid, has no significant extra effect if not enough PV power is generated.

Another interesting finding, based on the LDCs, is that the configuration of the hybrid microgrids allows the installment of a significantly sized solar PV array, almost without burdening the grid at all. This was considered as one of the advantages of the hybrid microgrid. Another advantage of the hybrid microgrid was that the hybrid microgrid would counteract the burden of the increase of EVs on the grid. To some extent this is indeed the case for the hybrid microgrid, as well as for SCL and SC. This, however, remains to depend on the local generation.

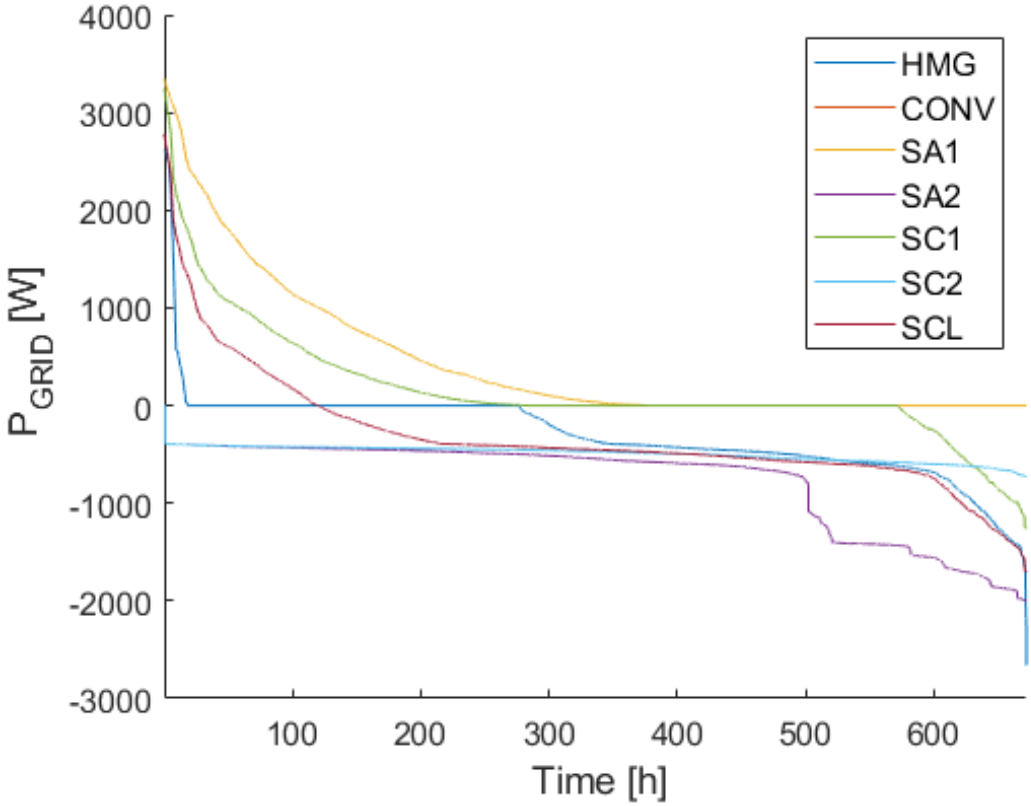

Figure 6.20: LDC curve of all weeks combined for all scenarios. HMG represent the LDC of the hybrid microgrid. Plots SA1 and SC1 represent connection 1 of both scenarios and SA2 and SC2 connection 2.

Chapter 7

Discussion

In this research a hybrid microgrid that includes a solar carport is designed. Its configuration is established based on an average Dutch sized office facility. Corresponding to this configuration a two-level control strategy is proposed. The higher-level is responsible for maintaining the overall power balance in the microgrid as well as providing setpoints for the lower-level controllers. Each lower-level controller has its own specific control objective ranging from maintaining the DC bus voltage in case of the BESS, to regulating the active power flow between the AC and DC microgrid by the ILC. The microgrid including its controllers are modeled in Matlab and Simulink to investigate the performance of the design. The individual control layers were analyzed first, after which the two-level control strategy was tested. Last, the simulation of the higher-level controller was used to gain insight into its performance compared to office facilities were the hybrid microgrid concept is not applied. During this research, in setting the system boundaries and scope, determining the model and defining the scenarios, decisions and assumptions have been made. All have affected the outcome of this research to some extent and resulted in limitations, which are discussed in this section. Also, the final results are put in perspective.

7.1 Impact of research setup

First of all, throughout this research the uncertainties were kept to minimum. This resulted in considering the PV generation, the demand and the details on the EVs to be known. Although, technology is able to predict PV generation to some reasonable extent these days [118] as well as allowing to determine and predict demand using load shifting [119], it cannot be considered a realistic representation. This assumption was, however, made to propose a first design of the control strategy as well as to gain insight into the potential of this system. This way an upper boundary is obtained, which means that if this research has in this setup no potential, it will definitely not have any with a more realistic approach. Also, it must be mentioned that although the effect of having unpredicted operating conditions have been tested in one set of scenarios, it is not representative for having no predictions of the load or PV pattern at all. It is, therefore, recommended to investigate this in future research.

Next, for the designed lower-level controllers of the EVs, the BESS and the ILC, only PI control was considered. This control technique was selected due to its simple design and application. Consequently, no other control techniques have been taken into consideration. Different control techniques could have been a better fit for designed the hybrid microgrid. This means that the design of the hybrid microgrid could be improved significantly by means of different control techniques. It is considered, however, outside the scope of this

research to investigate the use of different control techniques.

Furthermore, due to scope of this research an existing model was used for the representation of the MPPT converter for the solar array. Simulations show that the model is functioning sub-optimal compared to its functioning in the original model it was part of. The actual operation of the model was, however, not considered problematic and the model was able perform its designed functions to a reasonable extent. Especially, for the simulations and scenarios conducted in this research, the negative effect of the sub-optimal functioning model was minimized. The converter was less accurate in forcing the PV array to operate at the MPP for lower irradiance levels. Fortunately, in most scenarios high irradiance levels were simulated keeping the error to a minimum. Also, it had no effect on the scenarios including only the higher-level controller. In case the model would be improved in future research, the performance of the PV array in the Simulink model would benefit significantly.

In addition, Matlab and Simulink were used to model the hybrid microgrid, which resulted in several constraints for the simulations performed in this research. First of all, the sample time used for the MPC controller is 5 minutes. This was set to ensure reasonable computation times for the simulations. However, this sample time also results in a lower accuracy and a slower response rate. Due to the assumption that the PV generation, the demand, and the EV details are considered to be known, the negative impact of this sample time in the different simulations was kept to a minimum. Particularly, in case the microgrid would be subjected to more rapid and unexpected changes, a faster sample time becomes more important to prevent any harmful and undesired situations. Secondly, several scenarios, and especially scenario set 3 on the interaction between the two control layers and set 4 on the impact of the designed microgrid, were limited by the used software. To simulate 1 second in case of the Simulink simulation, 15 minutes of computation time was required. Simulation of longer than 10 seconds, were even aborted by the software itself, for running out of memory. For the Matlab calculations, the computation time was also the bottleneck. To model the MPC controller over a period of a week, 45 minutes were required. Although, a lot can be shown in several simulation of a week, it is impossible to capture the seasonal trends fully, extremes, and exemptions herein. The comparison of scenario 4 is for this reason not fully representative, even though it gives a good impression. It is considered likely that the Simulink model as well as the Matlab model can be improved in terms of calculation time. This is expected due to the modeling skills of the author as well as it was not the aim of this research to optimize the model in terms of computation time.

Moreover, the considered load pattern is not a load pattern of a typical office building in the Netherlands. Since actual load patterns for these types of facilities are not widely available, a pattern of the Lawrence Berkeley National Laboratory in the United Stated was used. Although, the amplitude of this pattern was adjusted such that it fits the relative load of a Dutch office building, the actual pattern is disputable for two reasons. First of all, the Lawrence Berkeley National Laboratory, is not considered as an average office building. Secondly, due to variances in geographical location, the resulting load pattern is also expected to be different. For example, lighting or temperature control can induce different load patterns. Consequently, the use hereof could lead to a mismatch with the used PV pattern. This should not result in a problem with the designed control strategy. It could, however, have an effect on the simulations of the impact of the hybrid microgrid on the internal supply and demand as well as on the power exchange with the grid. This effect adds on top of the effect of having selected only one week per season for the load and PV pattern.

7.2 Results in context

The design of the hybrid microgrid has shown promising results in the conducted scenarios, where it is compared to alternative scenarios. The results, however, only reflect the hybrid microgrid under a selection of circumstances. More extensive and realistic research and simulations are required to test the robustness of designed system as well as to investigate it under a broader variety of circumstances. Nonetheless, the proposed scenarios do allow for some initial conclusions.

In all conducted scenarios the PV generation, the EVs, the office load, and the BESS were relatively proportional to each other. This can be considered a success factor for the hybrid microgrid. In case the solar array would be significantly larger, the microgrid is not able to deal with the relative larger peaks. These will consequently be supplied to the grid. However, for the performance of the hybrid microgrid a larger solar array is beneficial. After all, the BESS was only rarely used to its full capacity. In case the solar array would be significantly smaller than considered in this research, the effect of the hybrid microgrid reduces and the configuration might be irrelevant.

A larger number of EVs or a higher demand would primarily result in needing more power form the grid. On the contrary, a lower number of EVs and a lower demand would reduce the dependency of the grid. The BESS would in this case store more power and for a longer period of time. Finally, the size of the BESS could be reduced slightly without affecting the performance of the hybrid microgrid too much. Also, a larger BESS would not improve the performance of the microgrid significantly. It would only take care of the highest PV generation peaks, which only occur rarely.

For the application of this type of hybrid microgrid, it is of importance to size the different components proportionally. Otherwise, the performance of the hybrid microgrid could be negatively be affected for the reasons discussed previously. When this is taken in consideration, it is expected that the hybrid microgrid could be beneficial for most office facilities with a local parking area.

Last, what is not considered in this research, but is highly relevant for the feasibility of the implementation of the hybrid microgrid, are the costs. The solar array, BESS and ILC are the components required to setup the hybrid microgrid. The induced costs for these components and for setting up the configuration are considered significant. Also, this research has not provided insights regarding the costs, direct and indirect, that are saved by using this type of system. For the actual implementation it is, therefore, recommended to first conduct a feasibility study.

Chapter 8

Conclusion

Due to the global energy transition, the growth of solar PV is expected to be inevitable. Together with the electrification of the transport sector, and thereby the increase in EVs, challenges and opportunities arise. Both, EVs and solar PV, have a DC interface and research has shown they can complement each other and balance out their negative effects. These advantages have been embraced in the development of DC microgrids, in the form of smart parking systems and solar carports. In this research, however, it is investigated what the impact is of solar carports as part of, a more complex AC/DC hybrid microgrid. The effect of this system on the power exchange with the grid, the internal supply and internal demand is of main interest.

An average dutch business premises with an adjacent parking lot, is taken as a reference system for the hybrid microgrid. The DC microgrid consists of the EVs, the solar PV array, representing the solar carport, and a battery storage system. The DC side was interconnected via the ILC to the AC microgrid, which includes the AC load, representing an office building, and a connection to the utility grid.

The microgrid is controlled via a two-level control strategy. The higher-level controller uses MPC to regulate the power balance in the microgrid and to determine the setpoints for the lower-level controllers. The lower-level control consists of four individual controllers, each with their own objective. First of all, the ILC is responsible for regulating the active power flow between the AC and the DC microgrid, for enforcing the generation of reactive current to zero, and for synchronizing the transferred power with the AC bus. Second, the controller of the BESS is taking care of maintaining the DC voltage and indirectly of the power transfer to and from the BESS. The controllers of the EVs are establishing a constant current flow to and from the EVs. Last, the controller of the solar array aims the array to constantly operate at the MPP.

The configuration of the hybrid microgrid and its control strategy are modeled in Matlab and Simulink. First, the lower-level controllers are analyzed to see whether they operate according to their intended design. To start, the ILC shows itself to be a stable component in the microgrid. It converges accurately to the setpoints it receives. The speed at which it converges could be improved since it is relatively slow in case of sudden large changes in setpoints. However, realistically these changes are highly unlikely, especially if a lower sample time for the higher-level controller is set, and therefore the design is considered to be sufficient for the purpose in this research. The converters of the BESS and EVs show accurate and fast responses under various circumstances and are therefore a perfect fit for the microgrid design. Finally, for the controller of the PV array, an existing model is used. Although, it does not operates to its maximum potential, it proves to be sufficiently accurate for the purpose of this design.

Second, the MPC controller is analyzed thoroughly with respect to setup of the controller as well as to the scalability of the design and the robustness. To start, longer prediction horizons enable the controller to better anticipate on the future developments of the microgrid. It, however, also results in an proportional increase in computation time. Therefore, a trade-off needs to be made in setting up the higher-level controller. Next, the effect of penalizing the power exchange with the BESS and EVs in the objective function is explored. The intention is to minimize unnecessary power flows within the microgrid, which is confirmed by the scenarios. Also, by altering the individual weights for the power exchange with the BESS and EVs priority can be given to one or the other depending on the preferred operation of the microgrid. Furthermore, the scalability of the controller was investigated. The scenarios show that the controller is able to control the microgrid without any problems with a significant increase in the number of EVs connected to the microgrid. Last, the controller is subjected to unpredicted circumstances. The results show that accurate predictions are beneficial for the performance of the microgrid. Unpredicted circumstances directly affect the efficiency of the microgrid in a negative way. There future improvements with respect to the robustness of the controller can be made.

Thirdly, the two-level control strategy was investigated. The MPC controller provided setpoints for the lower-level controllers, which were converged to accurately. The PV array generated less than predicted, which was expected based on the not optimally functioning MPPT converter. Furthermore, due to design of the controller of the BESS the power transferred to the BESS was also less. The controller of the BESS only transfers power indirectly. Consequently, the error of the generated PV power, as well as the other losses in the DC side of the microgrid, sum up and result in a lower power flow than expected to the BESS. Similarly, the system losses on the AC side of the microgrid result in a nonzero power exchange with the grid since it operates as an infinite bus.

Finally, the hybrid microgrid was compared to four alternative configurations. All scenarios were simulated over four different weeks, each in a different season. For these simulations, only the higher-level controller was utilized. Based on these simulations, the hybrid microgrid shows promising results. Especially, during the months with relatively more solar PV generation, the effect of the hybrid microgrid configuration was most promising.

Appendix A

Appendix

A.1 Scenario 1

Table A.1: Reference hybrid microgrid at $t = 0$ for the scenarios of the lower-level controllers

Symbol	Description	Value	Unit
GHI	Radiation received by solar array	500	$[W/m^2]$
P^*_{ILC}	ILC reference power	0	$[W]$
I^*_{EV}	EV reference current	-10	$[A]$
SOC_{EV}	SOC of EV	50	$[\%]$
SOC_{BESS}	SOC of BESS	50	$[\%]$
P_{LOAD}	AC power demand	10000	$[W]$
m	Number of EVs	1	$[-]$

A.2 Scenario 2

A.2.1 Effect of different prediction horizons on EVs

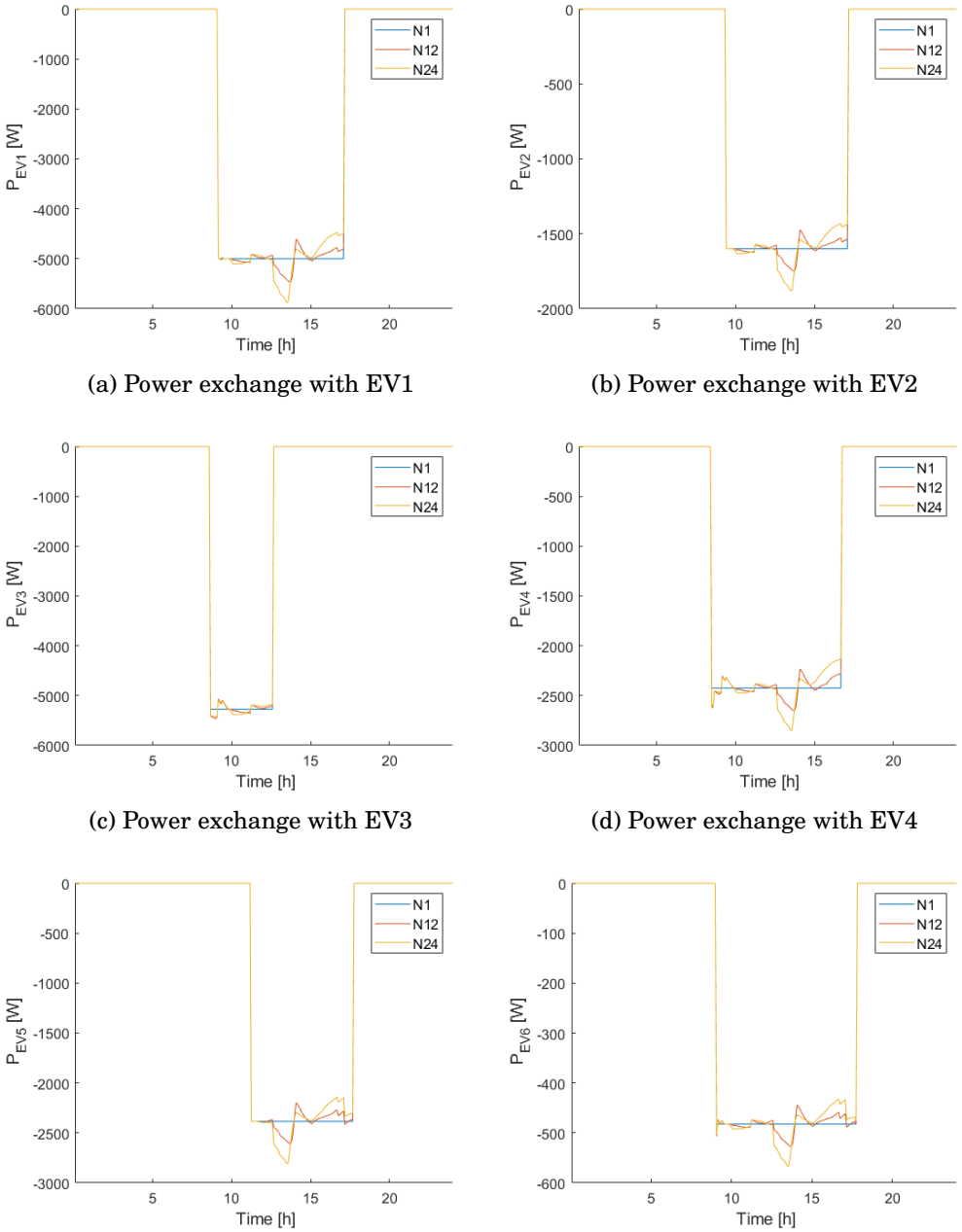

(a) Power exchange with EV1

(b) Power exchange with EV2

(c) Power exchange with EV3

(d) Power exchange with EV4

(e) Power exchange with EV5

(f) Power exchange with EV6

Figure A.1: The power exchange with the EVs for the different prediction horizons

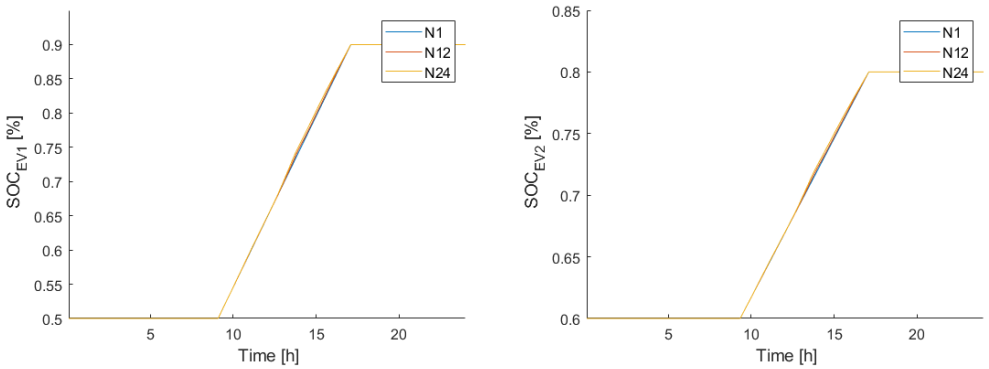

(a) SOC of EV1

(b) SOC of EV2

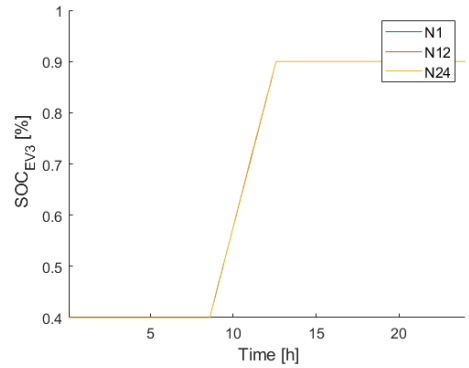

(c) SOC of EV3

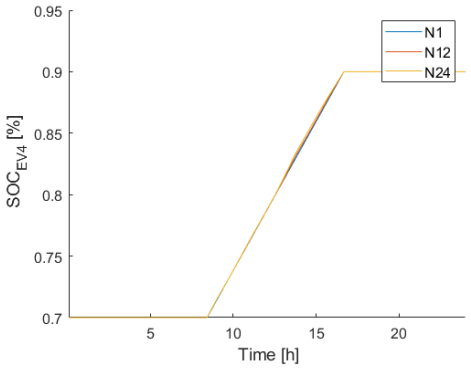

(d) SOC of EV4

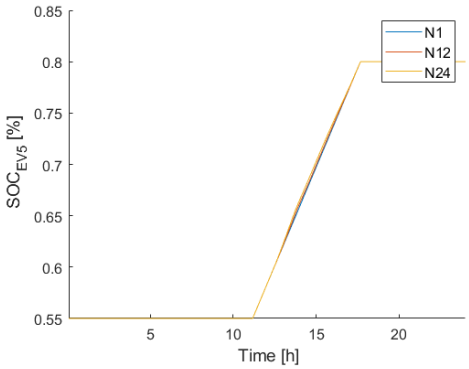

(e) SOC of EV5

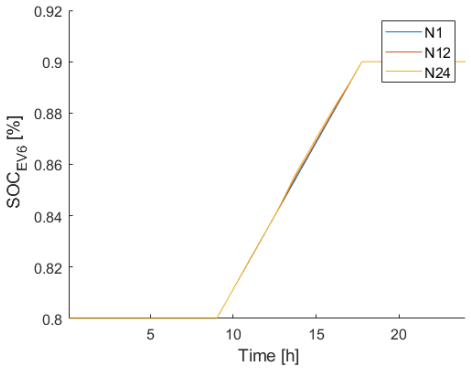

(f) SOC of EV6

Figure A.2: The SOC of the EVs for the different prediction horizons

A.2.2 Effect of different weights in the cost function on EVs

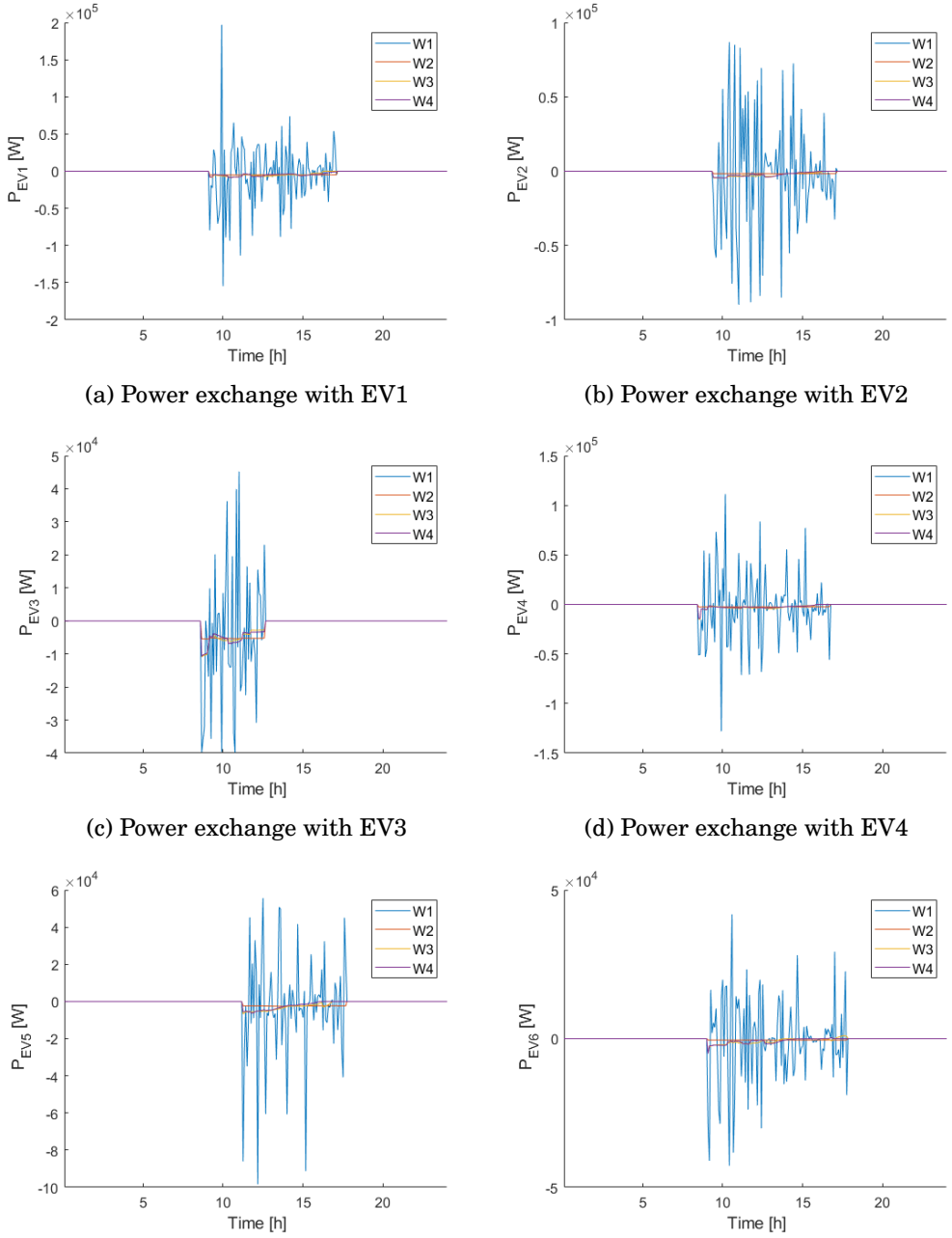

(a) Power exchange with EV1

(b) Power exchange with EV2

(c) Power exchange with EV3

(d) Power exchange with EV4

(e) Power exchange with EV5

(f) Power exchange with EV6

Figure A.3: The power exchange with the EVs for different weights in the cost function

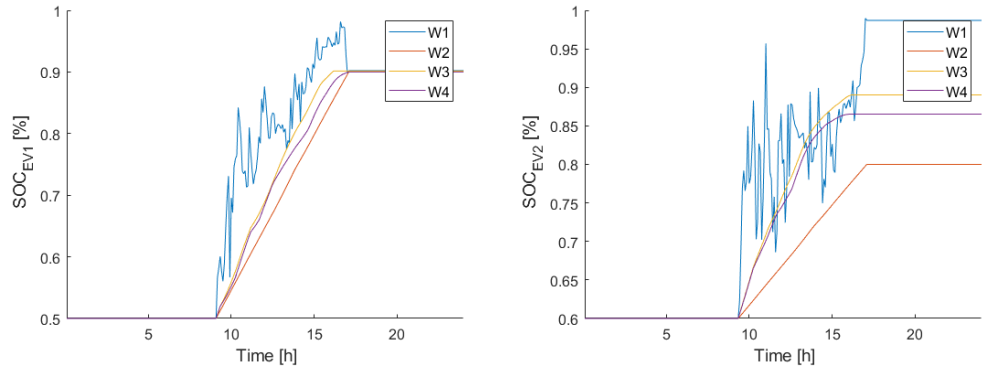

(a) SOC of EV1

(b) SOC of EV2

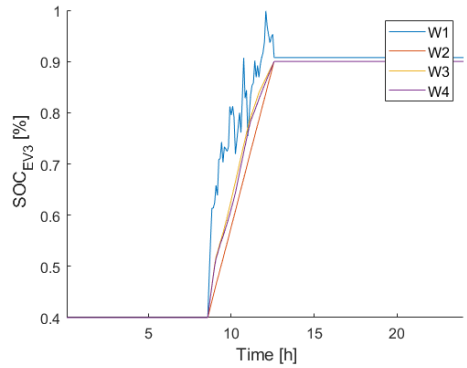

(c) SOC of EV3

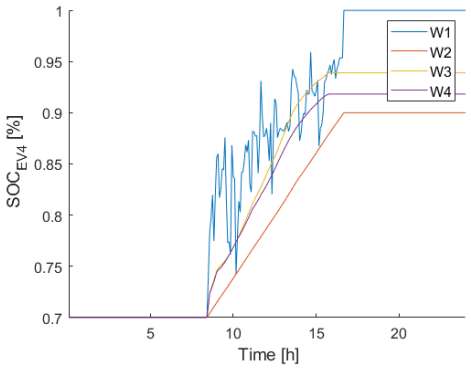

(d) SOC of EV4

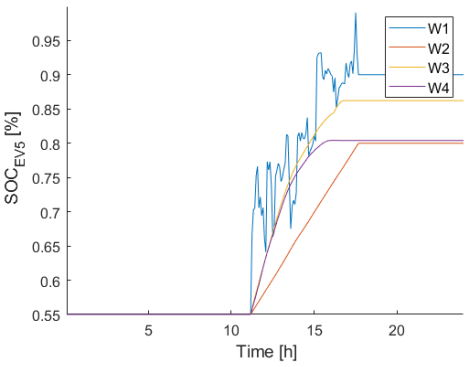

(e) SOC of EV5

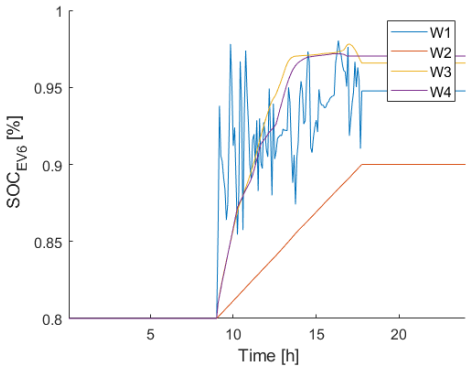

(f) SOC of EV6

Figure A.4: The SOC of the EVs for different weights in the cost function

A.2.3 Parameters of the EVs

Table A.2: Parameters of the EVs for the different scenarios with varying numbers of EVs

EV index	Type	SOC_{arr}	SOC_{des}	t_{arr}	t_{dep}
1	Tesla s	50%	90%	09:00:00	17:00:00
2	Nissan Leaf e+	60%	80%	09:15:00	17:00:00
3	BMW i3s	40%	90%	08:30:00	12:30:00
4	Tesla s	70%	90%	08:20:00	16:35:00
5	Nissan Leaf e+	55%	80%	11:05:00	17:35:00
6	BMW i3s	80%	90%	08:55:00	17:40:00
7	Nissan Leaf e+	30%	65%	11:05:00	18:30:00
8	Nissan Leaf e+	50%	75%	08:00:00	16:40:00
9	Tesla s	45%	55%	10:25:00	19:20:00
10	Tesla s	70%	100%	09:30:00	17:30:00
11	BMW i3s	35%	55%	11:50:00	16:00:00
12	Tesla s	25%	35%	07:20:00	19:05:00
13	Nissan Leaf e+	55%	80%	09:20:00	17:00:00
14	Tesla s	50%	80%	11:55:00	19:50:00
15	BMW i3s	50%	60%	09:25:00	18:35:00
16	BMW i3s	55%	100%	10:45:00	16:40:00
17	BMW i3s	55%	100%	07:40:00	17:55:00
18	BMW i3s	30%	40%	10:35:00	17:55:00
19	Tesla s	65%	80%	07:45:00	17:50:00
20	Nissan Leaf e+	45%	90%	10:05:00	16:55:00
21	BMW i3s	55%	90%	08:40:00	15:35:00
22	BMW i3s	35%	85%	11:25:00	15:25:00
23	Nissan Leaf e+	55%	95%	11:00:00	15:05:00
24	BMW i3s	35%	85%	08:05:00	18:20:00
25	Nissan Leaf e+	20%	30%	08:15:00	16:55:00
26	BMW i3s	60%	85%	08:50:00	15:10:00
27	Tesla s	25%	35%	07:40:00	15:35:00
28	BMW i3s	35%	55%	10:40:00	19:30:00
29	Nissan Leaf e+	25%	65%	10:35:00	15:55:00
30	BMW i3s	60%	100%	09:45:00	19:40:00
31	Tesla s	60%	75%	10:45:00	15:40:00
32	BMW i3s	20%	40%	07:10:00	17:55:00
33	Nissan Leaf e+	25%	45%	11:55:00	16:10:00
34	Nissan Leaf e+	70%	80%	07:05:00	15:35:00
35	Nissan Leaf e+	65%	90%	08:05:00	19:05:00
36	BMW i3s	70%	90%	09:10:00	19:30:00
37	BMW i3s	65%	100%	10:15:00	19:00:00
38	BMW i3s	50%	80%	10:30:00	17:30:00
39	Tesla s	35%	55%	11:40:00	15:55:00
40	BMW i3s	50%	95%	08:40:00	15:25:00

A.3 Scenario 3

A.3.1 Setup

Table A.3: Simulation state values at t_0 = 11:00

Symbol	Value	Unit
SOC_{BESS}	55.23	[%]
SOC_{EV1}	72.04%	[%]
$PRES_{EV1}$	1	[-]
SOC_{EV2}	43.55%	[%]
$PRES_{EV2}$	1	[-]
SOC_{EV3}	40.00%	[%]
$PRES_{EV3}$	0	[-]
P_{ILC}	9062.9	[W]

A.4 Scenario 4

A.4.1 Solar PV generation

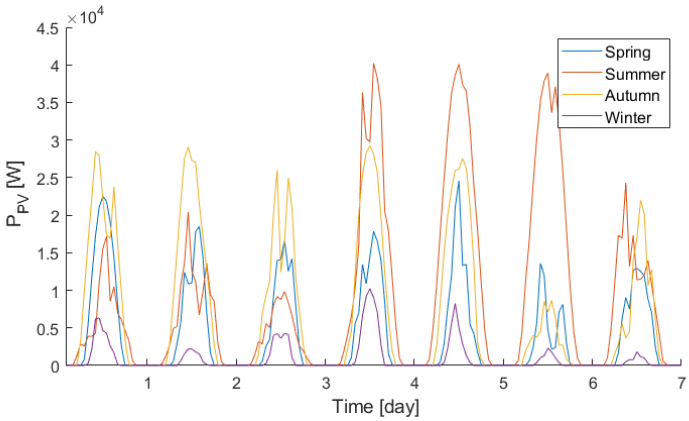

Figure A.5: Four PV generation patterns used in Scenario set 4

A.4.2 AC load

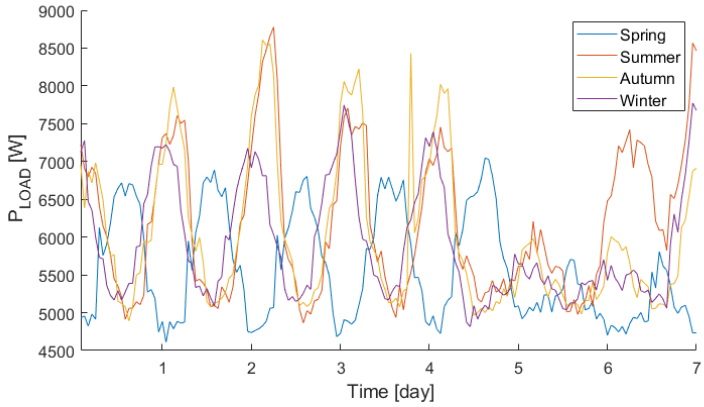

Figure A.6: Four load patterns used in Scenario set 4

A.4.3 EVs during four seasons

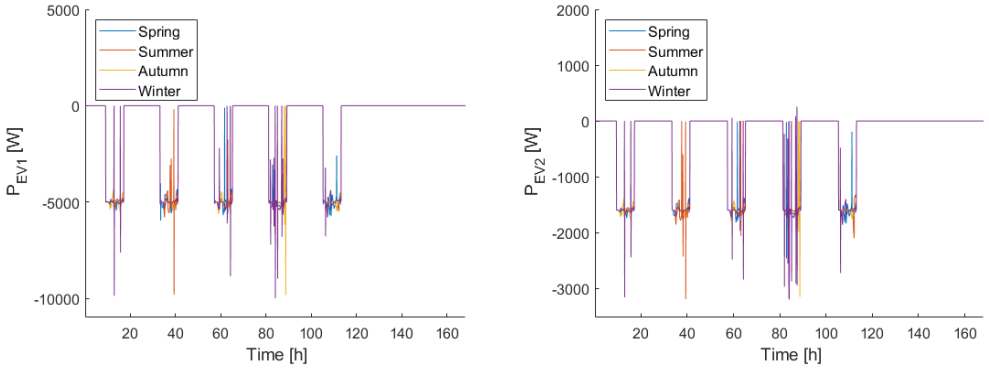

(a) Power exchange with EV1

(b) Power exchange with EV2

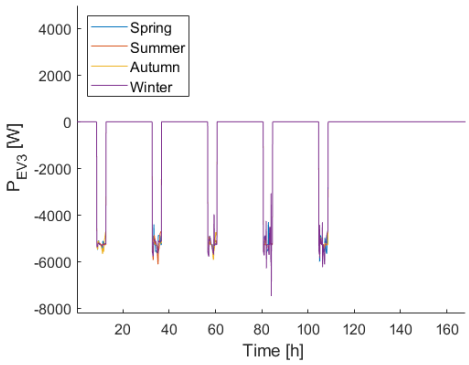

(c) Power exchange with EV3

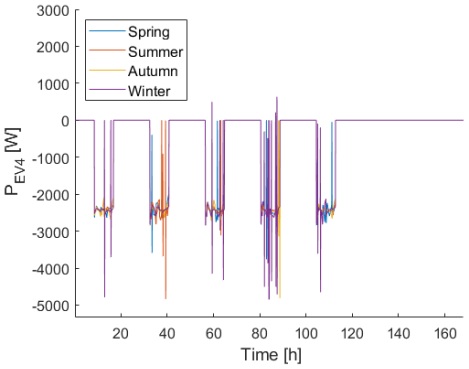

(d) Power exchange with EV4

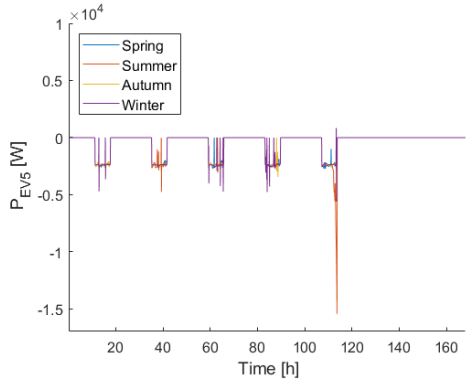

(e) Power exchange with EV5

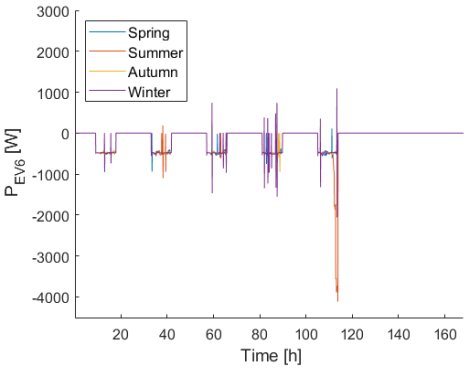

(f) Power exchange with EV6

Figure A.7: The power exchange with the EVs for the different prediction horizons

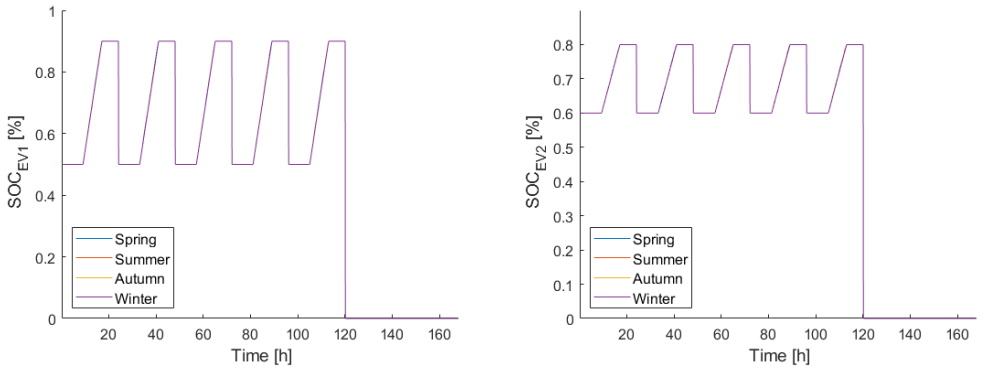

(a) SOC of EV1

(b) SOC of EV2

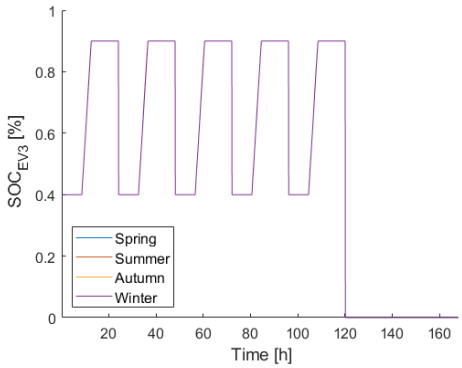

(c) SOC of EV3

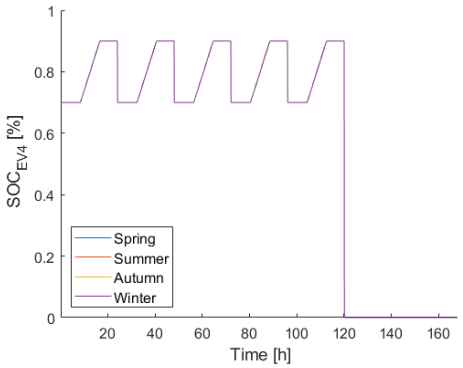

(d) SOC of EV4

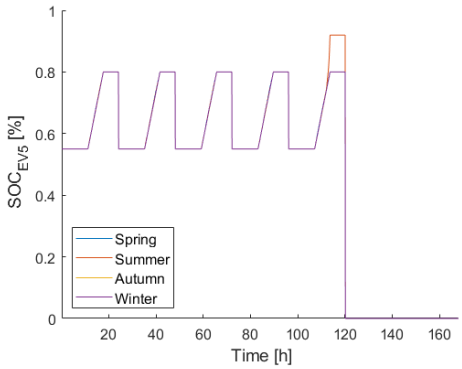

(e) SOC of EV5

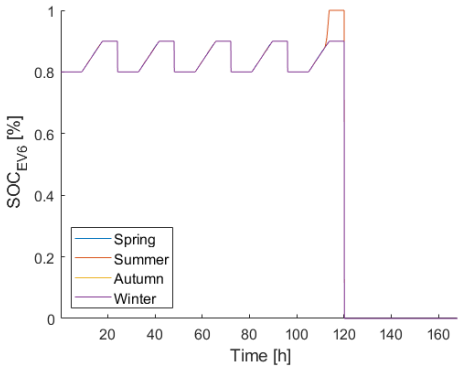

(f) SOC of EV6

Figure A.8: The SOC of the EVs for the different prediction horizons

Bibliography

[1] IRENA. Power system flexibility for the energy transition, Nov 2018.

[2] Sherif M Ismael, Shady HE Abdel Aleem, Almoataz Y Abdelaziz, and Ahmed F Zobaa. State-of-the-art of hosting capacity in modern power systems with distributed generation. *Renewable energy*, 130:1002–1020, 2019.

[3] Robert H Lasseter. Microgrids. In *2002 IEEE Power Engineering Society Winter Meeting. Conference Proceedings (Cat. No. 02CH37309)*, volume 1, pages 305–308. IEEE, 2002.

[4] Ajay Gupta, Suryanarayana Doolla, and Kishore Chatterjee. Hybrid ac–dc microgrid: systematic evaluation of control strategies. *IEEE Transactions on Smart Grid*, 9(4):3830–3843, 2018.

[5] Eneko Unamuno and Jon Andoni Barrena. Hybrid ac/dc microgrids—part i: Review and classification of topologies. *Renewable and Sustainable Energy Reviews*, 52:1251–1259, 2015.

[6] Xiong Liu, Peng Wang, and Poh Chiang Loh. A hybrid ac/dc micro-grid. In *2010 Conference Proceedings IPEC*, pages 746–751. IEEE, 2010.

[7] Xiong Liu, Peng Wang, and Poh Chiang Loh. A hybrid ac/dc microgrid and its coordination control. *IEEE Transactions on smart grid*, 2(2):278–286, 2011.

[8] Tan Ma and Osama A Mohammed. Optimal charging of plug-in electric vehicles for a car-park infrastructure. *IEEE Transactions on Industry Applications*, 50(4):2323–2330, 2014.

[9] Pedro Nunes, Tiago Farias, and Miguel C Brito. Enabling solar electricity with electric vehicles smart charging. *Energy*, 87:10–20, 2015.

[10] Pedro Nunes, Raquel Figueiredo, and Miguel C Brito. The use of parking lots to solar-charge electric vehicles. *Renewable and Sustainable Energy Reviews*, 66:679–693, 2016.

[11] Uwakwe C Chukwu and Satish M Mahajan. V2g parking lot with pv rooftop for capacity enhancement of a distribution system. *IEEE Transactions on Sustainable Energy*, 5(1):119–127, 2013.

[12] Francis K Tuffner, Forrest S Chassin, Michael CW Kintner-Meyer, and Krishnan Gowri. Utilizing electric vehicles to assist integration of large penetrations of distributed photovoltaic generation capacity. Technical report, Pacific Northwest National Lab.(PNNL), Richland, WA (United States), 2012.

[13] MF Shaaban, AA Eajal, and EF El-Saadany. Coordinated charging of plug-in hybrid electric vehicles in smart hybrid ac/dc distribution systems. *Renewable Energy*, 82:92–99, 2015.

[14] Md Shamiur Rahman, MJ Hossain, and Junwei Lu. Utilization of parked ev-ess for power management in a grid-tied hybrid ac/dc microgrid. In *2015 Australasian universities power engineering conference (AUPEC)*, pages 1–6. IEEE, 2015.

[15] Md Shamiur Rahman, MJ Hossain, and Junwei Lu. Coordinated control of three-phase ac and dc type ev–esss for efficient hybrid microgrid operations. *Energy conversion and management*, 122:488–503, 2016.

[16] Md Shamiur Rahman, MJ Hossain, FHM Rafi, and Junwei Lu. Ev charging in a commercial hybrid ac/dc microgrid: Configuration, control and impact analysis. In *2016 Australasian Universities Power Engineering Conference (AUPEC)*, pages 1–6. IEEE, 2016.

[17] Ying Chen, Wen Wei, Fengyan Zhang, Chengyun Liu, and Chao Meng. Design of pv hybrid dc/ac microgrid for electric vehicle charging station. In *2017 IEEE Transportation Electrification Conference and Expo, Asia-Pacific (ITEC Asia-Pacific)*, pages 1–6. IEEE, 2017.

[18] Md Shamiur Rahman, MJ Hossain, Junwei Lu, and Hemanshu Roy Pota. A need-based distributed coordination strategy for ev storages in a commercial hybrid ac/dc microgrid with an improved interlinking converter control topology. *IEEE Transactions on Energy Conversion*, 33(3):1372–1383, 2018.

[19] De Groene Energie Maatschappij. Solar canopies en laad infrastructuren.

[20] Harm Olthof. Onderzoek oppervlaktegegevens utiliteitsbouw (geon), 2012.

[21] CBS. Energiekentallen utiliteitsbouw dienstensector; oppervlakteklasse. Jan 2019.

[22] Asten. *Parkeernormennota 2016*. Dec 2016.

[23] Zhenhua Jiang and Roger A Dougal. Hierarchical microgrid paradigm for integration of distributed energy resources. In *2008 IEEE Power and Energy Society General Meeting-Conversion and Delivery of Electrical Energy in the 21st Century*, pages 1–8. IEEE, 2008.

[24] Zhenhua Jiang and Xunwei Yu. Power electronics interfaces for hybrid dc and ac-linked microgrids. In *2009 IEEE 6th International Power Electronics and Motion Control Conference*, pages 730–736. IEEE, 2009.

[25] Sixifo Falcones, Xiaolin Mao, and Raja Ayyanar. Topology comparison for solid state transformer implementation. In *Power and Energy Society General Meeting, 2010 IEEE*, pages 1–8. Citeseer, 2010.

[26] Xu She, Alex Q Huang, Srdjan Lukic, and Mesut E Baran. On integration of solid-state transformer with zonal dc microgrid. *IEEE Transactions on Smart Grid*, 3(2):975–985, 2012.

[27] Xunwei Yu, Xu She, Xiaohu Zhou, and Alex Q Huang. Power management for dc microgrid enabled by solid-state transformer. *IEEE Transactions on Smart Grid*, 5(2):954–965, 2013.

[28] Liang Wang, Donglai Zhang, Yi Wang, Bin Wu, and Hussain S Athab. Power and voltage balance control of a novel three-phase solid-state transformer using multilevel cascaded h-bridge inverters for microgrid applications. *IEEE Transactions on Power Electronics*, 31(4):3289–3301, 2015.

[29] Jiahong Yan, Xiangqi Zhu, and Ning Lu. Smart hybrid house test systems in a solid-state transformer supplied microgrid. In *2015 IEEE Power & Energy Society General Meeting*, pages 1–5. IEEE, 2015.

[30] Jasem Khajesalehi, Keyhan Sheshyekani, Mohsen Hamzeh, and Ebrahim Afjei. Maximum constant boost approach for controlling quasi-z-source-based interlinking converters in hybrid ac–dc microgrids. *IET Generation, Transmission & Distribution*, 10(4):938–948, 2016.

[31] Manoranjan Sahoo and K Siva Kumar. Bidirectinal switched boost converter for ac-dc hybrid microgrid. In *2014 IEEE Applied Power Electronics Conference and Exposition-APEC 2014*, pages 2231–2236. IEEE, 2014.

[32] Lei Zhang, Feng Gao, Nan Li, Qian Zhang, and Chunyi Wang. Interlinking modular multilevel converter of hybrid ac-dc distribution system with integrated battery energy storage. In *2015 IEEE Energy Conversion Congress and Exposition (ECCE)*, pages 70–77. IEEE, 2015.

[33] Poh Chiang Loh, Ding Li, Yi Kang Chai, and Frede Blaabjerg. Autonomous control of interlinking converter with energy storage in hybrid ac–dc microgrid. *IEEE transactions on industry applications*, 49(3):1374–1382, 2013.

[34] Ritwik Majumder. A hybrid microgrid with dc connection at back to back converters. *IEEE Transactions on Smart Grid*, 5(1):251–259, 2013.

[35] Chung-Chuan Hou and Yung-Fu Huang. Diode rectifier with auxiliary converter for hybrid ac/dc microgrids. *IEEE Journal of Emerging and Selected Topics in Power Electronics*, 2(4):1059–1069, 2014.

[36] Abdelazeem A Abdelsalam, Hossam A Gabbar, and Adel M Sharaf. Performance enhancement of hybrid ac/dc microgrid based d-facts. *International Journal of Electrical Power & Energy Systems*, 63:382–393, 2014.

[37] Amr Ahmed A Radwan and Yasser Abdel-Rady I Mohamed. Assessment and mitigation of interaction dynamics in hybrid ac/dc distribution generation systems. *IEEE Transactions on Smart Grid*, 3(3):1382–1393, 2012.

[38] Abdulkerim Karabiber, Cemal Keles, Asim Kaygusuz, and B Baykant Alagoz. An approach for the integration of renewable distributed generation in hybrid dc/ac microgrids. *Renewable Energy*, 52:251–259, 2013.

[39] Ruwan PS Chandrasena, Farhad Shahnia, Sumedha Rajakaruna, and Arindam Ghosh. Dynamic operation and control of a hybrid nanogrid system for future community houses. *IET Generation, Transmission & Distribution*, 9(11):1168–1178, 2015.

[40] Hua Han, Xiaochao Hou, Jian Yang, Jifa Wu, Mei Su, and Josep M Guerrero. Review of power sharing control strategies for islanding operation of ac microgrids. *IEEE Transactions on Smart Grid*, 7(1):200–215, 2015.

[41] Tomislav Dragičević, Xiaonan Lu, Juan C Vasquez, and Josep M Guerrero. Dc microgrids—part i: A review of control strategies and stabilization techniques. *IEEE Transactions on power electronics*, 31(7):4876–4891, 2015.

[42] Juan P Torreglosa, Pablo Garcia-Trivino, Luis M Fernandez-Ramirez, and Francisco Jurado. Control strategies for dc networks: A systematic literature review. *Renewable and Sustainable Energy Reviews*, 58:319–330, 2016.

[43] Chi Jin, Poh Chiang Loh, Peng Wang, Yang Mi, and Frede Blaabjerg. Autonomous operation of hybrid ac-dc microgrids. In *2010 IEEE International Conference on Sustainable Energy Technologies (ICSET)*, pages 1–7. IEEE, 2010.

[44] Poh Chiang Loh, Ding Li, Yi Kang Chai, and Frede Blaabjerg. Hybrid ac–dc microgrids with energy storages and progressive energy flow tuning. *IEEE transactions on power electronics*, 28(4):1533–1543, 2012.

[45] Mehdi Baharizadeh, Hamid Reza Karshenas, and Josep M Guerrero. Control strategy of interlinking converters as the key segment of hybrid ac–dc microgrids. *IET Generation, Transmission & Distribution*, 10(7):1671–1681, 2016.

[46] Yao Liu, Xiaochao Hou, Xiaofeng Wang, Chao Lin, and Josep Guerrero. A coordinated control for photovoltaic generators and energy storages in low-voltage ac/dc hybrid microgrids under islanded mode. *Energies*, 9(8):651, 2016.

[47] Yanghong Xia, Yonggang Peng, Pengcheng Yang, Miao Yu, and Wei Wei. Distributed coordination control for multiple bidirectional power converters in a hybrid ac/dc microgrid. *IEEE Transactions on Power Electronics*, 32(6):4949–4959, 2016.

[48] Ye Zhang, Hong Jie Jia, and Li Guo. Energy management strategy of islanded microgrid based on power flow control. In *2012 IEEE PES Innovative Smart Grid Technologies (ISGT)*, pages 1–8. IEEE, 2012.

[49] Payam Teimourzadeh Baboli, Mahdi Shahparasti, Mohsen Parsa Moghaddam, Mahmoud Reza Haghifam, and Mustafa Mohamadian. Energy management and operation modelling of hybrid ac–dc microgrid. *IET Generation, Transmission & Distribution*, 8(10):1700–1711, 2014.

[50] Mehdi Hosseinzadeh and Farzad Rajaei Salmasi. Power management of an isolated hybrid ac/dc micro-grid with fuzzy control of battery banks. *IET Renewable Power Generation*, 9(5):484–493, 2015.

[51] Xiao Jianfang, Wang Peng, Leonardy Setyawan, Jin Chi, and Choo Fook Hoong. Energy management system for control of hybrid ac/dc microgrids. In *2015 IEEE 10th Conference on Industrial Electronics and Applications (ICIEA)*, pages 778–783. IEEE, 2015.

[52] Mehdi Hosseinzadeh and Farzad Rajaei Salmasi. Robust optimal power management system for a hybrid ac/dc micro-grid. *IEEE Transactions on Sustainable Energy*, 6(3):675–687, 2015.

[53] Philip J Hart, TM Jahns, and RH Lasseter. Performance characteristics of a hybrid certs microgrid electric vehicle charging station. In *2014 IEEE Energy Conversion Congress and Exposition (ECCE)*, pages 3309–3316. IEEE, 2014.

[54] Peng Wang, Chi Jin, Dexuan Zhu, Yi Tang, Poh Chiang Loh, and Fook Hoong Choo. Distributed control for autonomous operation of a three-port ac/dc/ds hybrid microgrid. *IEEE Transactions on Industrial Electronics*, 62(2):1279–1290, 2014.

[55] Chengshan Wang, Xialin Li, Li Guo, and Yun Wei Li. A nonlinear-disturbance-observer-based dc-bus voltage control for a hybrid ac/dc microgrid. *IEEE Transactions on Power Electronics*, 29(11):6162–6177, 2014.

[56] Peng Wang, Xiong Liu, Chi Jin, Pohchiang Loh, and Fookhoong Choo. A hybrid ac/dc micro-grid architecture, operation and control. In *2011 IEEE Power and Energy Society General Meeting*, pages 1–8. IEEE, 2011.

[57] Mir Nahidul Ambia, Ahmed Al-Durra, Cedric Caruana, and SM Muyeen. Islanding operation of hybrid microgrids with high integration of wind driven cage induction generators. *Sustainable Energy Technologies and Assessments*, 13:68–75, 2016.

[58] Huaguang Zhang, Jianguo Zhou, Qiuye Sun, Josep M Guerrero, and Dazhong Ma. Data-driven control for interlinked ac/dc microgrids via model-free adaptive control and dual-droop control. *IEEE Transactions on Smart Grid*, 8(2):557–571, 2015.

[59] Xiaonan Lu, Josep Guerrero, Remus Teodorescu, Tamas Kerekes, Kai Sun, and Lipei Huang. Control of parallel-connected bidirectional ac-dc converters in stationary frame for microgrid application. In *2011 IEEE Energy Conversion Congress and Exposition*, pages 4153–4160. IEEE, 2011.

[60] Xiongfei Wang, Yun Wei Li, Frede Blaabjerg, and Poh Chiang Loh. Virtual-impedance-based control for voltage-source and current-source converters. *IEEE Transactions on Power Electronics*, 30(12):7019–7037, 2014.

[61] Xiaonan Lu, Josep M Guerrero, Kai Sun, Juan C Vasquez, Remus Teodorescu, and Lipei Huang. Hierarchical control of parallel ac-dc converter interfaces for hybrid microgrids. *IEEE Transactions on Smart Grid*, 5(2):683–692, 2013.

[62] Huagen Xiao, An Luo, Zhikang Shuai, Guobin Jin, and Yuan Huang. An improved control method for multiple bidirectional power converters in hybrid ac/dc microgrid. *IEEE Transactions on Smart Grid*, 7(1):340–347, 2015.

[63] AA Eajal, EF El-Saadany, and K Ponnambalam. Inexact power sharing in ac/dc hybrid microgrids. In *2016 IEEE Canadian Conference on Electrical and Computer Engineering (CCECE)*, pages 1–5. IEEE, 2016.

[64] AA Eajal, EF El-Saadany, and K Ponnambalam. Equal power sharing in islanded ac/dc hybrid microgrids. In *2016 IEEE Electrical Power and Energy Conference (EPEC)*, pages 1–6. IEEE, 2016.

[65] Josep M Guerrero, Mukul Chandorkar, Tzung-Lin Lee, and Poh Chiang Loh. Advanced control architectures for intelligent microgrids—part i: Decentralized and hierarchical control. *IEEE Transactions on Industrial Electronics*, 60(4):1254–1262, 2012.

[66] Abedalsalam Bani-Ahmed, Luke Weber, Adel Nasiri, and Hossein Hosseini. Microgrid communications: State of the art and future trends. In *2014 International Conference on Renewable Energy Research and Application (ICRERA)*, pages 780–785. IEEE, 2014.

[67] Amr Ahmed A Radwan and Yasser Abdel-Rady I Mohamed. Networked control and power management of ac/dc hybrid microgrids. *IEEE Systems Journal*, 11(3):1662–1673, 2014.

[68] Chi Jin, Junjun Wang, Koh Leong Hai, Choo Fook Hoong, and Peng Wang. Coordination secondary control for autonomous hybrid ac/dc microgrids with global power sharing operation. In *IECON 2016-42nd Annual Conference of the IEEE Industrial Electronics Society*, pages 4066–4071. IEEE, 2016.

[69] P Teimourzadeh Baboli, S Bahramara, M Parsa Moghaddam, and M-R Haghifam. A mixed-integer linear model for optimal operation of hybrid ac-dc microgrid considering renewable energy resources and phevs. In *2015 IEEE Eindhoven PowerTech*, pages 1–5. IEEE, 2015.

[70] A Bracale, P Caramia, and F Mottola. A cost minimization strategy for the control of hybrid ac-dc microgrids in industrial systems. In *2015 International Conference on Clean Electrical Power (ICCEP)*, pages 40–47. IEEE, 2015.

[71] Saeed Dehghan Manshadi and Mohammad Khodayar. Decentralized operation framework for hybrid ac/dc microgrid. In *2016 North American Power Symposium (NAPS)*, pages 1–6. IEEE, 2016.

[72] Nabil Qachchachi, Hassane Mahmoudi, and Abdennebi El Hasnaoui. Optimal power flow for a hybrid ac/dc microgrid. In *2014 International Renewable and Sustainable Energy Conference (IRSEC)*, pages 559–564. IEEE, 2014.

[73] Shahab Bahrami, Vincent WS Wong, and Juri Jatskevich. Optimal power flow for ac-dc networks. In *2014 IEEE International Conference on Smart Grid Communications (SmartGridComm)*, pages 49–54. IEEE, 2014.

[74] P Caramia, G Carpinelli, F Mottola, and G Russo. An optimal control of distributed energy resources to improve the power quality and to reduce energy costs of a hybrid ac-dc microgrid. In *2016 IEEE 16th International Conference on Environment and Electrical Engineering (EEEIC)*, pages 1–7. IEEE, 2016.

[75] Nandkishor Kinhekar, Narayana Prasad Padhy, Furong Li, and Hari Om Gupta. Utility oriented demand side management using smart ac and micro dc grid cooperative. *IEEE Transactions on Power Systems*, 31(2):1151–1160, 2015.

[76] Mehrdad Yazdanian and Ali Mehrizi-Sani. Distributed control techniques in microgrids. *IEEE Transactions on Smart Grid*, 5(6):2901–2909, 2014.

[77] Vladimir Toro and Eduardo Mojica-Nava. Microgrids coordination based on heterogeneous multi-agent systems. In *2015 IEEE 2nd Colombian Conference on Automatic Control (CCAC)*, pages 1–5. IEEE, 2015.

[78] H Nwe Aung, AM Khambadkone, Dipti Srinivasan, and T Logenthiran. Agent-based intelligent control for real-time operation of a microgrid. In *2010 Joint International Conference on Power Electronics, Drives and Energy Systems & 2010 Power India*, pages 1–6. IEEE, 2010.

[79] Liang Che, Mohammad Shahidehpour, Ahmed Alabdulwahab, and Yusuf Al-Turki. Hierarchical coordination of a community microgrid with ac and dc microgrids. *IEEE Transactions on smart grid*, 6(6):3042–3051, 2015.

[80] Konrad Mertens. *Photovoltaics: fundamentals, technology, and practice*. John Wiley & Sons, 2013.

[81] Klaus-Dieter Jäger, Olindo Isabella, Arno HM Smets, René ACMM van Swaaij, and Miro Zeman. *Solar Energy: Fundamentals, Technology and Systems*. UIT Cambridge, 2016.

[82] Ned Mohan, William P Robbins, and Tore Undeland. *Power electronics: converters, applications and design*. Wiley, 1995.

[83] M Godoy Simões and Felix A Farret. *Modeling Power electronics and interfacing energy conversion systems*. Wiley Online Library, 2017.

[84] Michał Knapczyk and Krzysztof PIEŃKOWSKI. Analysis of pulse width modulation techniques for ac/dc line-side converters. *Prace Naukowe Instytutu Maszyn, Napędów i Pomiarów Elektrycznych Politechniki Wrocławskiej. Studia i Materiały*, 59(26):194–209, 2006.

[85] AI Maswood and HD Tafti. Advanced multilevel converters and applications in grid integration, 2019.

[86] Adrian Ioinovici. *Power Electronics and Energy Conversion Systems: Fundamentals and Hard-switching Converters, Volume 1*. John Wiley and Sons, 2013.

[87] Wikipedia. Buck converter — Wikipedia, the free encyclopedia, 2020. [Online; accessed 21-January-2020].

[88] Texas Instruments Incorporated. *AN-1973 Benefits and Challenges of High-Frequency Regulators*. Jun 2009.

[89] John Leis. *Digital signal processing using MATLAB for students and researchers*. Wiley Online Library, 2011.

[90] Bidyadhar Subudhi and Raseswari Pradhan. A comparative study on maximum power point tracking techniques for photovoltaic power systems. *IEEE Transactions on sustainable energy*, 4(1):89–98, 2013.

[91] Chihchiang Hua and Chihming Shen. Study of maximum power tracking techniques and control of dc/dc converters for photovoltaic power system. In *PESC 98 Record. 29th Annual IEEE Power Electronics Specialists Conference (Cat. No. 98CH36196)*, volume 1, pages 86–93. IEEE, 1998.

[92] Moacyr Aureliano Gomes De Brito, Luigi Galotto, Leonardo Poltronieri Sampaio, Guilherme de Azevedo e Melo, and Carlos Alberto Canesin. Evaluation of the main mppt techniques for photovoltaic applications. *IEEE transactions on industrial electronics*, 60(3):1156–1167, 2013.

[93] Kamran Sharifabadi, Lennart Harnefors, Hans-Peter Nee, Staffan Norrga, and Remus Teodorescu. *Design, control, and application of modular multilevel converters for HVDC transmission systems*. John Wiley & Sons, 2016.

[94] Carlos Bordons, Félix Garcia-Torres, and Miguel A Ridao. *Model Predictive Control of Microgrids*. Springer, 2020.

[95] Mahmoud Saleh, Yusef Esa, Yassine Mhandi, Werner Brandauer, and Ahmed Mohamed. Design and implementation of ccny dc microgrid testbed. In *2016 IEEE Industry Applications Society Annual Meeting*, pages 1–7. IEEE, 2016.

[96] Moacyr AG De Brito, Leonardo P Sampaio, G Luigi, Guilherme A e Melo, and Carlos A Canesin. Comparative analysis of mppt techniques for pv applications. In *2011 International Conference on Clean Electrical Power (ICCEP)*, pages 99–104. IEEE, 2011.

[97] Navid Eghtedarpour and Ebrahim Farjah. Power control and management in a hybrid ac/dc microgrid. *IEEE transactions on smart grid*, 5(3):1494–1505, 2014.

[98] Tan Ma, Mehmet Hazar Cintuglu, and Osama A Mohammed. Control of a hybrid ac/dc microgrid involving energy storage and pulsed loads. *IEEE Transactions on Industry Applications*, 53(1):567–575, 2016.

[99] M Akbari, MA Golkar, and SM Moghaddas Tafreshi. Firefly algorithm-based voltage and frequency control of a hybrid ac-dc microgrid. In *2012 Proceedings of 17th Conference on Electrical Power Distribution*, pages 1–7. IEEE, 2012.

[100] M Akbari, MA Golkar, and SMM Tafreshi. A pso solution for improved voltage stability of a hybrid ac-dc microgrid. In *ISGT2011-India*, pages 352–357. IEEE, 2011.

[101] Rahul Anand Kaushik and Naran M Pindoriya. Power flow control of hybrid ac-dc microgrid using master-slave technique. In *2014 IEEE Conference on Energy Conversion (CENCON)*, pages 389–394. IEEE, 2014.

[102] A Mohamed, SriRajuBushanam Vanteddu, and O Mohammed. Protection of bidirectional ac-dc/dc-ac converter in hybrid ac/dc microgrids. In *2012 Proceedings of IEEE Southeastcon*, pages 1–6. IEEE, 2012.

[103] Poh Chiang Loh, Ding Li, Yi Kang Chai, and Frede Blaabjerg. Autonomous operation of ac–dc microgrids with minimised interlinking energy flow. *IET Power Electronics*, 6(8):1650–1657, 2013.

[104] Muhammad H.. Rashid. *Power Electronics Handbook: Devices, Circuits and Applications*. Elsevier, 2011.

[105] KH Hussein, I Muta, T Hoshino, and Ml Osakada. Maximum photovoltaic power tracking: an algorithm for rapidly changing atmospheric conditions. *IEE Proceedings-Generation, Transmission and Distribution*, 142(1):59–64, 1995.

[106] Marcelo Gradella Villalva, Jonas Rafael Gazoli, and Ernesto Ruppert Filho. Comprehensive approach to modeling and simulation of photovoltaic arrays. *IEEE Transactions on power electronics*, 24(5):1198–1208, 2009.

[107] Tarak Salmi, Mounir Bouzguenda, Adel Gastli, and Ahmed Masmoudi. Matlab/simulink based modeling of photovoltaic cell. *International Journal of Renewable Energy Research (IJRER)*, 2(2):213–218, 2012.

[108] Sara Matasci. The top sunpower solar panels for sale: Energysage, Sep 2018.

[109] MathWorks. Battery.

[110] Olivier Tremblay and Louis-A Dessaint. Experimental validation of a battery dynamic model for ev applications. *World electric vehicle journal*, 3(2):289–298, 2009.

[111] Tesla. Powerpack - commercial & utility energy storage solutions.

[112] Electric Vehicle Database. Tesla model s performance.

[113] Electric Vehicle Database. Nissan leaf e.

[114] Electric Vehicle Database. Bmw i3s 120 ah.

[115] MathWorks. Three-phase dynamic load.

[116] Buildings Datasets. Long-term electricity and gas consumption for lbnl building 74.

[117] Sarmad Majeed Malik, Xin Ai, Yingyun Sun, Chen Zhengqi, and Zhou Shupeng. Voltage and frequency control strategies of hybrid ac/dc microgrid: a review. *IET Generation, Transmission & Distribution*, 11(2):303–313, 2017.

[118] Muhammad Naveed Akhter, Saad Mekhilef, Hazlie Mokhlis, and Noraisyah Mohamed Shah. Review on forecasting of photovoltaic power generation based on machine learning and metaheuristic techniques. *IET Renewable Power Generation*, 13(7):1009–1023, 2019.

[119] Chaojie Li, Xinghuo Yu, Wenwu Yu, Guo Chen, and Jianhui Wang. Efficient computation for sparse load shifting in demand side management. *IEEE Transactions on Smart Grid*, 8(1):250–261, 2016.

[120] Frank Pierie. How to measure and optimize the sustainability of complex (renewable) energy production pathways:: applied to farm scale biogas production pathways. 2018.